OUT ONE END OR THE OTHER, ANALYSIS OF NOVEL TERRESTRIAL FEEDING TRACES FROM EGG MOUNTAIN

by

Ian Michael Matteson

A thesis submitted in partial fulfillment
of the requirements for the degree

of

Master of Science

in

Paleontology

MONTANA STATE UNIVERSITY
Bozeman, Montana

December 2025

DEDICATION

This thesis is dedicated to all the people who have helped me keep my dream alive. Without their support, I would never have made it this far in my adventure. Thank you so much for believing in me.

ACKNOWLEDGEMENTS

I would like to first extend my profound gratitude to Dr. Dave Varricchio, my colleagues in the graduate department, and the Earth Sciences Department at Montana State University for their valuable advice and assistance with this project. I want to thank my committee: Dave for his constant assistance, Dr. Madison Myers for her guidance on geochemical methods, and Karen Chin for her depth of knowledge and wisdom on the subject. I want to thank the Museum of the Rockies for the opportunity and for allowing me to use their specimens. A thank you goes out to Wagner Petrographic for the preparation and thin-sectioning used in this thesis. I want to thank the Imaging and Chemical Analysis Laboratory (ICAL) (RRID: SCR_026325) and the Montana Nanotechnology Facility (MONT) for the use of their JEOL JSM-6100 SEM and Nikon XL3 portable X-ray Fluorescence. I want to thank the University of Washington and Delta Electronics for the use of their CT machines. Special thanks to the staff at the Super Photon Ring-8 (SPring-8) and Dr. Masato Hoshino for their assistance with the collection, use, and analysis of the Synchrotron data for the specimens. We also extend our gratitude to Dr. Takuya Imai for his valuable advice and support throughout our stay in Japan. I want to thank Dr. Jack Horner, Dr. Holly Woodward Ballard, Dr. Ashley Poust, Dr. Danny Barta, Dr. Mark Taper, Dr. Casey Holliday, and Dr. Mary Schweitzer for their expertise and advice. I want to thank Brendan Clark and Harrison Allen for their help with processing synchrotron data, and Heath Caldwell for his help photographing the specimen. I also want to thank my MSU cohort and friends for supporting me throughout my time at MSU. A final thanks goes to my parents, without whose help and encouragement, I would not have gotten this far, and a special thanks to my father, who helped me with the title of this thesis.

TABLE OF CONTENTS

LIST OF TABLES

Table Page

LIST OF FIGURES

Figure Page

LIST OF FIGURES

Figure Page

LIST OF FIGURES

Figure Page

LIST OF FIGURES

Figure Page

LIST OF FIGURES

Figure Page

LIST OF FIGURES

Figure Page

ABSTRACT

The Egg Mountain locality within the Upper Cretaceous Two Medicine Formation of the Willow Creek anticline is thought to represent well-drained soils, with evidence drawn from the fossil record. It has many fossil discoveries, such as the nests and egg clutches of *Troodon formosus* and trace fossils, including invertebrate coprolites and pupal cases. Three unique specimens found at the site, MOR 10878-9, MOR 10878-4A, and MOR 10878-4B, are ovoid dark masses with matrix, and range in size from 68 mm to 17 mm in length. They were examined to determine if their initial identification as coprolites was correct, how and why they were preserved, and what this could tell us about the producer's diet, ecology, and environment. To determine the overall composition of the specimens, pXRF and EDS elemental analysis were performed on MOR 10878-9 and thin sections of MOR 10878-4B. 3D Computed Tomography and synchrotron scans were conducted to identify inclusions and understand the internal structure of each specimen. The EDS data reveal that the matrix has low levels of phosphorus and calcium, suggesting a composition similar to the host sediment rather than a phosphatic coprolite. Synchrotron data and thin sections show that the dark mass of the specimen resembles trabecular bone in cross-section while the cavities have fill that is different from the matix though this is not clearly understood why. Fragments of both cortical and trabecular bone suggest that the producer had eaten material from a potentially juvenile dinosaur. Synchrotron scans also revealed potential invertebrate burrows and fecal pellets, suggesting that invertebrates may have fed on the remains, thereby degrading the soil-facing portion. These specimens may be coprolites that were degraded mainly by detritivores. However, the lack of a pervasive phosphatic ground mass might indicate that the specimens represent a regurgitalite instead. The producer was likely a small to medium-sized predator that may have fed on a younger dinosaur that came from one of the many nests in the area. Further analysis of the fragments within the specimens may provide insight into both predators and prey, as well as their roles in the ecosystem as a whole.

INTRODUCTION

Fossilized traces of animal behavior and activities can provide valuable insights into ancient environments and their ecosystems. Trace fossils can reveal the biology of the animals that produced them, their behavior, their potential ecological niche, and the broader ecology of the region during that time (Chin, 1996). Such information can be challenging to infer from body fossils alone, as even whole-body skeletons often reveal only morphological features and biomechanics (Thulborn, 1991). Unfortunately, traces such as tracks, skin imprints, nests, bromalites, and others can be ephemeral, and environmental factors can often destroy important details (Chin, 1996). Because trace fossils are rare, sites that preserve them are incredibly important. One such location that preserves these traces is Egg Mountain.

Egg Mountain is situated within the Two Medicine Formation, a Campanian-aged Upper Cretaceous formation (Varricchio et al., 2010; Fowler, 2017; Rogers et al., 2025). The Two Medicine Formation consists of terrestrial rocks that were deposited along the Western Interior Cretaceous Seaway, beginning with its regression and ending with its westward transgression (Rogers et al., 1997; Scofield, 2018; Ramezani et al., 2022; Rogers et al., 2025). The section of the Two Medicine Formation that Egg Mountain represents is situated southwest of Choteau, MT, within the Willow Creek anticline. The Willow Creek anticline site is renowned for its numerous fossil finds, including many dinosaur fossils. It has some well-known traces, most notably the abundance of nests from multiple types of dinosaurs (Horner & Makela, 1979; Horner, 1984, 1987; Hirsch & Quinn, 1990; Varricchio et al., 1997, 1999). The anticline also contains other traces, such as coprolites from large herbivores and burrows with pupation traces from invertebrates (Nadon, 1993; Chin, 1996; Martin &Varricchio, 2011). Egg Mountain itself is

known for the clutches of *Troodon formosus*, but other informative traces have been found here, including insect pupae, invertebrate coprolites, and even regurgitalites (Varricchio et al., 1997; Freimuth & Varricchio, 2019; Freimuth et al.,2021).

In July 2010, specimens MOR 10878 7-12-2010-9 (MOR 10878-9) and MOR 10878 7-10-2010-4 (MOR 10878-4A and MOR 10878-4B) were discovered at Egg Mountain and were initially identified as coprolites. While this identification is possible, other explanations need to be considered before being confirmed. Some other possible explanations for these specimens include mineralized concretions or nodules that form in the sediment around other objects (Allen et al., 2025), other bromalites such as regurgitalites (Freimuth et al., 2021), or potentially transported bone. Therefore, further analysis was necessary to gain a deeper understanding of their exact nature. Here, we employed elemental analysis and internal imaging to assess whether these specimens are coprolites, determine how they were preserved, and understand what they can reveal about the environment and ecology of Egg Mountain during the Campanian period.

Terrestrial environments, such as the one represented by the rock layers at Egg Mountain (Freimuth & Varricchio, 2019; Weaver et al, 2021), have been known to preserve bromalites, the fossilized remains from digested material in the form of either: coprolites (fossilized feces), regurgitalites (fossilized gastric pellets or other regurgitated material), and consumulites (fossilized material from the inside of an animal) (Chin et al., 1998, 2003; Northwood, 2005; Hunt & Lucas, 2012; Qvarnström et al., 2024). While terrestrially derived bromalites, though not as abundant as those preserved in aquatic environments, can sometimes be found in caves or cave deposits (Wood et al., 2014; Sanz et al, 2016; Gatta & Rolfo, 2017), they are more commonly found in flood or shallow fluvial or lacustrine deposits (Edwards et al., 1995; Chin et

al., 2003; Northwood, 2005; Hollocher & Hollocher, 2012; Freimuth et al, 2021). These terrestrial bromalites can serve as evidence of the depositional environment, as exposure to the elements prior to fossilization can cause desiccation cracks, such as those seen in some coprolites, which indicate that the coprolite was exposed to air before burial (Northwood, 2005; Hollocher & Hollocher, 2012). Along with this depositional information, terrestrial bromalites can provide a better understanding of the ecology and digestive processes of terrestrial organisms. This information is invaluable, as terrestrial settings do not usually allow for rapid burial, unlike crocodiles, fish, and other aquatic animals that spend most of their time in water, where there is a greater potential for burial (Brachaniec et al., 2015; Platt et al., 2020). Some digestive information about dinosaurs has been discovered previously, such as that found inside tyrannosaurid coprolites (Chin et al., 1998; Chin et al., 2003) and even regurgitated remains of mammal fossils (Freimuth et al., 2021). In the tyrannosaurid coprolites, there are small bone fragments (~1 cm), and one coprolite (Chin et al., 2003) had remnants of muscle fibers. These inclusions indicated that the digestion of tyrannosaurids may not have dissolved even small bone fragments, potentially suggesting that Tyrannosaurus had a short retention time for its meals (Chin et al., 2003). In the case of regurgitates, it can allow us to draw comparisons to modern carnivorous birds, which often egest bone, hair, and other undigested material (Duke, 1997; Qvarnström et al., 2019; Freimuth et al., 2021). Understanding the contents of a bromalite specimen is just as important as understanding its overall morphology.

Background

Geologic Setting

The MOR 10878 specimens were found at Egg Mountain, a fossiliferous location within Teton County, Montana, ~ 19 km southwest of Choteau within the Willow Creek anticline of the Two Medicine Formation (Lorenz & Gavin, 1984; Rogers, 2025) (Fig. 1). The Two Medicine Formation is primarily made up of siliciclastic rock layers that represent sediments of lacustrine and fluvial depositional environments with some volcanoclastic sediments that indicate that there was volcanism in the region at the time (Lorenz & Gavin, 1984; Rogers et al., 1993; Rogers et al., 1997; Roberts & Hendrix, 2000). These rock layers are primarily composed of greenish-grey siltstone and claystone, which dominate the formation. In addition to these rock layers, there are sandstone layers that represent shallow fluvial environments and volcanic bentonite layers that were used for radiometric dating (Rogers et al., 1997; Shelton, 2006; Rogers et al., 2025). The formation was deposited for much of the Campanian, spanning a roughly 8-million-year period from 82.4 Ma to 74.4 Ma (Rogers et al., 2025), making it contemporaneous with the Eagle, Claggett, Judith River, and Bearpaw Formations of North-central Montana and the Milk River and Pakowki Formations and the Belly River Group of Southwest Alberta, CA (Ramezani et al., 2022; Rogers et al., 2023,2025). Deposition of the Two Medicine Formation began as the Colorado Sea regressed eastward, leaving behind non-marine layers that record environments between the Cordilleran Mountain belt and the western edge of the Western Interior Cretaceous Seaway (Rogers et al., 1997). Deposition ended with the transgression of the Bear Paw Sea, leading to the formation being overlain by the Bear Paw Shale (Rogers et al., 1997).

The Willow Creek Anticline spans 77.97 Ma (± 0.024 Ma) to 74.43 Ma (± 0.015 Ma) of the Two Medicine Formation, comprising portions of the Hagens Crossing Member and the Flag Butte Member (Rogers et al., 2025). The rock layers in the area are often calcareous, possibly leached from limestone or other calcium-rich sources that were being eroded in the Cordillera mountains (Chin, 1996; Roger, 1997; Shelton, 2006). This calcareous influence may have helped preserve the herbivore coprolites found in the area (Chin, 1996). The anticline also contains many body fossils, including dinosaurs such as *Maiasaura pleeblesorum* and *Troodon formosus* and other animals such as lizards and mammals, and other traces such as nests and clutches of eggs from dinosaurs (Horner & Makela, 1979; Horner, 1984, 1987; Lorenz & Gavin, 1984; Hirsch & Quinn, 1990; Varricchio et al., 1997, 1998; Jackson et al., 2015).

Egg Mountain itself (Fig. 1) is found on the western end of the Willow Creek anticline. Stratigraphically, Egg Mountain is located in the Flag Butte Member lacustrine interval and has been dated to be approximately 76.99 to 76.5 million years old (Fig. 2) (Varricchio et al., 2010; Fowler, 2017; Rogers et al., 2025). The quarry from which the specimens were extracted is located on top of Egg Mountain hill and was in operation from 2010 to 2016. The majority of the quarry consists of greenish-grey mudstones and siltstones, characterized as calcareous or micritic (Lorenz & Gavin, 1984; Rogers et al., 1993; Shelton, 2006). Egg Mountain is primarily known for and named after the clutches of eggs of the ootaxa *Primatoolithus*, representing *Troodon formosus*, and *Continuoolithus* as well as eggshell fragments found at the location (Horner & Makela, 1979; Horner, 1984, 1987; Hirsch & Quinn, 1990; Varricchio et al., 1997, 1998).

The rock layers at Egg Mountain indicate a depositional environment characterized by subaerial paleosols and well-draining sediments (Martin & Varricchio, 2011; Freimuth et al.,

2021). However, due to the lack of a preserved paleosol horizon, possibly resulting from extensive bioturbation, it has been difficult to prove that the rock layer represents a terrestrial environment (Martin & Varricchio, 2011). Further research on fossils from the site was conducted to draw a more definitive conclusion (Freimuth et al., 2021). Trace fossils have been found at Egg Mountain, including burrows, the previously noted insect pupa cases, coprolites, including those belonging to invertebrates, and the specimens of MOR 10878 (Freimuth et al., 2019, 2021). Other invertebrate traces, such as *Feoichnus martini*, have also been found (Panascí & Varricchio, 2020). Other fossils found at the Egg Mountain site include scattered remains of *Orodromeus makelai* (Horner & Weishampel, 1988), as well as hadrosaur and less common theropod teeth (Scofield, 2018) and the remains of mammals and lizards (DeMar et al., 2017; Weaver et al., 2021). The clutches of eggs, along with the fossils and traces found at Egg Mountain, represent an environment with well-drained sediments, which allowed invertebrates to create these structures (Freimuth & Varricchio, 2019). The evidence from these traces points to subaerial sediments that are likely flood deposits rather than fluvial or lacustrine horizons (Freimuth & Varricchio, 2019; Weaver et al., 2021; Freimuth et al., 2021).

Bromalites

Coprolites

One type of bromalite that can help us better understand an ancient animal and its environment, more so than a body fossil, is the coprolite that the animal leaves behind. However, coprolites—the fossilized remains of feces—are usually scarcer than body fossils because fecal matter tends to decay (Thulborn, 1991; Hollocher & Hollocher, 2012). Many coprolites are found in rock layers from aqueous depositional environments, typically from animals inhabiting

fluvial, lacustrine, or marine environments, allowing the fecal matter to be buried relatively quickly (Brachaniec et al., 2015). However, scat deposited in an aqueous environment can swell and soften, thereby reducing cohesion (Thulborn, 1991). Under high-energy conditions, they may be rapidly destroyed by the current (Thulborn, 1991). In contrast, lower-energy conditions may preserve them longer, allowing them to be buried and preserved (Thulborn, 1991; Hone et al., 2015). In contrast to aqueous environments, scat deposited on land can persist for a time due to it drying out and hardening (Thulborn, 1991). However, terrestrial environments that are erosional or have no sediment deposition will not preserve coprolites. Hardening of scat allows it to be preserved long enough for mineralization to occur, preventing fluvial events like flooding from destroying it during burial (Thulborn, 1991; Chin, 1996). Fecal matter typically persists best in low-energy environments that quickly cover them with sediment (Thulborn, 1991).

Coprolites are typically identified by their shape, distinct coloration, and composition from the surrounding rock (Thulborn, 1991; Chin, 1996). Shape can also be diagnostic of specific digestive systems, as seen in fish with spiral-valve intestinal tracts that produce coiled coprolites (Romer & Parsons, 1986; Chin, 1996). However, it is essential to recognize that coprolites, owing to their relatively malleable origins, can vary in shape and size. Other geologic specimens, such as certain concretions, can be misidentified as coprolites because of their similar shapes (Chin, 1996). Examining the geochemistry and the presence, composition, and preservation of inclusions within the coprolite is essential before a conclusive identification can be made. This evidence can be acquired by both identifying specific inclusions, such as bone or invertebrate fragments in the case of carnivorous defecators (Chin, 2003; Hone et al, 2015; Qvarnström et al, 2017; Qvarnström et al., 2019; Qvarnström et al., 2024) or comminuted plant

material for herbivorous producers (Chin et al., 1996; Qvarnströmet al., 2024). Coprolites from terrestrial-derived sediments have been observed sometimes to contain bones and even traces of muscle tissue (Chin et al., 2003), while others have been found to include plant matter (Chin, 2007). Herbivore coprolites are rarer than those of carnivores because they often lack mineral components from their diet (Hollocher & Hollecher, 2012).

Identifying specific elements within the specimens can be important in determining the producer. Coprolites from a predatory diet have a distinct mineral and elemental composition compared to that of the surrounding matrix (Chin et al., 2003). High phosphate levels in some coprolites can be attributed to bone or soft tissues in a carnivore diet (Chin et al, 2003; Hunt et al., 2012; Qvarnström et al., 2019). The dissolved phosphorus and calcium help preserve them better than their plant-based counterparts through phosphatization (Hollocher & Hollocher, 2012). However, the presence of phosphates can be misleading if environmental factors cause the coprolite to phosphatize rather than the inclusion of bone (Northwood, 2005). Phosphatization from the environment can originate from other calcium- and phosphate-rich sources, such as many nearby shells and bones in the sediment, which are dissolved by water over time (Northwood, 2005). The elemental composition alone should not be the sole basis for determining a diet; it must be considered alongside other methods. Understanding the environment surrounding the specimens will help us determine whether external factors, such as shells (Northwood, 2005), contribute to the elevated P and Ca levels or whether inclusions within the specimens cause them. It is essential to identify animal-derived products within the coprolite, such as bone fragments, scales, muscle fibers, and insect carapaces, which, once digested, would

provide the P and Ca necessary for phosphatization (Chin, 2003; Qvarnström et al., 2017; Qvarnström et al., 2024).

Scat width has been correlated with the sizes of extant animals to better determine an individual's potential size without requiring direct observation of the animal (Weaver et al., 1979; Reilly et al., 2002; Platt et al., 2020). For instance, a study by Platt et al. (2020) found a correlation between crocodile size and the diameter of their scat. Although coprolite size can be used to estimate the minimum size of an animal (Chin, 1996), determining the maximum size of the animal through coprolites is more difficult, as the fecal matter could have been part of a greater whole that was broken apart prior to burial or influenced by other factors that are specific to the individual, further complicating speculation (Chin, 1996). In addition, fecal size can be influenced by several factors, including meal size and the individual's health (Weaver et al., 1979; Reilly et al., 2002; Platt et al., 2020).

Regurgitalite

Another helpful bromalite comes in the form of regurgitalite, or the fossilized remains of material that was egested orally (Hunt, 1992; Myhrvold, 2011). Similar to coprolites, regurgitalites can provide valuable insights into the digestive systems of animals. Voluntary regurgitation of matter often occurs when an animal is unable to digest certain parts of an organism, such as hair, seeds, shells, or bones (Balgooyen, 1971). Regurgitalites can occur in various forms, such as the ejection of undigested material (Cooper et al., 2022) that is loosely held together or, more famously, as gastric pellets, as seen in owls (Duke, 1997). Gastric pellets are observed in various extant animals, including archosaurs (e.g, many birds of prey and crocodiles), varanids, and some mammals (Myhrvold, 2011; Gordon et al., 2020). In extant

archosaurs, this is often attributed to pellets that form in the gizzard of the animal, which stop the undigestible hair, bones, and claws from going further in the digestive system, where they may get stuck and cause a fatal blockage and impaction of the animal (Diver & Stahle, 2015). Gizzards and gastric pellets have also been attributed to dinosaurs, as seen in one species from the clade Paraves described by Zheng et al. (2018); the *Anchiornis* appeared to have a collection of lizard and fish bones with light acid etching in a white mass near its cervical vertebrae. This led the authors to conclude that members of Paraves may have had digestive systems similar to those of modern birds.

Regurgitalites are more challenging to identify than other bromalites. Unlike coprolites, which have a distinct ground mass (phosphate-rich in carnivore coprolites or plant matter in herbivore coprolites), and consumulites, which are found within a body cavity of the fossilized skeleton, regurgitates may often appear to be collections of materials closely packed together (Hunt, 1992). Acid etching has been used in the past as potential evidence for a sample being a regurgitalite (Myhrvold, 2011; Mayr & Schaal, 2016; Zheng et al., 2018) while others have used the absence of the etching to imply the same conclusion (Holgado et al., 2015). The absence of acid etching also does not necessarily preclude a specimen from being either of the other types of bromalite, especially a consumulite. Due to this difficulty, regurgitates have often been misidentified in the past, sometimes as coprolites (Myhrvold, 2011; Gordon et al., 2020). This means that a closer examination of a specimen is required to identify it. In some studies, the presence of soft tissue has been used to distinguish between coprolites and regurgitates, as it is presumed that soft tissue would be digested if it had passed through the digestive system (Myhrvold, 2011; Gordon et al., 2020). However, soft tissue has been found in coprolite samples

before, and its preservation depends on the animal's digestive system and depositional environment (Chin et al., 2003). Another method is to understand the specimen's chemistry. In coprolite samples, the ground mass of the coprolite may have a high phosphate and calcium content derived from digested tissue, whereas in regurgitates, the matrix in the specimen is low in phosphorus but may have a higher calcium content around bone fragments (Gordon et al., 2020; Allen et al., 2025). This calcium around the bones is thought to be from gut bacteria that help to bind the specimen together (Gordon et al., 2020; Allen et al., 2025).

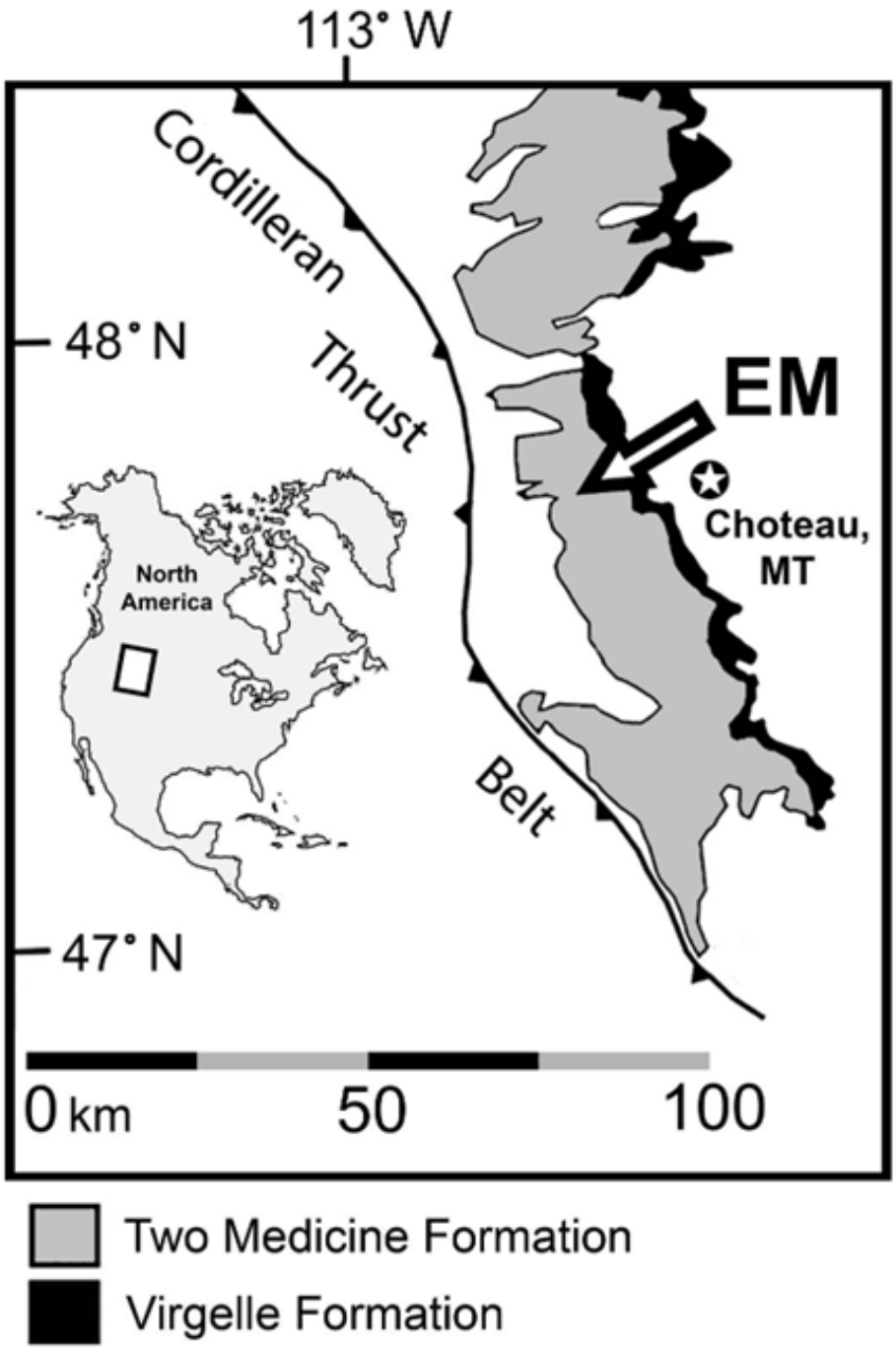

Figure 1: Schematic of geologic map from Freimuth et al, 2021 that shows the Two Medicine Formation's extent in north-central Montana and the relative location of Egg Mountain: EM.

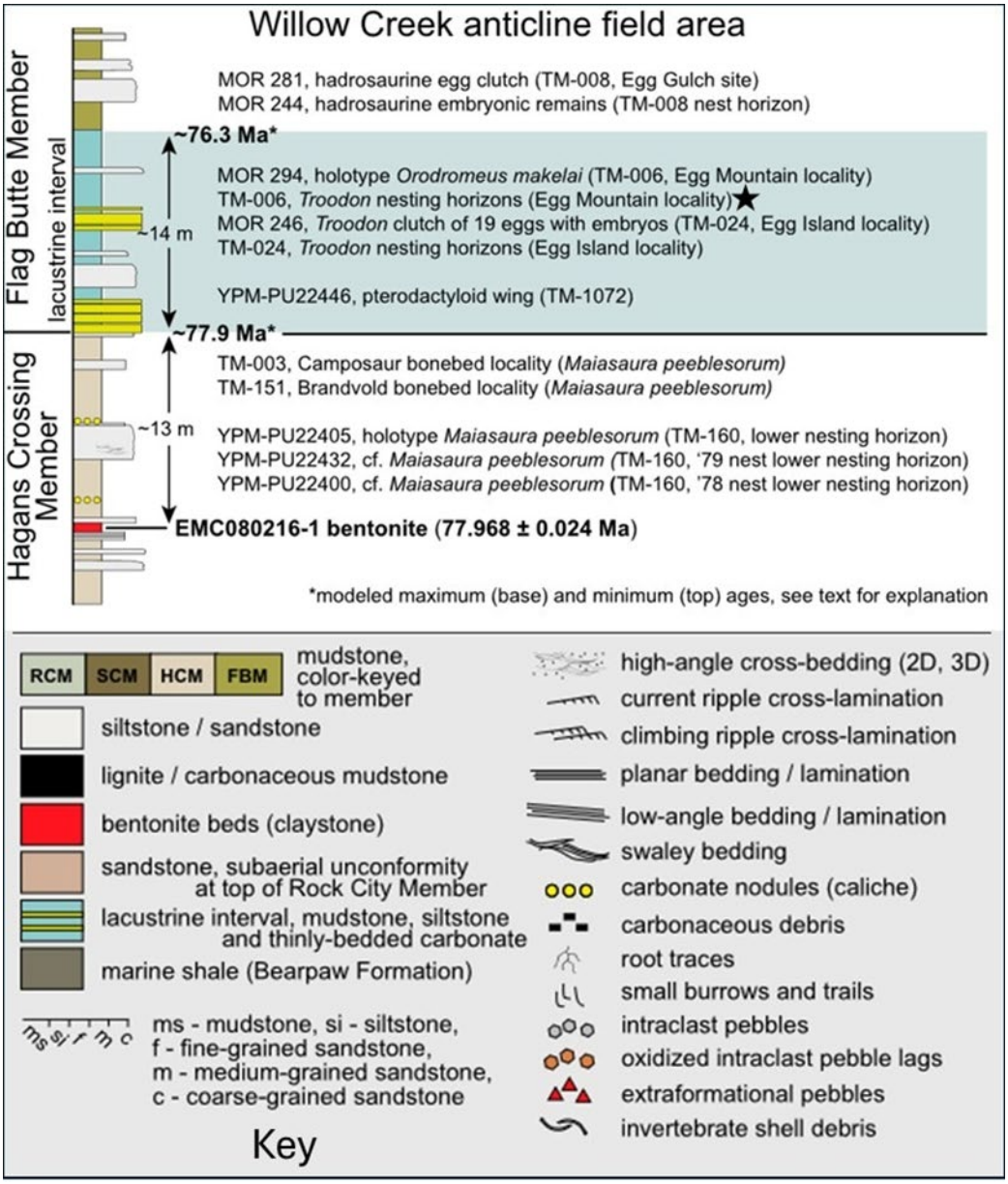

Figure 2: Stratigraphic column of the Willow Creek Anticline showing dinosaur finds within the field area (modified from Rodgers et al., 2024). Star notates the relative location of where MOR 10878 was found. MOR: Museum of the Rockies specimen numbers, Montana State University, Bozeman, Montana, USA; TM: Museum of the Rockies field locality numbers; YPM-PU: Yale Peabody Museum (New Haven, Connecticut, USA), Princeton University (Princeton, New Jersey, USA) specimen numbers.

MATERIALS AND METHODS

Specimens

This study describes three specimens (Figs. 3-5; Table 1), found at Egg Mountain that were collected on July 10th (MOR 10878-4) and 12th, (MOR 10878-9), after the site had been reopened in 2010 in the North 6/West 8 quadrant at depths of 619 mm (MOR 10878-9 and MOR 10878-4) from the datum. The quadrant also contained a lizard premaxilla (MOR 7-12-2010-6), triangular teeth that may be mammalian (MOR 7-12-2010-8), and various other bone fragments (MOR 7-15-2010-10). Other specimens found at similar depths (within 50 mm) are: lizard bones (MOR 7-12-2010-5, MOR 7-17-2010-15), mammal bones (MOR 7-29-2010-35, MOR 8-1-2010-41), Ossified tendons MOR 7-21-2010-23), eggshell fragments (MOR 8-1-2010-38, MOR 8-1-2010-39, MOR 8-1-2010-40, MOR 8-1-2010-42), bone assemblages of a large bone that was possibly hadrosaur (MOR 7-10-2010-6, MOR 7-17-2010-13, MOR 7-27-2010-31), other large bone fragments that include ribs (MOR 7-18-2010-18, MOR 7-18-2010-19, MOR 8-1-2010-43, MOR 8-1-2010-44), and a theropod tooth, possibly from a tyrannosaur (MOR 7-10-2010-3) (Scofield, 2018).

MOR 10878-7-12-2010-9 (MOR 10878-9) (Fig. 3) is the biggest of the three specimens, at 67 mm by 48 mm at its widest. MOR 10878-7-10-2010-4 is split into two specimens, labeled MOR 10878-4A and MOR 10878-4B, which are smaller. MOR 10878- 4A (Fig. 4) is 34 mm by 19 mm. MOR 10878-4B (Fig. 5) is 37 mm by 22 mm. Each has a dark portion, described as a dark mass in this paper, that exhibits a slight reflective property, is primarily composed of trabecular bone, as identified later in this paper, which is located at the top of the specimens.

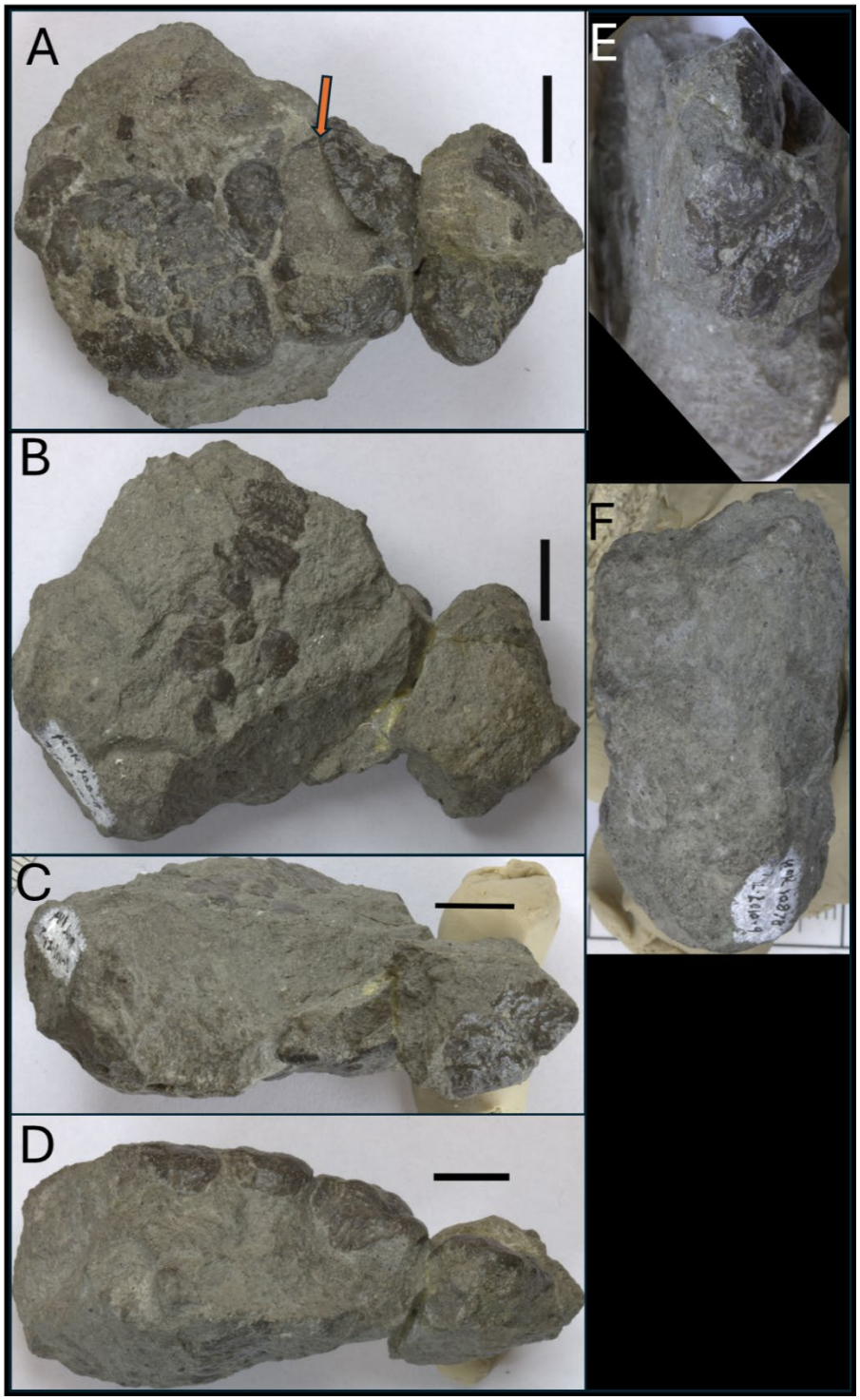

Figure 3: MOR 10878-9 specimen oriented with the dark mass on the top. A) top view with arrow pointing to damaged area that shows interior, B) bottom view, C) anterior view, D) posterior view, E) right-hand side view, and F) left-hand side view. The scale line represents 1 cm.

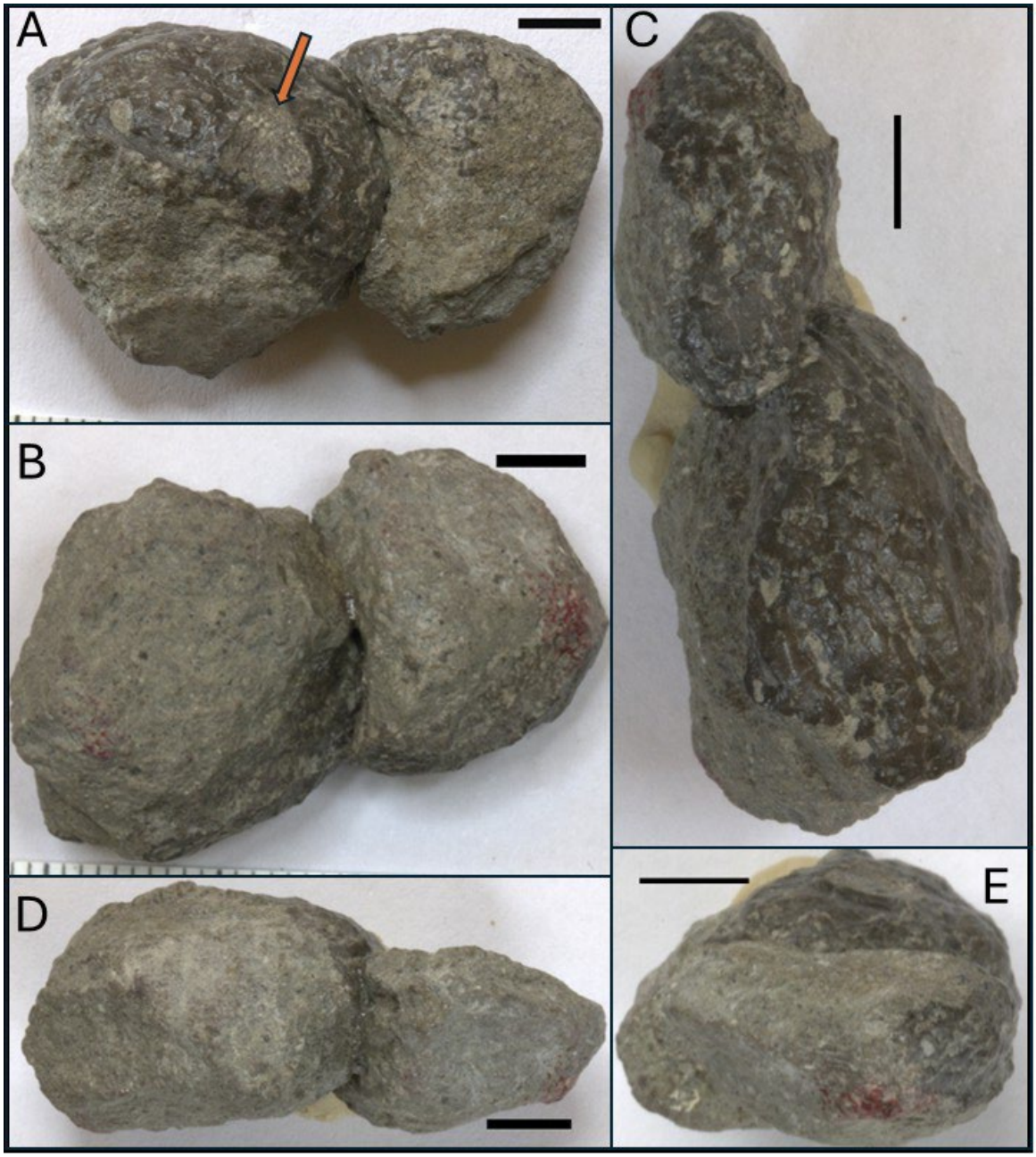

Figure 4: MOR 10878-4A specimen oriented with the dark mass on the top. A) top view with arrow pointing to damaged area, B) bottom view, C) anterior view, D) posterior view, and E) left-hand side view. The scale line represents 50 mm.

Figure 5: MOR 10878-4B specimen oriented with the dark mass on the top. Arrows point to matrix infilled cracks. A) top view, B) bottom view, C) anterior view, D) posterior view, E) left-hand side view, and F) right-hand view. The scale line represents 50 mm.

For definitional purposes, the dark mass includes these dark areas on top as well as the sediment in between.

MOR 10878-4 had 3D images of them taken with the 3D AMETEK Creaform Go!SCAN structured light scanners at the Museum of the Rockies. MOR 10878-9's and MOR 10878-4B's CT scans were used to create a 3D mesh in 3D Splicer and Dragonfly 3D, respectively, for printing. MOR 10878-9 and MOR 10878-4B were 3d printed using a Formlabs Form 2 – 3D resin printer using Grey Resin V5..

Thin Sections

Three polished thin sections were made of MOR-10878-4B, across the long and wide axes (37 mm x 22 mm), to transect the specimens and provide the most information about the dark mass and its interaction with the surrounding sediment, as well as give us the best opportunity to find inclusions. These thin sections were first observed under a Nikon Eclipse LV100 POL and a Leica DMR petrographic microscope to detect internal inclusions and unique features. Cross polarization and a lambda (gypsum) plate were used to identify different areas within the specimens. Photomicrographs were taken with an attached Leica EC4 digital camera and a Canon 5D Mark II digital SLR camera, respectively, on areas of interest. Other areas of interest for elemental analysis were marked for Energy-Dispersive Spectroscopy (EDS) using a Scanning Electron Microscope (SEM).

Geochemical Analysis

A Nikon XL3 portable X-ray Fluorescence (pXRF) instrument from the Imaging and Chemical Analysis Laboratory (ICAL) at Montana State University was used on 10878-9 at four

locations (see lower images in Table 1). Due to concerns about contamination from the preservative coating, which might obscure data, two locations were selected from areas that appeared uncoated. At the same time, the other two locations were chosen from areas likely coated with preservative plastics to provide a comparison. The first location was a site on the surrounding sediment near the broad end of the specimen on the posterior end, where no noticeable coating was observed, allowing for data collection from the matrix (Site 1). The second part of the dark mass near the broad end of the specimen did not seem to be coated (Site 2). The third (Site 3) was taken on the dark mass near the narrow end of a part that seemed to be coated. The fourth (Site 4) was on the opposite side of the others on a dark patch that may have been fossilized bone. The primary elements of interest, such as silicon and phosphorus, were identified and compared across the four locations.

A JEOL JSM-6100 SEM from ICAL was used to perform Energy-Dispersive X-ray Spectroscopy (EDS) on the thin sections of MOR 10878-4B to determine the elemental composition and weight percent of specific areas within the thin sections. Thin sections were coated with carbon to a thickness of approximately 20 μm. Elemental maps were generated at an accelerating voltage of 15 keV and a beam current of 30 nA. Specific, relevant, and abundant elements, such as P, Al, and Si, were mapped.

Both pXRF and EDS methods give elemental compositional analysis of the specimens. However, lighter elements like phosphorus (P) and silicon (Si) are more accurately detected by SEM-EDS, which offers higher resolution at specific points of interest within the specimen (Lemiere, 2018). Although there is higher uncertainty, the pXRF nonetheless helps us link the two specimens without resorting to more destructive methods (e.g., thin sections).

3D Internal Analysis

CT scans of MOR10878-9 were taken via an NSI X5000 scanning system at the University of Washington, and Delta Electronics took additional CT scans for MOR10878-9, MOR10878-4A, and 4B in Taiwan via a DELabμCT-100micro CT scanner. This produced a total of 4 scans: 2 of MOR 10878-9 and 1 each of MOR 10878-4A and MOR 10878-4B. However, internal images of the specimens were not as precise as we needed to see the interior of the dark mass and identify specific inclusions, requiring greater clarity for proper internal analysis.

MOR 10878-9, MOR 10878- 4A, and the puck of MOR 10878-4B were then scanned via the beamline BL28B2 at the SPring 8 synchrotron in Sayo, Hyogo, Japan, with the help of Dr.

Table 1: MOR Specimens and methods used on each specimen. Fragments are noted with: total found; number of fragments identified as Cortical; number of fragments identified outside of the dark mass; range of longest axis for found fragments.

Specimen	**MOR 10878-4A**	**MOR 10878-4B**	**MOR 10878-9**
Size (mm)	34 x 19 x 13.5	37 x 22 x 18.5	67 x 48 x 24
Date Collected	7/10/2010	7/10/2010	7/12/2010
CT-Scan	X	X	X
Synchrotron	X	X (Puck)	X
p-XRF			X
Thin section		X	
EDS/SEM		X	
Fragments	10; 5 Cortical; 4 Trabecular; 1 Unknown 0.8 – 4.6 mm	5; 2 Cortical; 2 Trabecular; 1 Unknown 2.3 – 9.8 mm	7; 6 Trabecular; 1 Unknown 2.6 – 30.2 mm
Notes	Two associated oval pieces glued together; Damage to the larger left segment (Fig. 4A)	One whole piece; Semi-oval; 3 thin sections, remainder of the specimen in puck; Possible desiccation cracks	Semi-Triangular with glued piece to the anterior end; Bone fragments visible on the bottom of the specimen; Damage to the anterior end of the specimen; Possible desiccation cracks

Masato Hoshino. The BL28B2 beamline is a high-energy white X-ray beam that does not pass through any optical devices to acquire microtomographic data (Imai et al., 2022). Lower-energy X-rays are filtered out using a heavy-metal applicator, allowing a peak energy of ~200 keV for tomography (Hoshino et al., 2017). The three specimens were placed in a plastic container lined with melamine sponges to prevent contact with the container walls and to help stabilize them. The “normal set” and “offset” methods, which scan the specimen within the beam area and rotate a larger specimen to scan it entirely within the beam area, respectively, were used to scan each specimen, allowing scans larger than 32 mm. The adequate pixel size was set to 12 μm with 7200 projections.

The tomographic image sequence was modified using the FIJI ImageJ version to reduce file sizes and create more precise images. These TIFF files were then rendered in the Dragonfly version for 3D analysis. Inclusions were highlighted and extracted to identify discernible morphological features.

RESULTS

Physical description

MOR 10878-09 and MOR 10878-4 specimens (Figs. 3-5) all have a lobate form. They consist of a glossy, dark brown mass, often fragmented and cracked, surrounded by a green-gray matrix. The dark mass was identified as the main body of the specimens, running lengthwise and shaped like a semi-ovoid. This mass exhibits a slight shine on non-coated sections (Fig. 6A), whereas it appears glossier in coated sections (Fig. 6B, D). The matrix is a mudstone characterized by tiny flecks or clasts less than 1 mm in diameter, ranging in color from dark (black and brown) to light (white, gray, and light blue/green), which is typical of the matrix of Egg Mountain(Lorenz & Gavin, 1984; Rogers et al., 1993; Shelton, 2006). The orientation of the specimens during acquisition was not recorded; therefore, the positions of 'up' and 'down' are arbitrarily defined, with the coprolite at the top and the matrix at the bottom, based on the presumption that this is how they were found, as there are no notes or photos to confirm their orientation. The dark mass can have rounded margins that curl into the surrounding matrix, or it can have rough or broken edges. The rounded margins are likely the natural extent of the dark mass when it was produced, while the rough and broken edges may result from damage by detritivores or taphonomic processes after the mass hardened (Thulborn, 1991). The dark mass does not extend continuously to both sides of the specimens, and although it has rounded edges, these do not extend to the bottom of the specimens.

MOR 10878-9 (Fig. 3) is the largest of the specimens, with the entire specimen measuring 67 mm in length, 48 mm in width at its widest point, 20 mm at its narrowest point, 24 mm in depth at its thickest point, and 15 mm at its thinnest point. The specimen is semi-

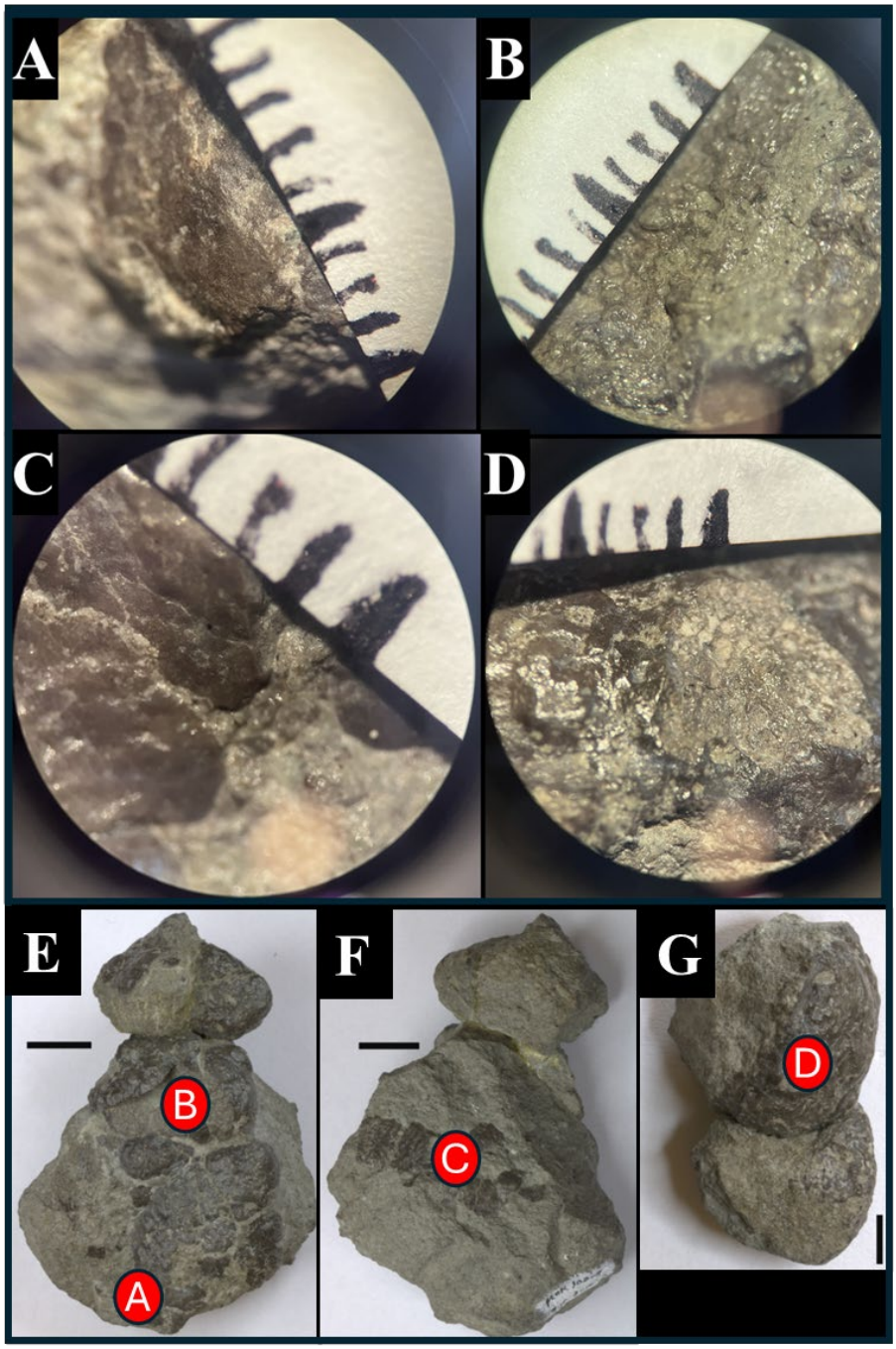

Figure 6: Close-up photos taken through a Nikon C-DS Specimen Microscope(A-D) and their locations on the specimens(E-G). Each tick in A-D equals 1 mm. A) Portion of dark mass on the posterior end of MOR 10878-9 that shows an uncoated section that is slightly less lustrous than the coated section. B) Coated broken area near the anterior portion of the specimen MOR 10878-9, showing the interior of the specimen. C) Suspected bone fragment on the bottom of specimen MOR 10878-9. D) Broken portion of specimen MOR 10878-4A. E) Top view of MOR 10878-9. Scale = 1 cm. F) Bottom view of MOR 10878-9. Scale = 1 cm. G) Top view of MOR 10878-4A. Scale 50 mm.

triangular, with a slight bulge measuring 28 mm by 20 mm by 16.5 mm, glued to the anterior end of the specimen. The top is primarily covered by a dark mass, with the main body measuring approximately 28 mm at its widest point. Part of the mass has been damaged towards the anterior end (Figs. 3A, 6B). This damage reveals the interior of the mass, which appears slightly lighter in color than the exterior and has a rougher texture. The posterior end is covered with a small amount of the dark mass or the surrounding matrix, with only a few cracks and parts of the sediment visible through it. Some of the observed cracks in the surface of the dark mass appear to be infilled with matrix. Because the matrix does not have similar cracks running through it, the infill likely occurred before the matrix was cemented, probably early in the taphonomic process. These cracks could indicate desiccation of the mass after exposure on the surface, or they may be pre-burial fractures. Smaller dark patches on the bottom of the specimen have a texture that could be indicative of bone fragments (Fig. 6C). These fragments are close together and span a 31 mm by 13 mm portion of the specimen. Individual fragments range in measurement from 5 mm by 5 mm pieces to 12 mm by 9 mm chunks (Figs. 3B, A3; Table A1:ID 20). These fragments seem to be 15 mm away from the top of the specimen, at least on the surface.

MOR 10878-4 comprises two specimens labeled MOR 10878- 4A (Fig. 4) and MOR 10878- 4B (Fig. 5). The specimens were found together but are not attached. 10878- 4A consists of two small, semi-ovoid segments, one slightly more prominent than the other, measuring 21 mm x 19 mm x 18.5 mm and 17 mm x 15 mm x 13.5 mm, respectively. It should be noted that these segments do not align completely along the glued edge, and CT scans reveal that the segments are not connected under the obscured portion between them. The left segment (Fig. 4A) exhibits notable damage to the dark mass (Fig. 6D), with an internal structure similar to that

observed in the broken portion of MOR 10878-9. 10878-4B is 37 mm long, 22 mm wide, 22 mm deep at its thickest point, and 13 mm at its thinnest. MOR 10878-4B had the most rounded edges of the dark mass that extended over the edges of the specimen; however, parts of the dark mass's edges are broken off. Multiple matrix-filled cracks were visible around the mass, possibly due to desiccation or pre-burial fracturing, similar to that observed in MOR 10878-9. Unlike in MOR 10878-9, neither MOR 10878-4A nor 4B appear to have either broken bone fragments or coprolite fragments on their downside, which are dominated by the surrounding matrix.

Internal Analysis: Thin Section

Light Microscope

Observations of the thin sections of MOR 10878-4B (Figs. 7, 8) yielded many interesting findings in cross-polarized light and with a lambda plate (λ-XPL). At least three sizeable (>5 mm) bone fragments with some penetrating from one slide to another (Fig. 7A). These fragments exhibit several features that are consistent with bone, including: optical properties of internal crystals consistent with hydroxyapatite, layers of fossilized lamellae, and structures of osteons. These fragments are less than 8 mm in size, with the longest being approximately 8 mm along their longest axis and around 5 mm along their shortest axis (Fig. 7C). The fragments are often angular and rough at their ends. These fragments exhibit sharp edges, suggesting breaking, similar to those seen in CT scans in Figure 7C, where portions of the bone display cracking or fractures. Other portions of some of these fragments exhibit rough edges (left side of Fig. 9B) while others have more curved features (Figs. 10, 11,

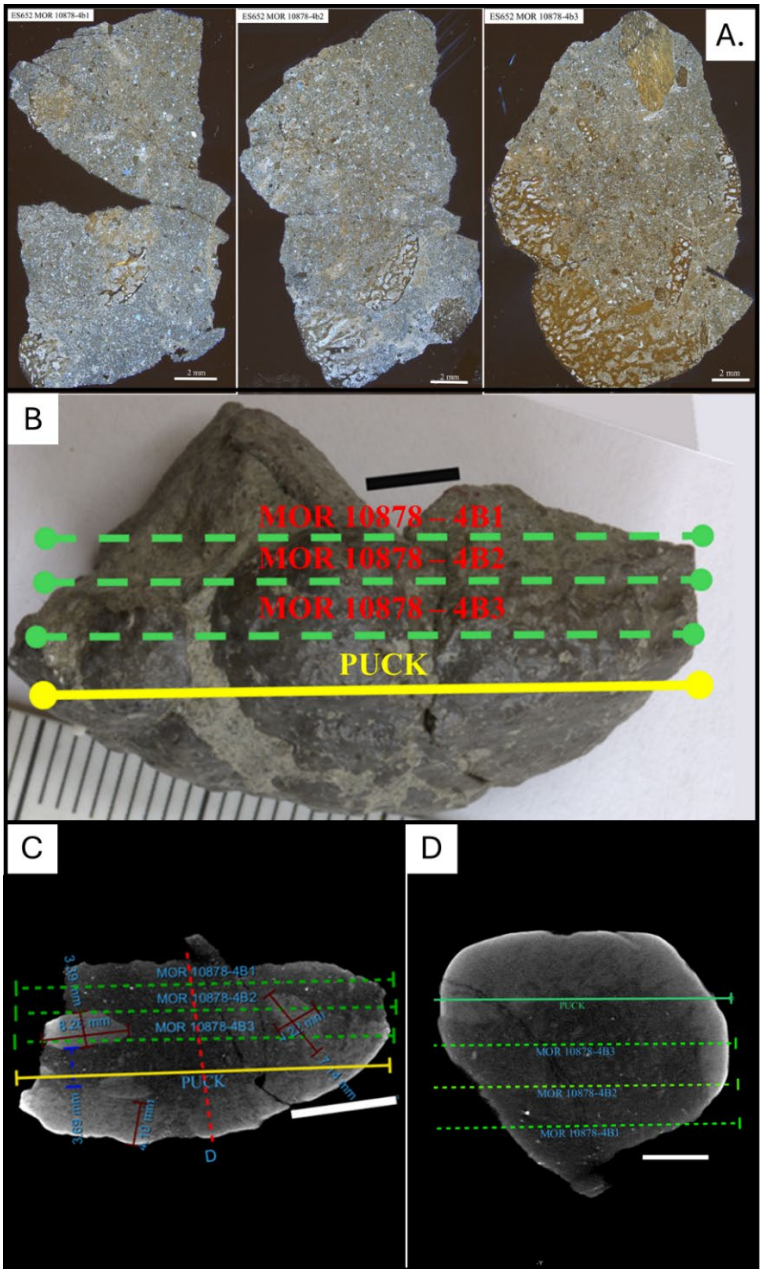

Figure 7: A) Picture of thin section slides ES653 MOR 10878-4B1-3 taken from MOR 10878-4B (Fig. 5). Scale bar = 2 mm. B) Picture of side view of MOR 10878-4B prior to thin-sectioning with lines corresponding to thin sections. Scale Bar = 5 mm C) CT scan of MOR 10878-4B interior side view before thin-sectioning. Dashed green lines represent thin-section orientation, while the yellow line represents the internal extent of the puck, and the dashed red line represents the location of D. The dashed blue line represents the shortest distance to the dark mass from the nearest fragment. Dark red lines represent the length of the fragment or the depth of the mass. Scale bar = 10 mm. D) Perpendicular CT scan of MOR 10878-4B with the dark mass on the top of the specimen. Scale Bar = 5 mm.

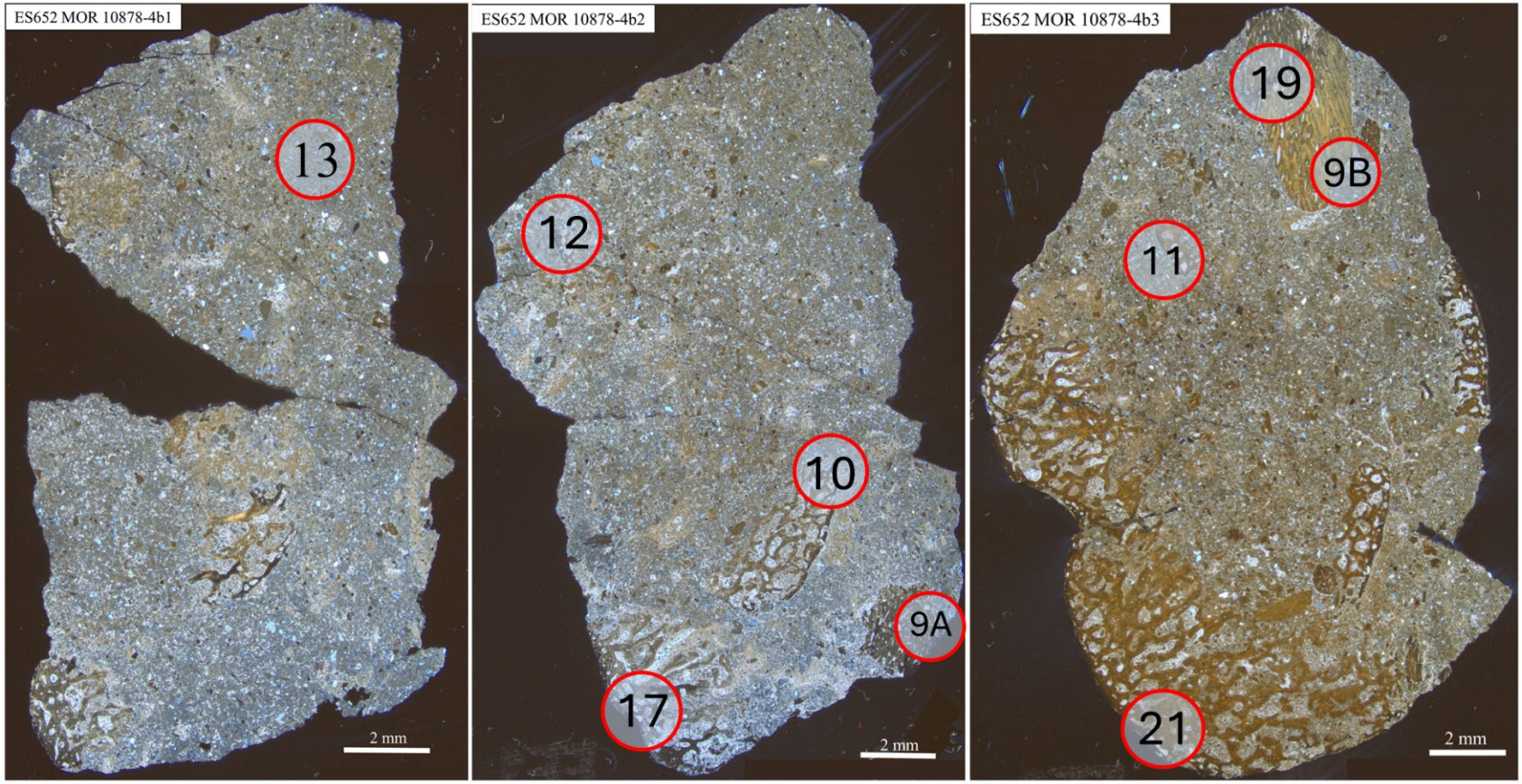

Figure 8: Picture of thin section slide ES653 MOR 10878-4B1-3. Circled numbers correspond to the figure number.

12). These curved portions of the fragments are likely the outer edge of the bone, possibly on the epiphysis of a limb element or cranial element (Bailleul et al, 2012).

Fragment ID 1 (Fig. A1; Table A1) from MOR 10878-4B appears to have an oval structure, with what seems to be the surrounding bone encompassing a hollow center filled with recrystallized material (Fig. 9A). These features are identified as Haversian systems, cylindrical structures of bone call osteons found within dense cortical bone, with some overlapping with other systems that are likely secondary osteons, while others are more isolated. Unfortunately, their identification, as well as that of possible osteocyte (bone cell) lacunae, is difficult to identify within the bone. However, the osteocytes should still be visible in certain portions of the slides as seen in other dinosaur bone thin sections. The lack of noticeable osteocytes may be due to a diagenetic process that altered the bone. However, this is unusual, as other features (such as the cartilage noted later) are present on the exterior of the bone fragments and the dark mass. The central canals of the osteons are filled with a clear crystal.

The fractures observed within the Haversian systems in Figure 9A could indicate deformation of the fragment. The origin of the deformation is unclear, but since minor deformations are observed in other fragments in these specimens, this may be due to lithostatic pressure, as seen in other bones from the formation (Woodward Ballard, 2012). Another possibility is that the deformation occurred before the fragment was buried, or even before digestion. While some breaks are observed in the thin sections, they may not explain the bubbly texture observed in this sample. This bubbly texture also resembles fiber bundles and fascicles, as seen in the ossified tendons of dinosaurs (Horner et al., 2016). The pattern of the Haversian systems indicates that these fragments are cortical bone, possibly from the outer surface of a

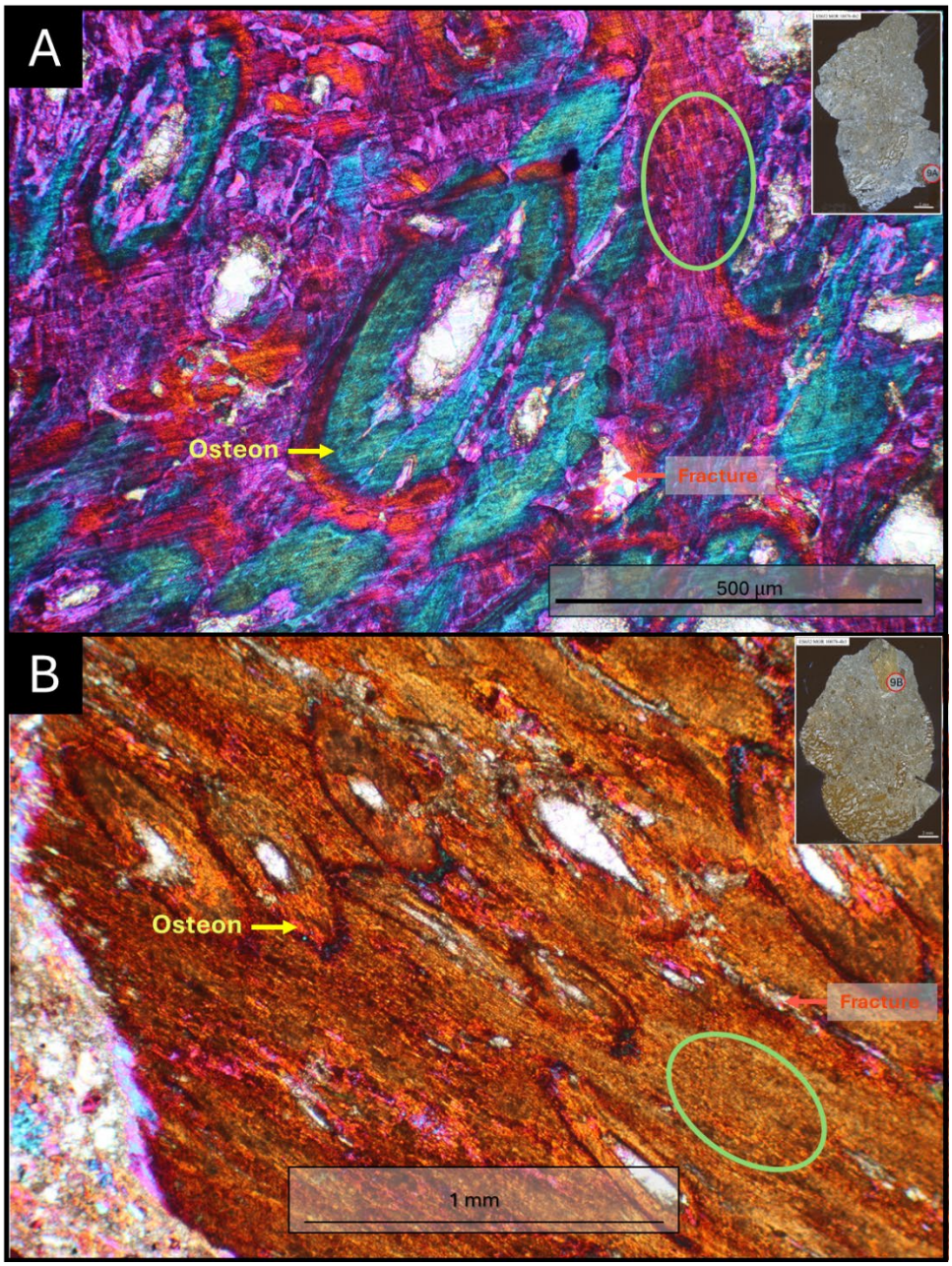

Figure 9: Photomicrograph obtained using a Leica DMR petrographic microscope with a Canon 5D Mark II digital SLR camera on a thin section slide, A) (ES 654 MOR 10878-4B2) under 100x magnification and B) (ES 654 MOR 10878-4B3) under 50x magnification, both with cross-polarization and interference colors from a lambda plate. Both show potential Haversian Systems in the bone fragment that is thought to be cortical bone or ossified tendons. Red arrows point to fractures in the bone. Yellow arrows point to osteons. The green-circled areas highlight a bubbly, textured bone (metaplastic bone).

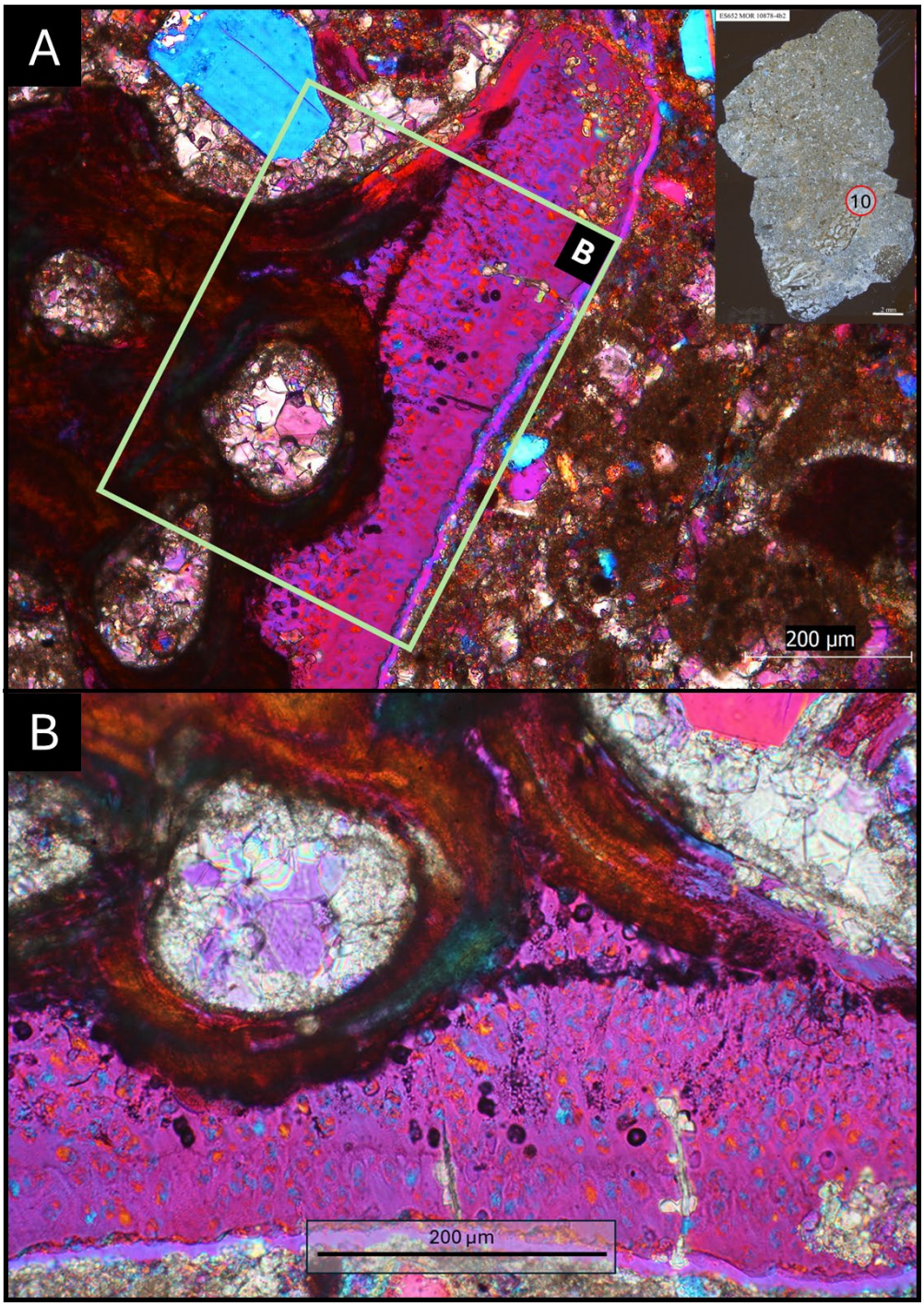

Figure 10: Photomicrograph obtained using a Nikon Eclipse LV100 POL Petrographic microscope with a Leica EC4 digital camera on a thin section slide. A) ES 654 MOR 10878-4B2 under 10x magnification with cross-polarization and interference colors from a lambda plate, showing the end of a bone fragment with fossilized cartilage cells. B) Boxed area under 200x magnification showing the cartilage layer.

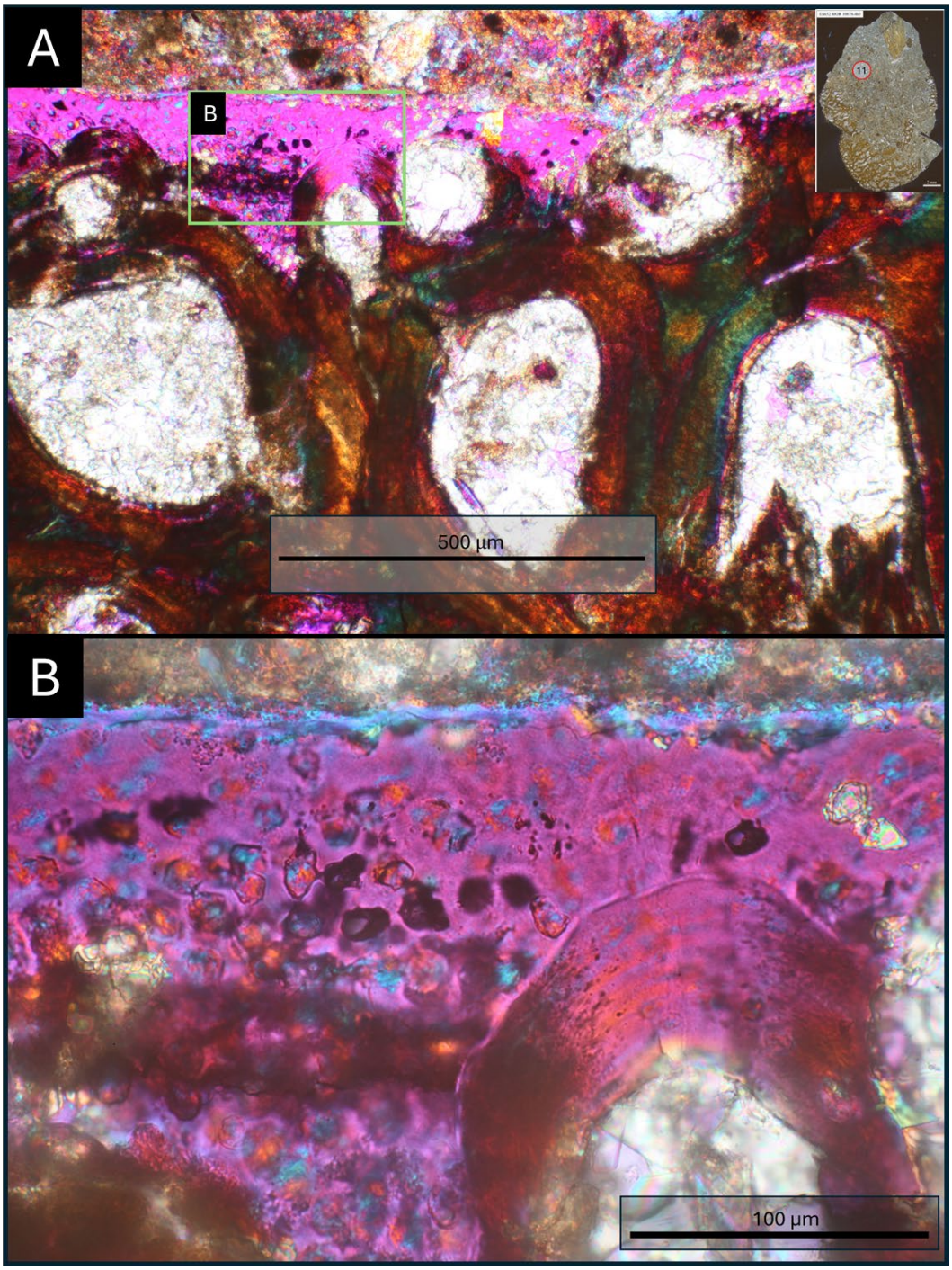

Figure 11: A) Photomicrograph obtained using a Leica DMR petrographic microscope with a Canon 5D Mark II digital SLR camera on a thin section slide (ES 654 MOR 10878-4B3) under 100x magnification with cross-polarization and interference colors from a lambda plate. It shows the end of a bone fragment with fossilized cartilage cells. B) Boxed area 400x magnification showing cartilage area with possible ossification.

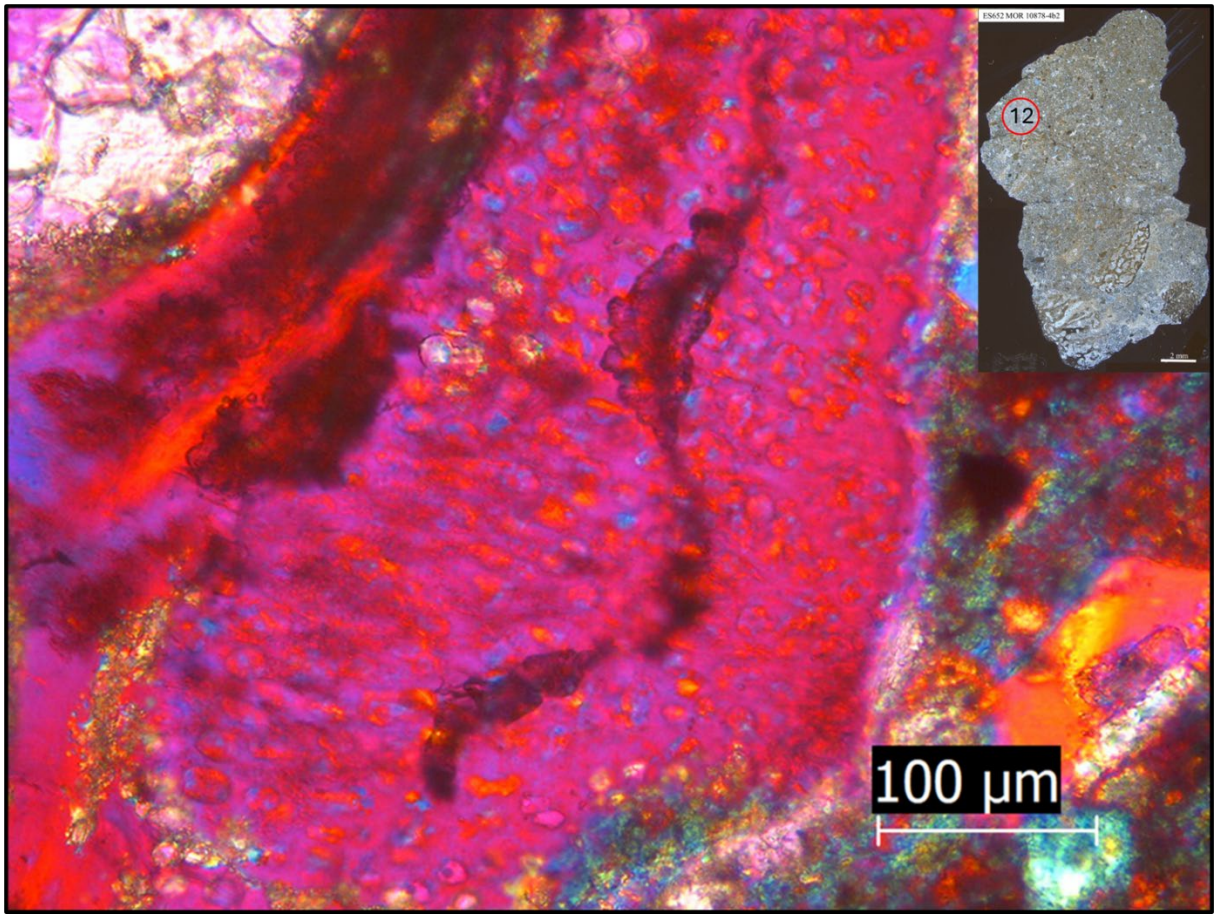

Figure 12: Photomicrograph obtained using a Nikon Eclipse LV100 POL Petrographic microscope with a Leica EC4 digital camera on a thin section slide (ES 654 MOR 10878-4B2) under 20x magnification with cross-polarization and interference colors from a lambda plate. Shows the area of cartilage growth on bone fragments.

bone or ossified tendons (Organ and Adams, 2005). The bone tissue surrounding the osteons appears to be metaplastic bone or primary tissue in Figure 9B, similar to that found in ossified tendons (Horner et al., 2016). The presence of secondary osteons within fragments could imply a more ontogenetically mature individual; however, this feature can also be observed in juveniles (Adams & Organ, 2005) and is present in different bones at various stages of ontogeny (Padian et al., 2016).

Fragment IDs 2 and 3 (Fig. A1; Table A1) from MOR-10878-4 B within the slides exhibit multiple features of interest (Figs. 10, 11). Firstly, parts of the fragments show a bone with no distinct shape beyond interconnected struts. The struts are damaged but show cavities filled with calcite and silicate minerals. Most of these cavities are likely interconnected and seem to share properties with other features of the fragment near the fragment's edge. These strut-like features appear to be more closed loops of bone, with some loops resembling chondroid tissue or ossifying cartilage compared to the rest of the material (Fig. 11) (Goret-Nicaise, 1984). These closed loops near the edge could be developing into osteons that close as an individual grows. Along certain edges of these fragments, there are areas of distinct texture and morphology similar to ossified bone, but with optical properties similar to those of the cartilage segments (Figs. 10, 11, 12). The texture of the feature appears to consist of fossilized cartilage cells in these areas at the edge of the bone, likely representing more chondroid tissue. This tissue appears as a sharp, thin boundary between the fragment and the surrounding matrix. In another smaller fragment, some cartilage sections are thicker than others, possibly indicating a thicker section of cartilage. However, this may represent the slide being cut at an oblique angle to the bone (Fig. 11). There are a total of four fragments found in the thin section of MOR 10878-4B, including ID 2 and 4, that seem to have ossified cartilage.

Elemental analysis

Compositional analysis of MOR 10878-9 (Table 2) conducted using pXRF revealed stark contrasts between data collection sites 1-4 (Sites pictured below in Table 2). Site 1 was derived from the surrounding matrix and exhibited the highest amounts of silicon (Si) and relatively high amounts of aluminum (Al), while displaying relatively low amounts of phosphorus (P) and

calcium (Ca); however, Ca remained at a high amount when compared to Si, being within 20 parts per million (ppm). This high content of Si and Al indicates the presence of silicates within the sediment that made up the mudstone. Site 2 was located on a portion of the dark mass that was uncoated and exhibited higher Ca than Si, as well as significantly higher P, with relatively lower Al. Site 3 on the potentially coated section of the dark mass that had been damaged showed similar amounts of each element, although all amounts were less than those in Site 2. This lower value may be due to the plastic coating obscuring the totals. Site 4, located on the opposite side of the specimen near some bone fragments, showed distinct abundances: higher Si and lower Ca than similar levels; P remained constant; and Al was lower, as observed in Site 3. Iron (Fe) stayed relatively consistent throughout each scan.

Table 2: Portable-XRF data from MOR 10878-9. Circled numbers correspond to each site. Site 1 is on the surrounding matrix; Site 2 is on a possible. Amounts are in normalized wt%.

Oxide	Site 1	Site 2	Site 3	Site 4
CaO	31.5	56.2	71.9	45.4
P_2O_5	5.4	19.7	13.6	11.8
SiO_2	50.2	14.6	9.5	33.7
FeO	3.4	1.5	1.8	2.9
Al_2O_3	9.2	2.7	1.0	6.2

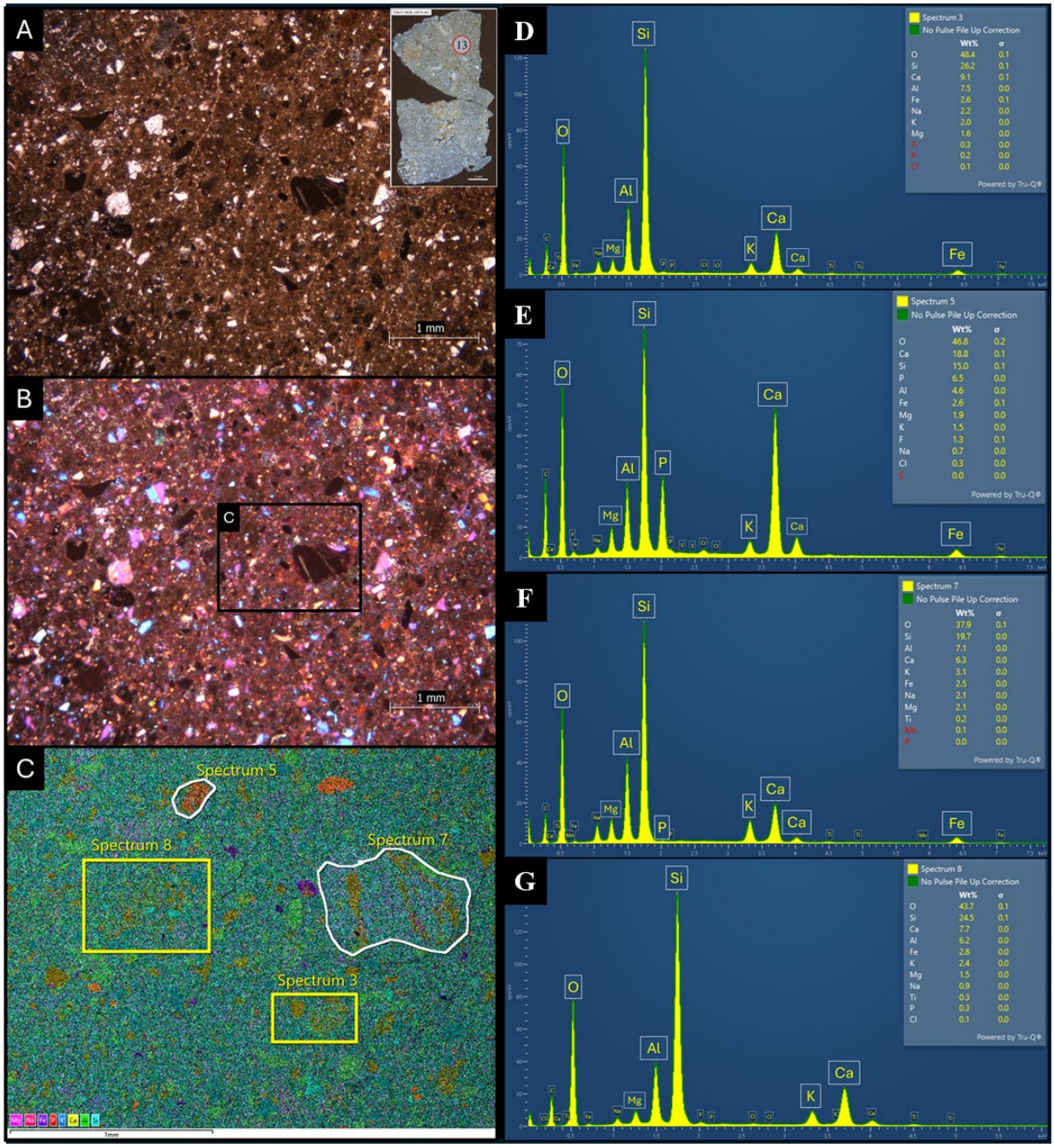

Figure 13: A) Photomicrograph obtained using a Nikon Eclipse LV100 POL Petrographic microscope with a Leica EC4 digital camera on a thin section slide (ES 654 MOR 10878-4B1) under 10x magnification. B) Photomicrograph with cross-polarization and interference colors from a lambda plate. Shows the area used for EDS for the surrounding sediment. C) EDS Map data from the surrounding sediment matrix of MOR 10878- 4B1. D - G show EDS Map Spectrum from sites. D) Spectrum site 3: unusual mineral clast. E) Spectrum site 5: phosphorus signal found in matrix. F) Spectrum site 7: large mineral in the specimen. G) Spectrum site 8: scanned for general matrix make-up.

Table 3: Element weight percent from oxides from EDS data for Figure 13. From MOR 10878-4B1 in the surrounding matrix.

Location	Na	Mg	Al	Si	P	S	K	Ca	Ti	Mn	Fe	Total	CaO/ P_2O_5
Spectrum 3	2.4	2.2	11.7	46.3	0.3		2.0	10.6	0.4		2.8	78.6	34.0
Spectrum 5	0.8	2.6	7.2	26.6	12.5	0.1	1.5	21.9			2.8	75.8	1.75
Spectrum 7	2.9	3.5	13.3	42.1	0.1		3.8	8.8	0.3	0.09	3.2	77.9	147
Spectrum 8	1.2	2.4	11.6	52.1	0.5		2.9	10.8	0.5		3.6	85.6	19.9

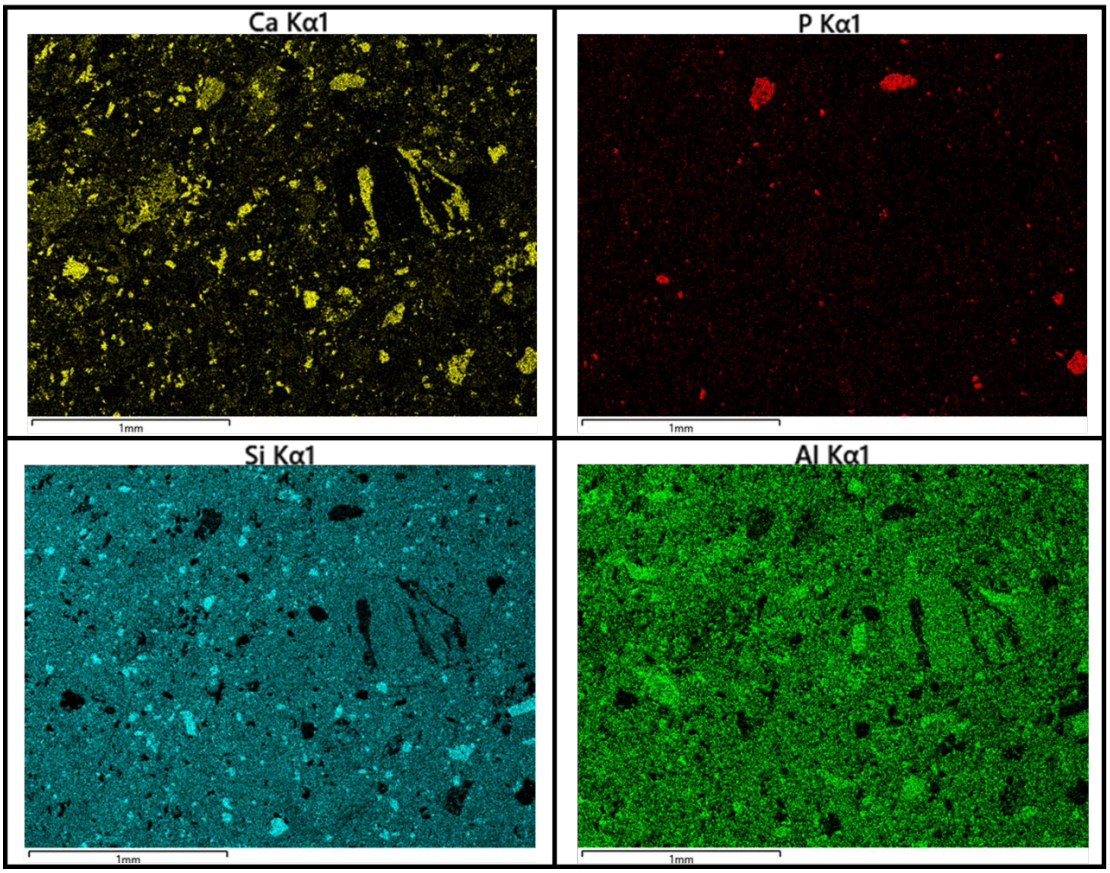

Figure 14: Focused element EDS Maps from MOR 10878-4B1 (Figure 13C) showing relative calcium (Ca), phosphorus (P), silica (Si), and aluminum (Al) concentrations.

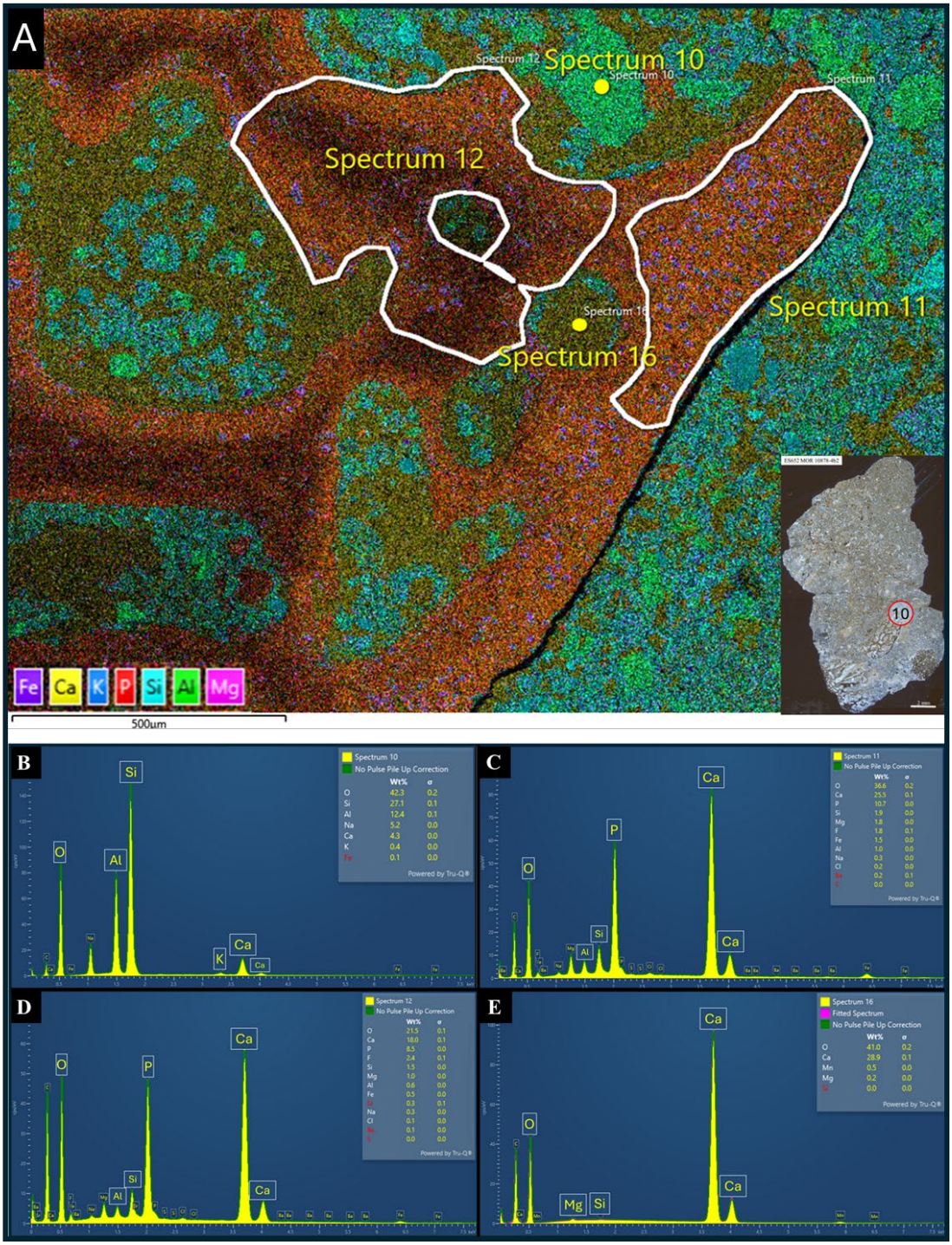

Figure 15: A) EDS Map data around Figure 10 from MOR 10878-4B2 (Fig. 7) of a bone fragment with cartilage. D - G show EDS Map Spectrum from sites. B) Spectrum site 10: external mineral from bone fragment. C) Spectrum site 11: area of possible ossified cartilage. D) Spectrum site 12: bone fragment strut. E) Spectrum site 16: Cavity within the bone fragment

Table 4: Element weight percent from oxides from EDS data for Figure 15A. From MOR 10878-4B2 on a bone fragment that has cartilage.

Location	Na	Mg	Al	Si	P	S	K	Ca	Ti	Mn	Fe	Sr	Ba	Total	CaO/ P_2O_5
Spectrum 10	7.2		23.7	57.9			0.5	6.0			0.1			95.4	
Spectrum 11	0.5	3.0	1.9	3.9	24.3	0.1		35.6			1.9		0.2	71.4	1.5
Spectrum 12	0.4	1.7	1.2	3.2	19.6	0.1		25.2			0.6	0.4	0.1	52.5	1.3
Spectrum 16		0.3		0.1				39.1		0.7				40.1	

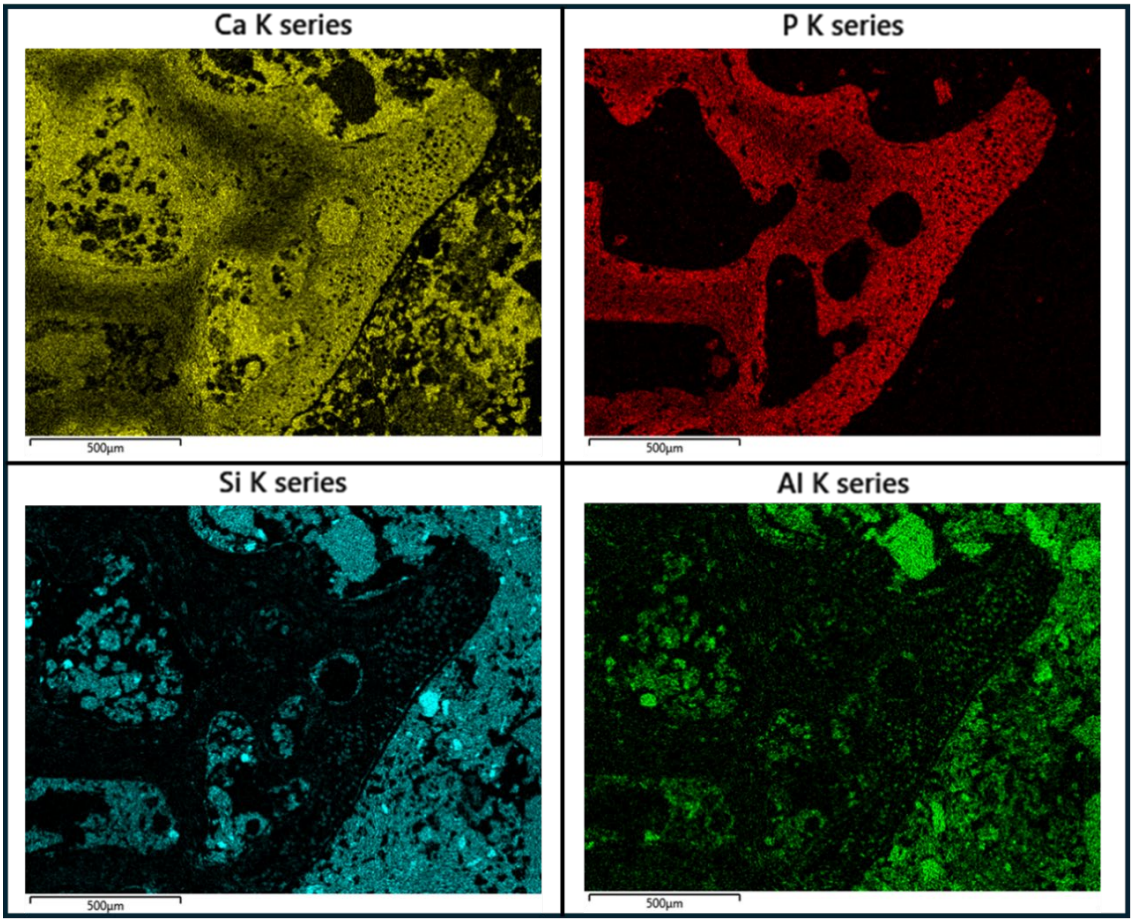

Figure 16: Focused element EDS Maps from MOR 10878-4B2 (Figure 15A) showing relative calcium (Ca), phosphorus (P), silica (Si), and aluminum (Al) concentration.

EDS data shows a more detailed picture than the pXRF. From pictures of the slides, the matrix of the surrounding sediment consisted of poorly sorted, subangular clasts (Fig. 13A). In slide MOR 10878-4B1 (Fig. 7, 13A, B), the EDS spectrum (Figs. 13C, 14) indicates that the surrounding sediment is predominantly composed of Si and Al, with Ca and Fe being the next most abundant elements in weight percent (Fig. 13D, G; Table 3). In the surrounding sediment, there are non-connected areas or pockets of P (Fig. 14; Table 3). Additionally, the Ca signals correspond with these pockets or are found in similar pockets (Fig. 14). Traces of Na, K, and Ti are also present within the surrounding sediments. Some EDS data from areas with bone fragments (Figs. 15, 16) indicate significantly higher levels of Ca and P, while exhibiting lower levels of Si and Al (Fig. 15D, F, G).

The trabecular bone (strut-like structures) is composed primarily of P and Ca (Fig. 15F; Table 4), a composition consistent with bone (Northwood, 2005). In the spaces between these structures, the composition is mostly Ca, Si, and A, with traces of Na and K (Fig. 15E, Table 4). These cavities are likely filled with calcite, as indicated by the presence of Ca, and with silicate minerals such as feldspars and quartz. The edge of the dark mass in MOR 10878-4B2 (Fig. 17) has high Ca and P with only traces of Si, Al, Fe, and Mg (Fig. 18; Table 4). This is consistent with the previously observed bone fragments. Interestingly, the empty spaces within the P map between the bone are primarily filled with Ca, likely calcite, with slight traces of Mn (Fig. 17F; Table 5). This means there is little infill from the surrounding sediment into this cavity. A fragment (Fig. 19) within MOR 10878-4B3 with potential Haversian systems has similar amounts of P and Ca (Figs. 19,20). However, it is notable that there are higher amounts of Si and

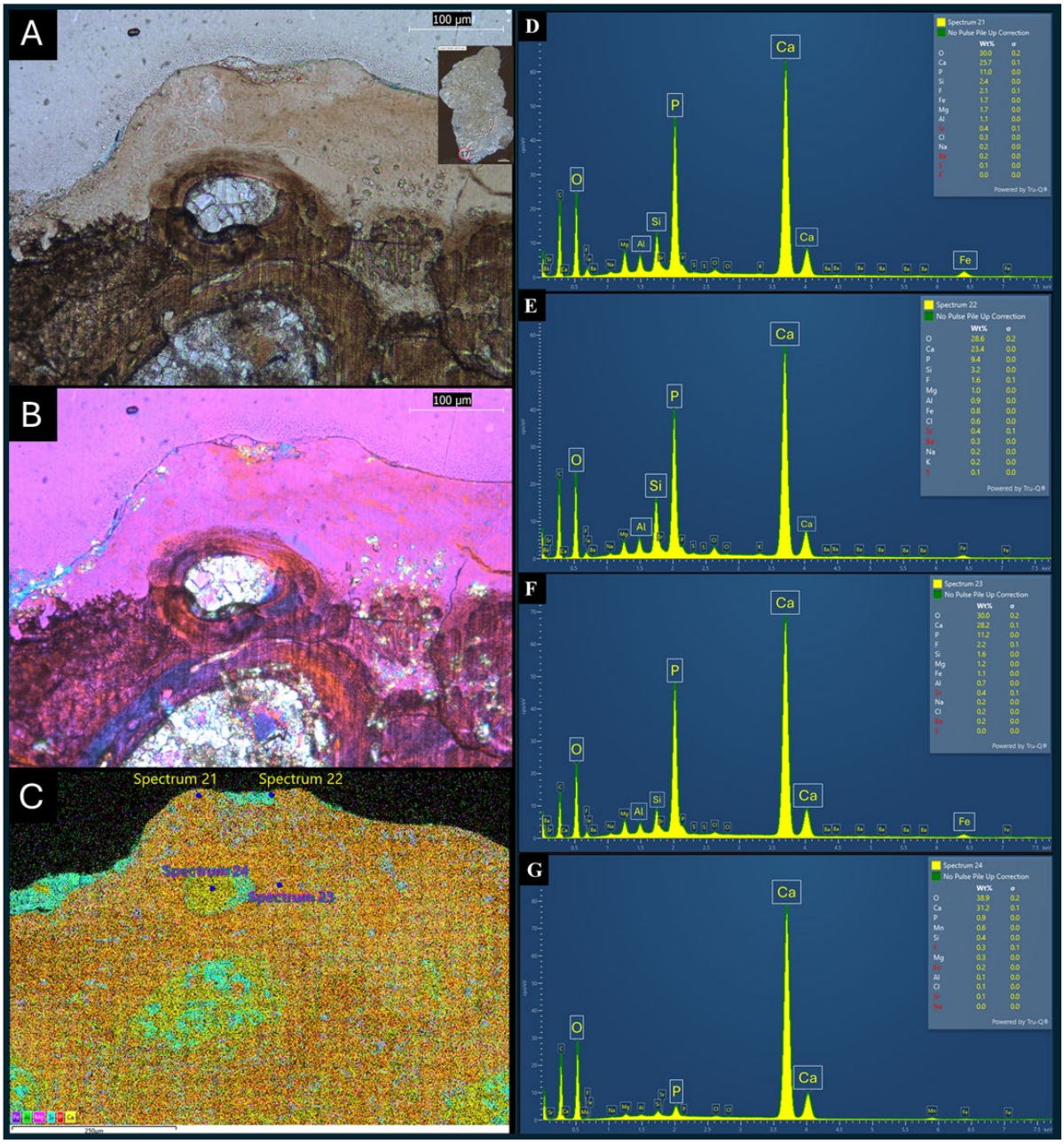

Figure 17: A) Photomicrograph obtained using a Nikon Eclipse LV100 POL Petrographic microscope with a Leica EC4 digital camera on a thin section slide (ES 654 MOR 10878-4B2) under 20x magnification. B) Same photomicrograph with cross-polarization and interference colors from a lambda plate near the edge of the dark mass. C) EDS Map data from MOR 10878-4B2 at the edge of the dark mass. D - G show EDS Map Spectrum from sites. D) Spectrum site 21. E) Spectrum site 22. F) Spectrum site 23. G) Spectrum site 24.

Table 5: Element weight percent from oxides from EDS data for Figure 17C. From MOR 10878-4B2 on the edge of a bone in the dark mass.

Location	Na	Mg	Al	Si	P	S	K	Ca	Mn	Fe	Sr	Ba	Total	CaO/ P_2O_5
Spectrum 21	0.3	2.9	2.2	5.1	25.3	0.1	0.1	36.0		2.2	0.5	0.3	74.9	1.4
Spectrum 22	0.3	1.6	1.8	6.9	21.6	0.2	0.2	32.8		1.0	0.5	0.3	67	1.5
Spectrum 23	0.3	1.9	1.4	3.5	25.7	0.1		39.5		1.4	0.5	0.2	74.4	1.5
Spectrum 24	0.1	0.5	0.2	0.9	2.07			42.5	0.8	0.2	0.1		47.3	20.6

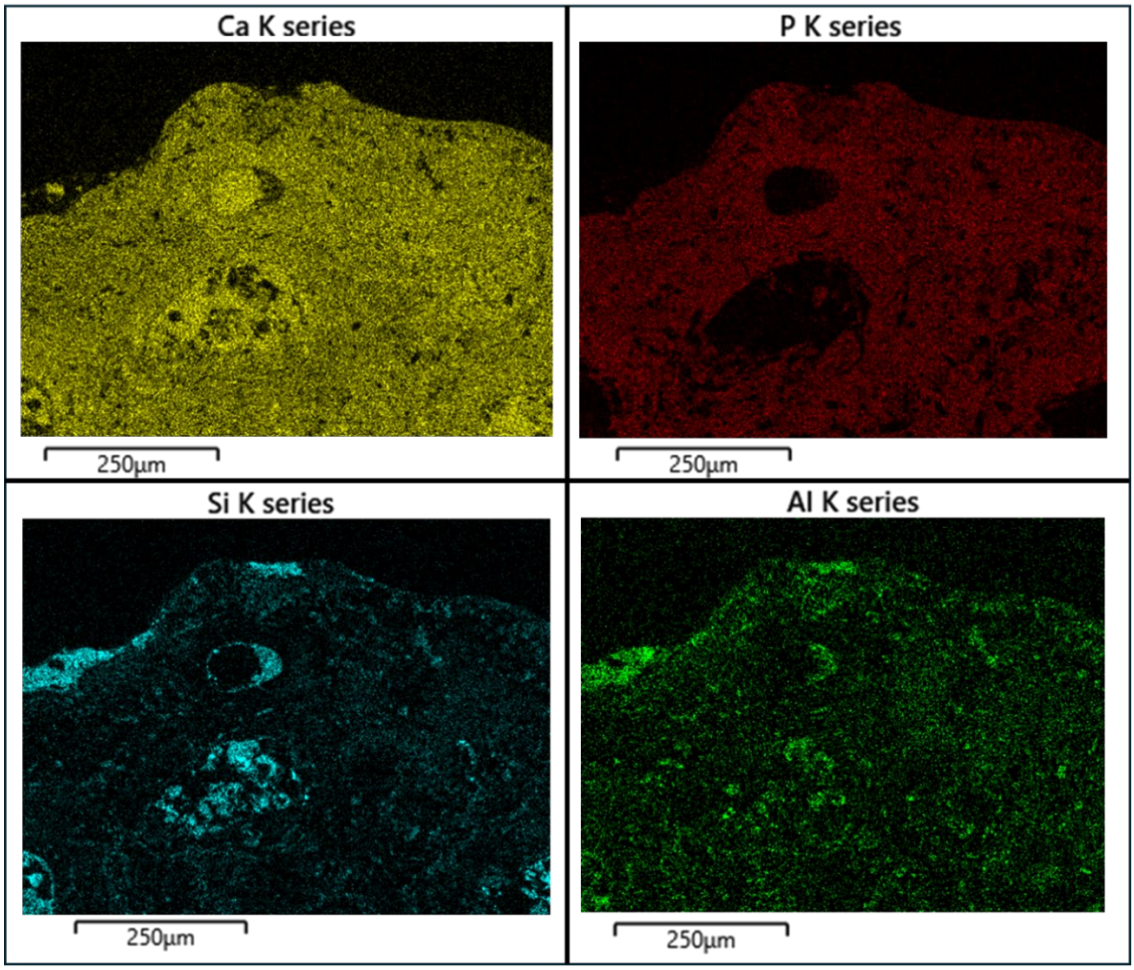

Figure 18: Focused element EDS Maps from MOR 10878-4B2 (Figure 17) showing relative calcium (Ca), phosphorus (P), silica (Si), and aluminum (Al) concentrations.

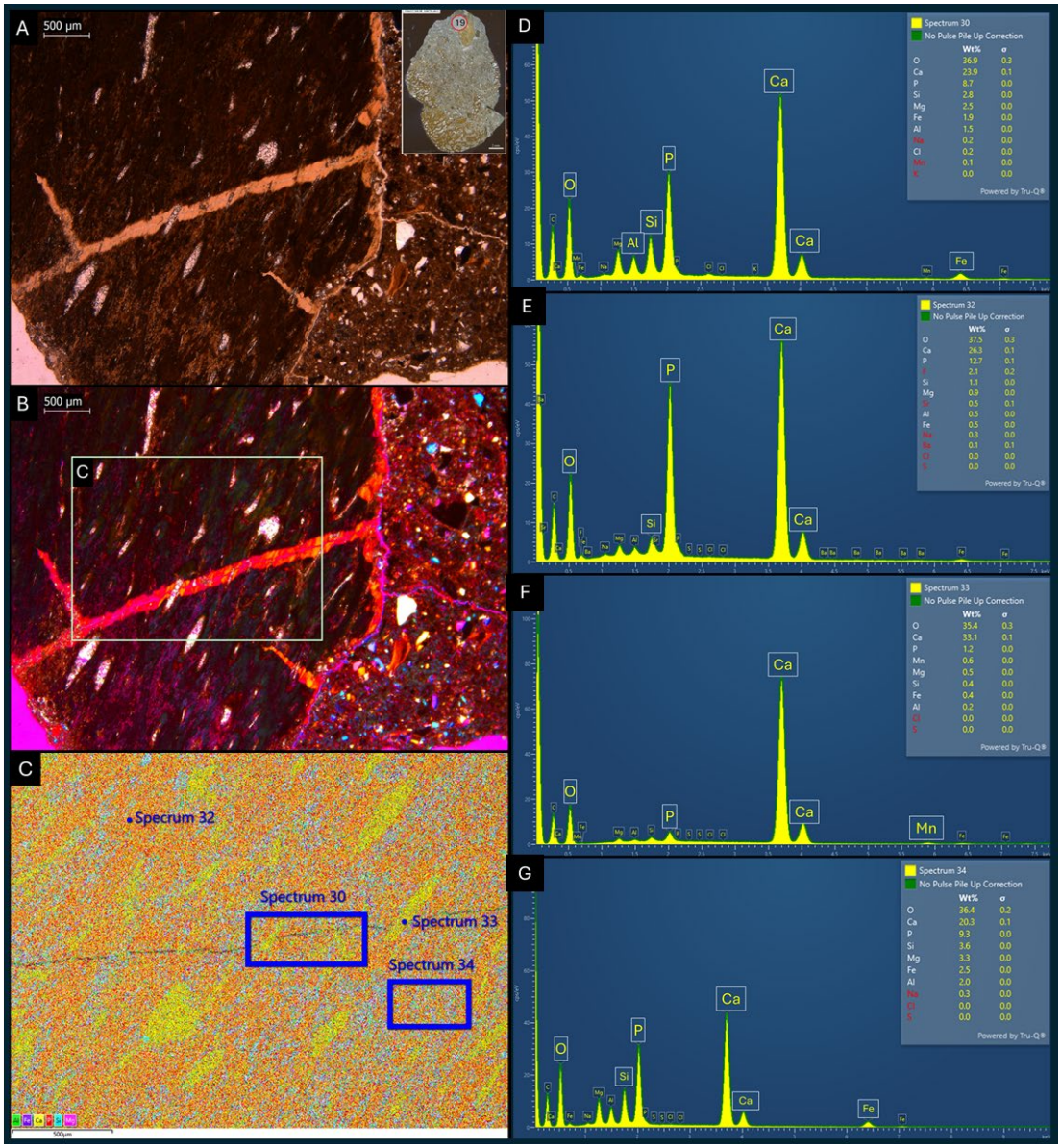

Figure 19: A) Photomicrograph obtained using a Nikon Eclipse LV100 POL Petrographic microscope with a Leica EC4 digital camera on a thin section slide (ES 654 MOR 10878-4B3) under 2x magnification under normal light. B) Photomicrograph with cross-polarization and interference colors from a lambda plate. The bone fragment has both primary and secondary osteons. C) EDS Map data from the boxed area of MOR 10878-4B3(Fig. 7) of a bone fragment with Haversian Systems. D - G show EDS Map Spectrum from sites. D) Spectrum site 30: Spot analysis near the optically altered area of bone. E) Spectrum site 32: spot analysis within bone for comparison. F) Spectrum site 33: mineral crossing, central crack, and altered area. G) Spectrum site 34: General analysis of bone area near crack.

Table 6: Element weight percent from oxides from EDS data for Figure 19C. From MOR 10878-4B3 on a potential cortical bone fragment.

Location	Na	Mg	Al	Si	P	S	K	Ca	Mn	Fe	Sr	Ba	Total	CaO/ P_2O_5
Spectrum 30	0.3	4.1	2.8	6.0	19.9		0.1	33.4	0.2	2.5			69.2	1.7
Spectrum 32	0.4	1.5	1.0	2.4	28.9	0.1		36.7		0.7	0.6	0.1	72.3	1.3
Spectrum 33		0.9	0.4	0.9	2.6	0.0		45.4	0.8	0.5			51.5	17.5
Spectrum 34	0.4	5.4	3.7	7.6	21.2	0.1		28.3		3.3			69.9	1.3

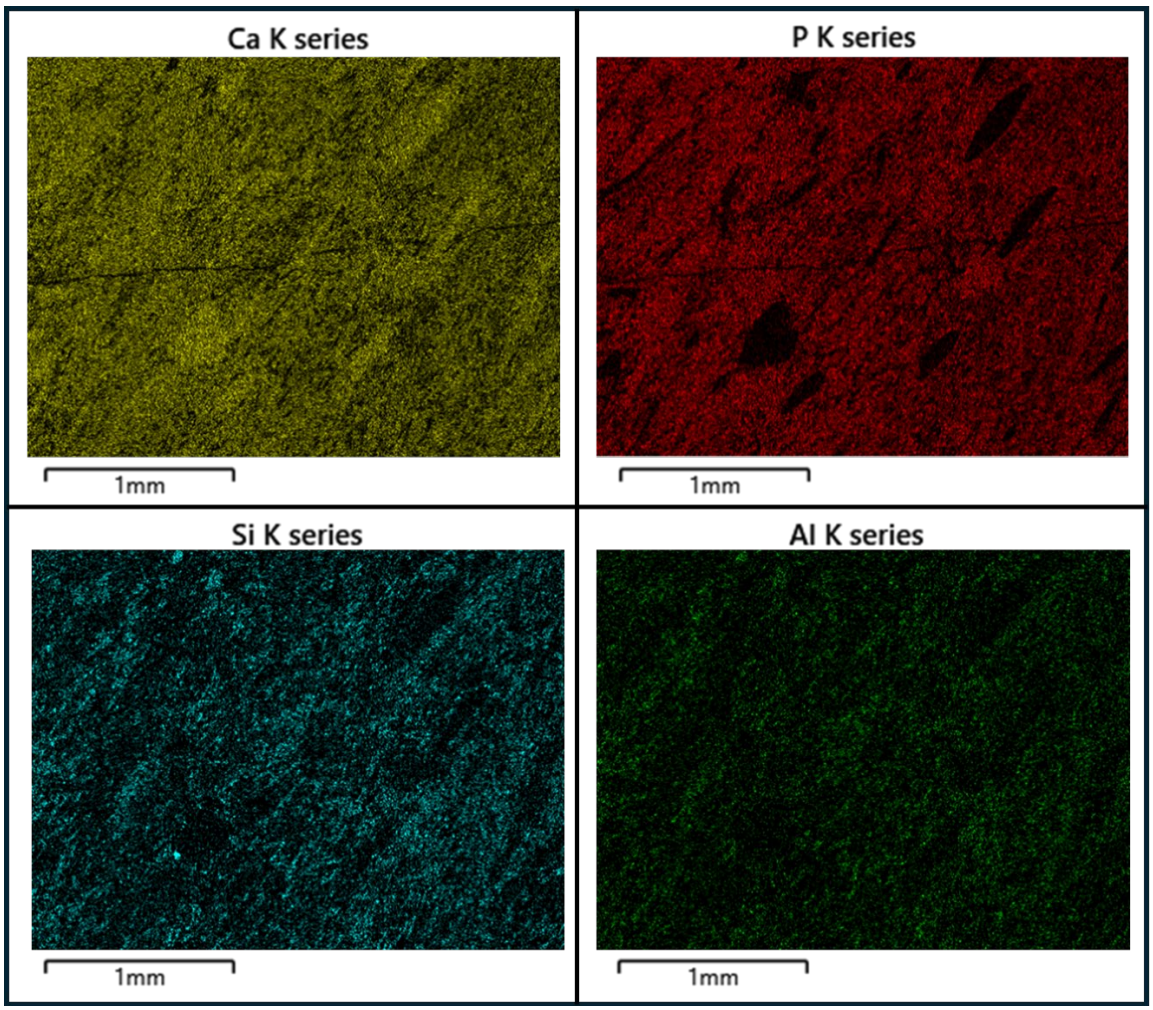

Figure 20: Focused element EDS Maps from MOR 10878-4B3 (Figure 19C) showing relative calcium (Ca), phosphorus (P), silica (Si), and aluminum (Al) concentrations.

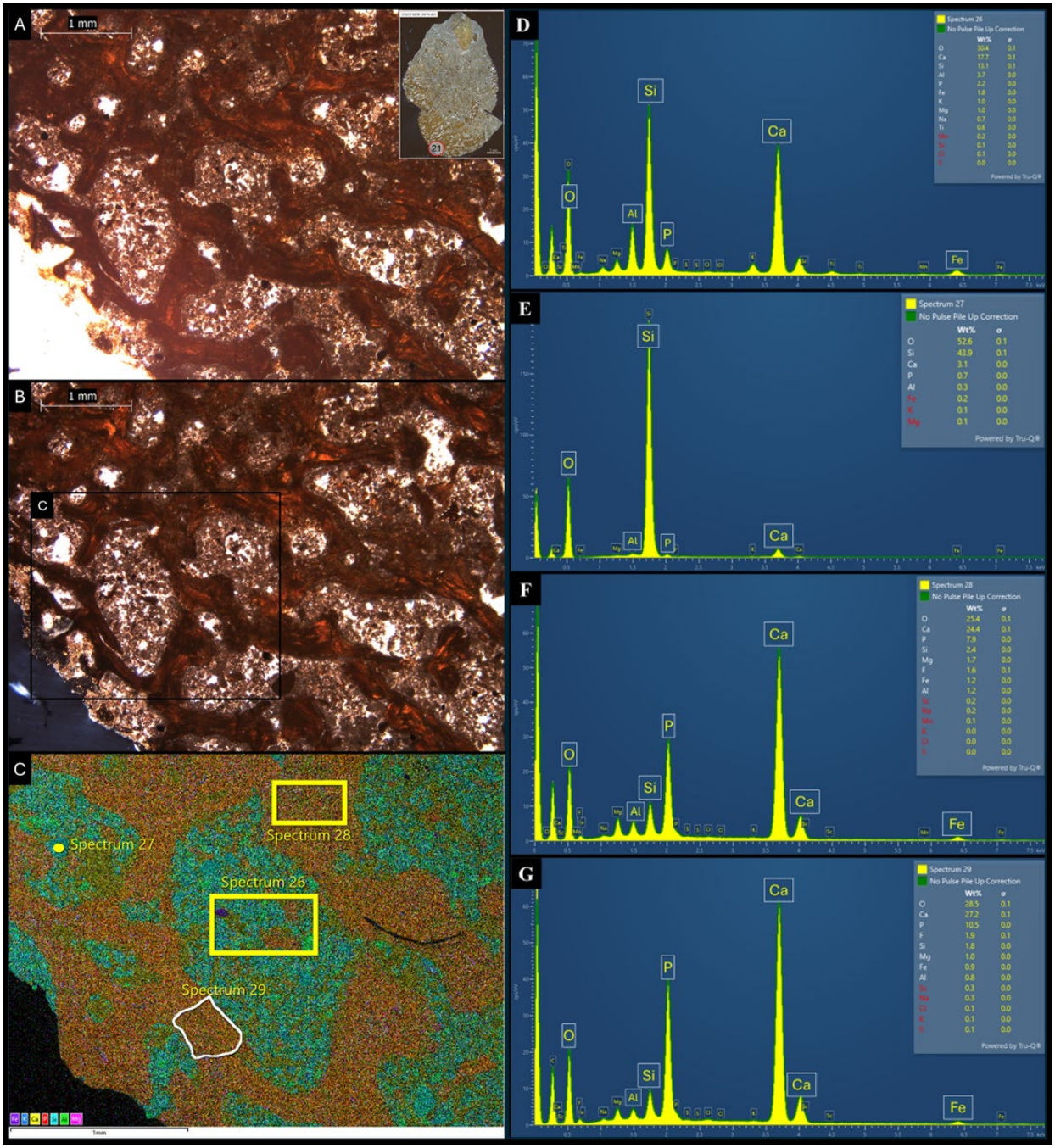

Figure 21: A) Photomicrograph of dark mass edge obtained using a Nikon Eclipse LV100 POL Petrographic microscope with a Leica EC4 digital camera on a thin section slide (ES 654 MOR 10878-4B3) under 2x magnification under normal light. B) Photomicrograph with cross-polarization. C) EDS Map data from the boxed area. D - G show EDS Map Spectrum from sites. D) Spectrum site 26: Generalized area within cavity. E) Spectrum site 27: Point analysis within cavity. F) Spectrum site 28: Generalized area of dark mass. G) Spectrum site 29: Dark mass strut near the edge of the specimen.

Table 7: Weight percent of elements from EDS data for Figure 21C. From MOR 10878-4B3 from the edge of the dark mass.

Location	Na	Mg	Al	Si	P	S	K	Ca	Sc	Ti	Mn	Fe	W	Total	CaO/ P_2O_5
Spectrum 26	0.9	1.7	7.0	27.8	5.0	0.1	1.3	24.8	0.2	1.0	0.3	2.3	0.1	72.4	4.9
Spectrum 27		0.2	0.5	93.8	1.7		0.2	4.4				0.2		101.0	2.6
Spectrum 28	0.3	2.8	2.2	5.1	18.0	0.1	0.1	34.2	0.3		0.1	1.6		64.8	1.9
Spectrum 29	0.4	1.7	1.5	3.9	24.1	0.1	0.1	38.1	0.4			1.2		71.4	1.6

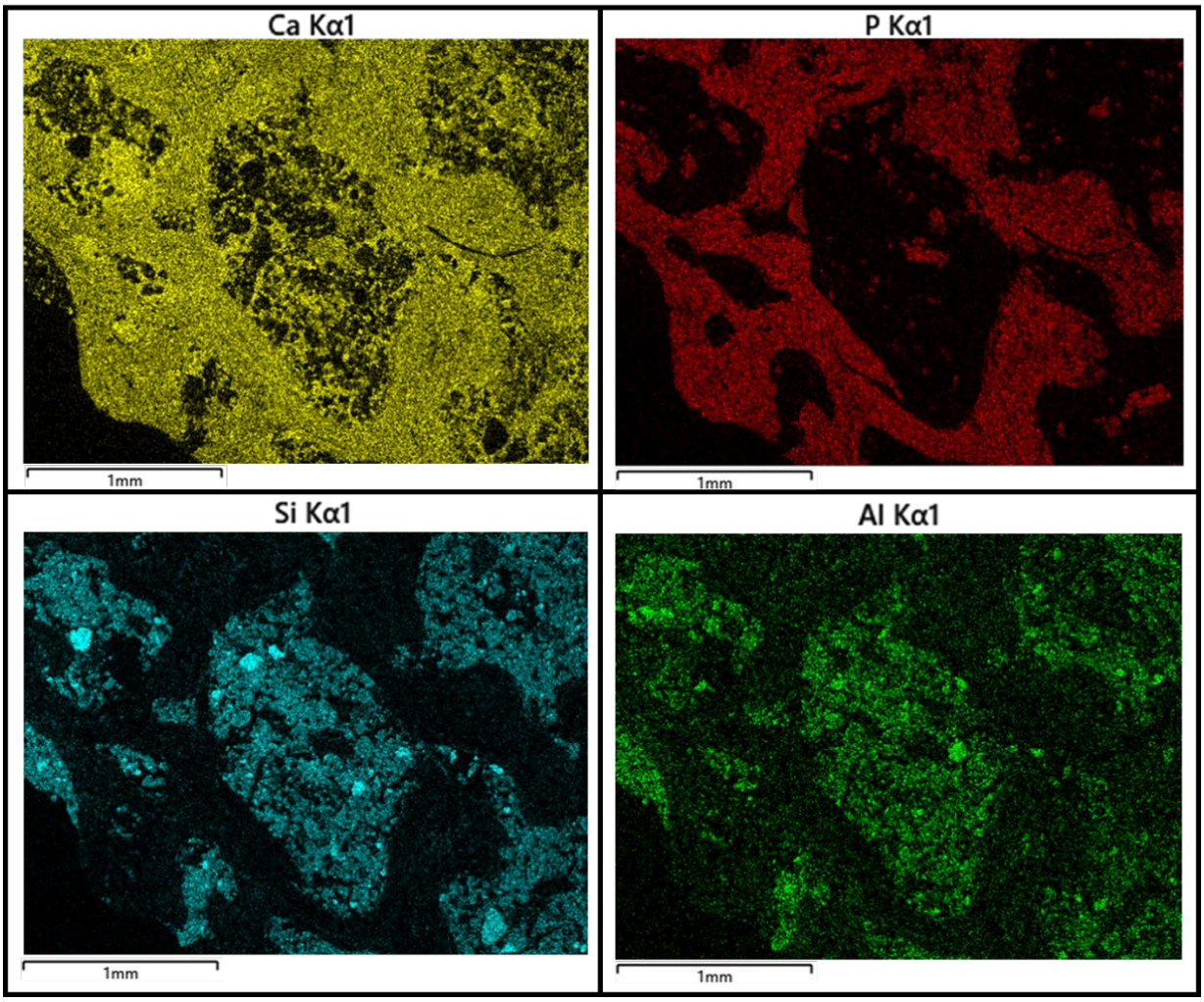

Figure 22: Focused element EDS Maps from MOR 10878-4B3 (Figure 21C) showing relative calcium (Ca), phosphorus (P), silica (Si), and aluminum (Al) concentration.

Al, up to 7.6 and 3.7 percent of the atomic weight, respectively, within the fragment (Fig. 19D-G; Table 6).

Another area of the dark mass, located near the edge of the Dark Mass on MOR 10878-4B3 and not directly associated with any other bone fragments (Fig. 21), exhibits a similar composition to that observed in the bone fragments. This part of the dark mass is located on a different slide (MOR 10878-4B3) than what is observed in Figure 17 (MOR 10878-4B2), but they may be connected and part of the same structure. The strut-like structures are composed primarily of Ca and P, likely calcium phosphate (Figs. 21D-G, 22; Table 7). The cavities in between are filled with silicate minerals and calcium deposits, possibly calcite (Figs. 21D-G, 22). This fill differs in color and texture from the surrounding sediment, with better sorting (Fig. 21A, B). Unlike that observed in other fragments and the surrounding sediment, some P is detected within these cavities as well, though not as much as seen in the bone (Fig. 22; Table 7).

CT and Synchrotron data

Both CT and synchrotron scans show a clear distinction between the surrounding sediment and the main body of the dark mass or bone fragments (Figs. 23, 24, 25; Supplementary Videos 1-3). For identification purposes, the dark mass includes the bone seen on the dorsal portion of the specimen, labeled M in figures 24 and 25, as well as the lighter-shaded sediment (in scans) around these fragments, labeled MS in figures 24D and F. The surrounding matrix displays grains of varying densities, most of which appear lighter in the synchrotron data and darker in the CT data compared to bone. In contrast, the dark mass exhibits a more uniform density spectrum. In synchrotron data, it is even possible to distinguish cavities within the dark mass or bone fragments from the surrounding bone (Figs. 23, 24, 25) as the cavities appear

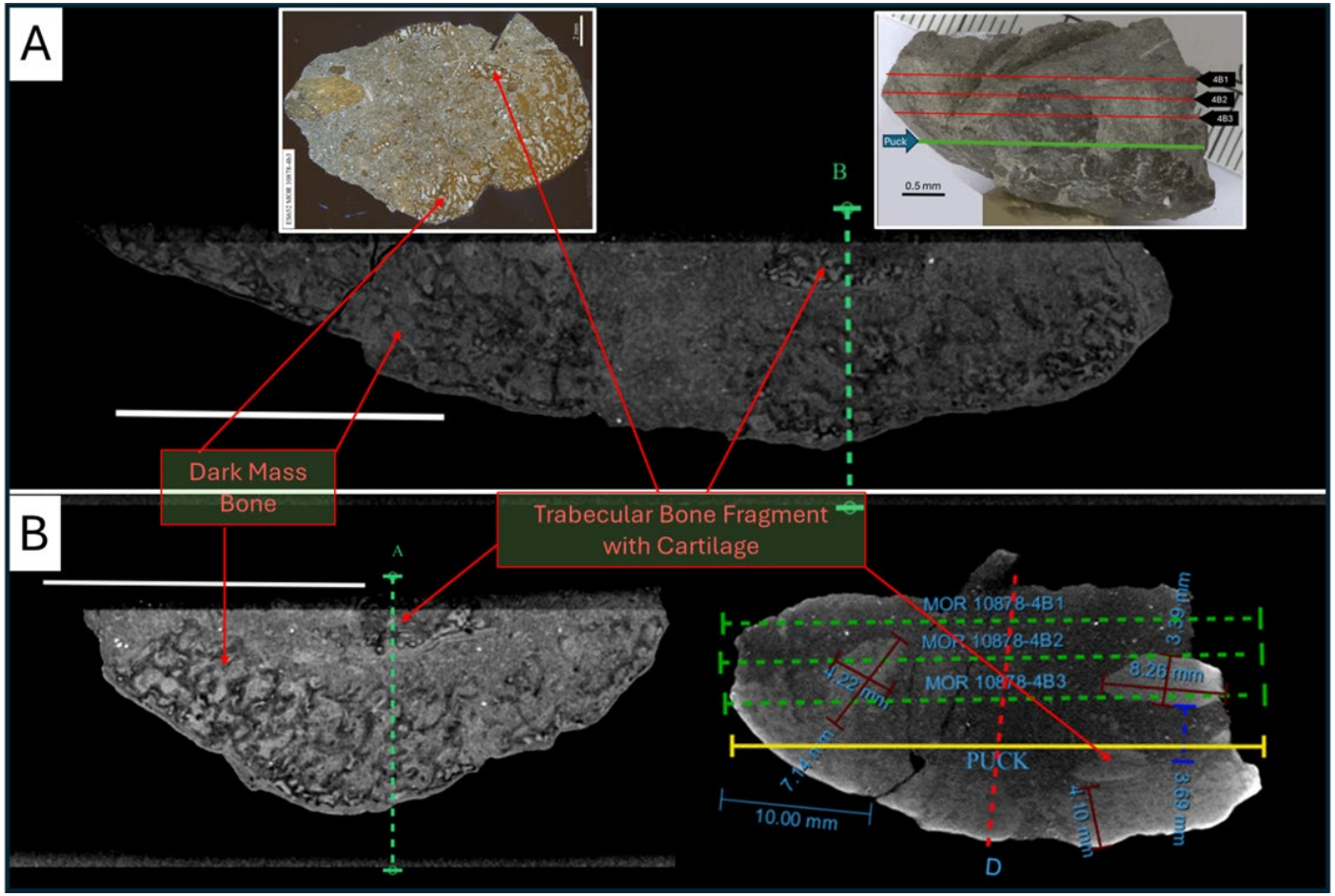

Figure 23: Synchrotron scan of the remaining puck of MOR 10878-4B from the thin sectioning. Shows the contrast of trabecular bone fragments when seen in thin-section, CT scans, and synchrotron scans. Similar features are seen in thin-section, CT scans, and Synchrotron scans, including bone fragments with possible cartilage and the trabecular bone of the dark mass. Additional figures are used as a reference to a similar or possibly identical feature. A) Longitudinal axis scan of the puck sample. B) Width axis scan of the puck sample.

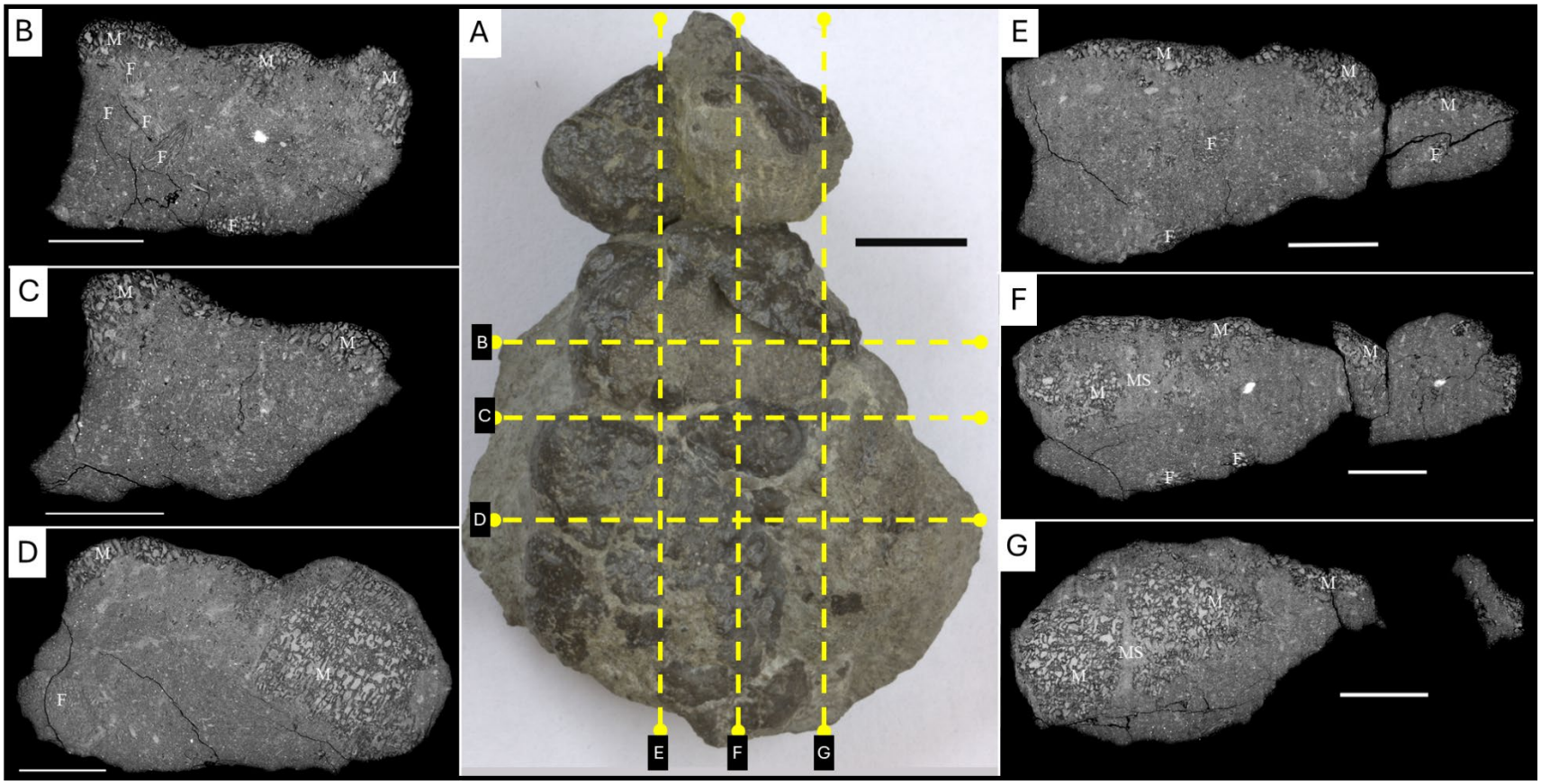

Figure 24: Scale bars = 1 cm. A) Top view of MOR 10878-9, mirrored to better line up with Synchrotron scans. Yellow dashed lines represent the location of medial synchrotron scans. B-G) are Medial synchrotron scans of MOR 10878-9. Lighter areas of the matrix (higher density) may indicate invertebrate burrows. Annotation abbreviations: M, Dark mass trabecular bone; MS, Dark mass sediment; F, Bone Fragments. B-D) Medial scans across the width axis of the specimen. E-G) Medial scans of the longitudinal axis of the specimen.

lighter. Some bony struts appear to extend from the dark mass and bone fragments around it, giving the area a mottled, amorphous appearance that changes rapidly as you progress through the specimen (Figs. 23, 24, 25). The bone fragments have distinct edges and features throughout the images, with consistent spaces within them. Trabecular bone, as identified in synchrotron scans and thin sections (Figure 23), shows trabeculae that were difficult to identify in CT scans alone due to the low resolution. On the edges of some fragments, compact lighter areas are observed, which potentially correspond with cartilage (Fig. 23).

In MOR 10878-9, the eight fragments (Fig. A3; Supplementary Video 6) either extend from the edge of the mass into the matrix or are further into the matrix, but do not reach the surface of the specimen (Fig. 24B). Many are next to each other, or are in close proximity, within a few mm, to the dark mass or the sediment around it. The fragments range in length from 0.77 mm to 30.22 mm, in width from 0.6 mm to 12.04 mm, and in depth from 0.37 mm to 5.60 mm. The majority of fragments are shorter than 5 mm in length and width, with only eight exceeding the length and five exceeding this width, and only three fragments exceed a length of 10 mm. Some of the fragments seen in MOR-10878-4A (Fig. A2; Supplementary Video 4) appear to have a cylindrical appearance (Fig. A2; Table A1: ID 7, 10, 11, 12), but proper identification is difficult at this time. Many of the fragments identified within the matrix are oriented somewhat parallel to the dark mass. This is observed with most of the flat fragments seen in MOR 10878-9, where their shortest axes face the dark mass and their longest axes are oriented in a similar plane (Fig. A3).

The dark mass of MOR 10878-4B (Supplementary Video 2,5) itself appears to have characteristics similar to those observed in the bone fragments (Fig. 23). Many of the filaments

extending into the surrounding matrix resemble trabecular bone fragments found elsewhere in the specimens, but with larger cavities and bone struts. Coprolites have been found to contain cavities before, likely due to the material within them breaking down and being replaced; however, they do not exhibit the same relative repeated pattern as seen within the mass (Shillito et al., 2020). This would likely imply that the majority of the dark mass is bone rather than the coprolite's groundmass. This is corroborated by the thin-section observations and EDS data in Figures 17 and 21, which pertain to the dark mass areas. This implies that the structure of the dark mass is primarily composed of trabecular bone fragments, with some possibly containing cartilage (Figs. 17A, 25C, D). These dark mass fragments range in size, with the longest being around 32 mm along its longest axis. However, this fragment is relatively thin at less than 5 mm in depth. The largest dark mass fragment by volume is 20.3 mm x 20.2 mm x 12.3 mm. The sediment between these fragments (MS in Fig. 24F, G) is slightly denser than the surrounding sediment, showing up as a lighter shade than the matrix in the synchrotron scans. This could imply that it is somewhat different in composition, but this is difficult to say at the moment.

Other inclusions have been observed in addition to bone fragments. Within the surrounding matrix of the specimens, there are notable ovoid inclusions with subtle but distinct edges, approximately 1-2 mm in diameter and about 2-2.5 mm in length (Figs. 25D, 26D). One inclusion (Table A1: ID 22) is 1.63 mm by 1.26 mm. The inclusions are often associated with one another or arranged in a line (Fig. 26D). These objects appear to be composed primarily of minerals similar to those of the surrounding matrix, with a change in density at the outer surface being the primary distinguishing characteristic between the inclusions and the matrix. We speculate that these inclusions may be fecal pellets from these invertebrates as they pass through

the sediment. These structures share dimensions similar to those of *Edaphichnium isp*., previously described from the Egg Mountain quarry (Freimuth et al., 2021).

These potential invertebrate fecal pellets can sometimes be associated with lighter regions within the specimens' surrounding matrix. These areas of differing density to the surrounding matrix sometimes extend to the dark mass fragments of the specimens (Figs. 24B-D and 26A-D). These areas are generally in lines that weave through the matrix. These are interpreted here as potential burrows from these invertebrates as they interact with bone fragments and dig through the sediment. These burrows seem to approach and even concentrate on portions of the dark mass (Fig. 26A, B; Supplementary Video 7). Because burrows are denser and resemble the sediment of the dark mass, it can be challenging to identify in certain scans which parts are burrows and bioturbation, and which are the dark mass sediments (Fig. 24D).

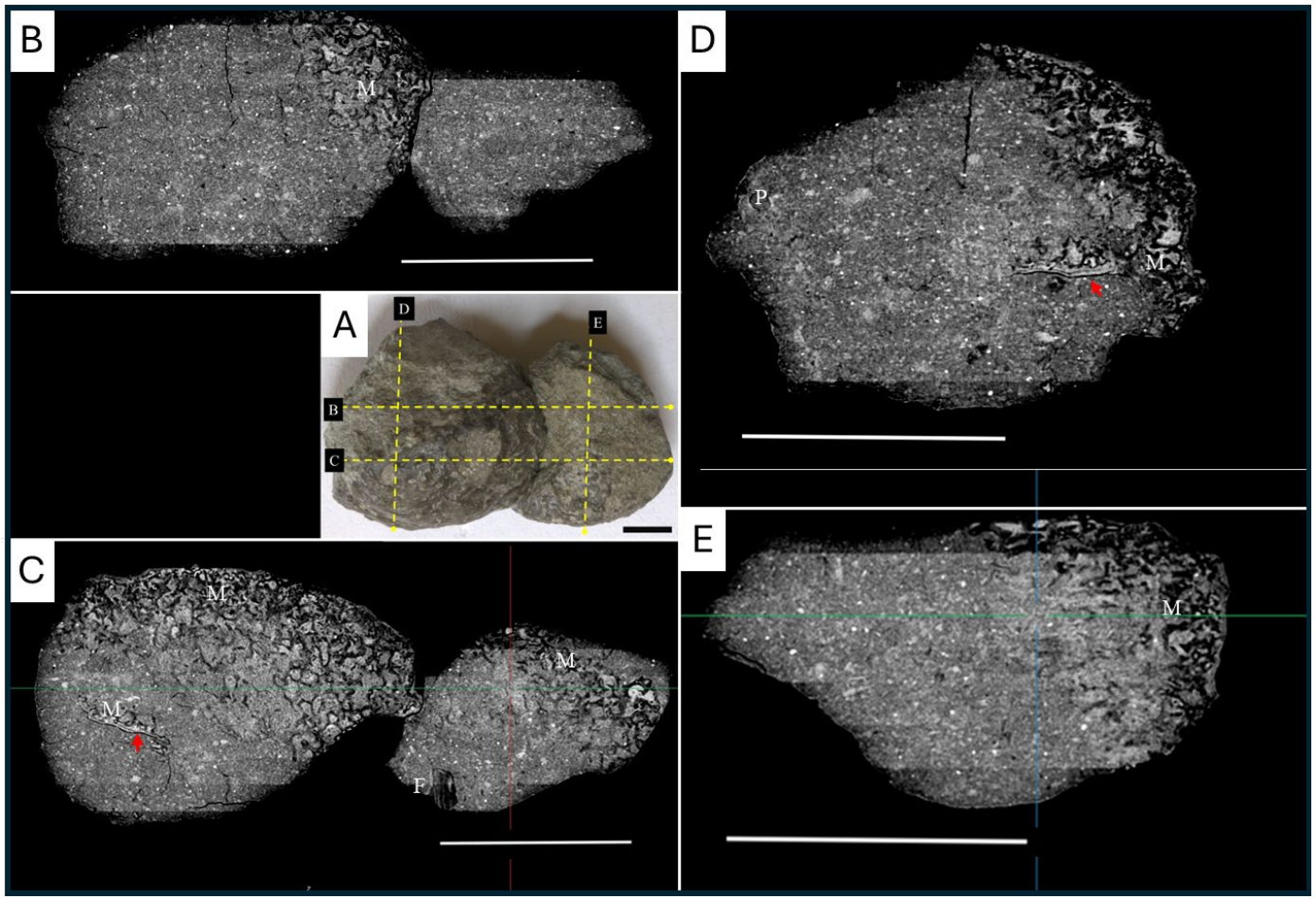

Figure 25: A) Top view of MOR 10878-4A, mirrored to better line up with Synchrotron scans. Yellow dashed lines represent the location of medial synchrotron scans. B-E) are medial synchrotron scans of MOR 10878-4A. Lighter areas (higher density) of trabecular bone (red arrows) may indicate cartilage portions of the bone. Annotation abbreviations: M, Dark mass trabecular bone; F, Bone fragments; P, Fecal pellet (invertebrate). B-C) Medial scans across the width axis of the specimen. D-E) Medial scans of the longitudinal axis of the specimen.

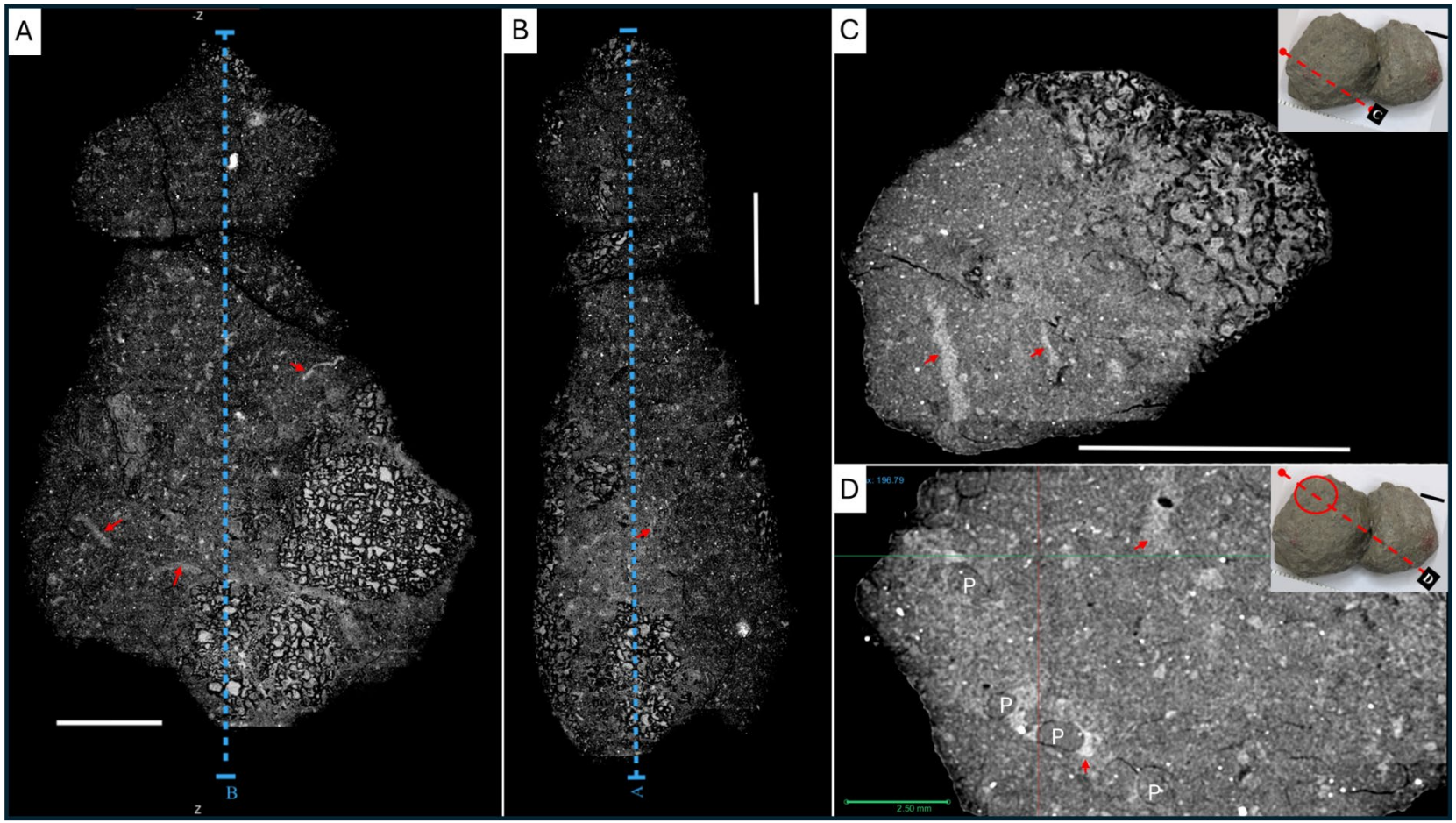

Figure 26: Close-ups of areas in 28B. Area near dark mass/bone with noted difference in density and texture of matrix that may indicate a possible burrow. Area in the matrix that shows noted difference in density and texture, and ovoid structures that are possibly invertebrate coprolites. A) Top view of medial scan of MOR 10878-9. B) lateral view of medial scan of MOR 10878-9. C) Cross-sectional view of MOR 10878-4A. D) Close up another cross-sectional view in MOR 10878-4A.

DISCUSSION

Specimen Analysis

The three MOR 10878 specimens all share similar features: a dark, semi-glossy mass with an elongated, lobate top, set within a mudstone matrix. When examining the surrounding matrix, it is notable that it is primarily held in place by siliciclastic grains and cement rather than calcareous ones, as observed in other parts of the Willow Creek anticline (Martin & Varricchio, 2011). The grains themselves appear to be general clay minerals (Fig. 13C, D, E, G), with some bone fragments (Fig. 13F). The bone fragments beneath the dark mass appear to have a similar orientation to the dark mass. These fragments are relatively small, and most are thin. In the thin sections (Figs. 7,8), there are portions of the edges of fragments and the dark mass fragments that have different optical properties than the bone that are connected to them (Figs. 10,11,17,19). While these portions of altered bone seem to have the same chemical properties seen in the bone (Figs. 18, 20), they are clear and lack the brownish tint and texture of other parts of the bone fragments.

These dark masses are mostly fragmented bone, as indicated by the data from both 3D scans and thin sections. This is also corroborated by the EDS data, which show that the dark mass interior is primarily composed of calcium phosphate, with the cavities filled with fine-grained dark infill sediments or calcium carbonate. This fill appears different from the surrounding sediments in texture. There are some of the cavities where there are noticeable increases in P, though the direct source of these signals isn't clearly understood. Both the thin section and 3D scans reveal that most of the dark masses are trabecular bone, with more rounded edges at the top of the specimen and more jagged edges oriented toward the interior. The bone

fragments of the dark mass are closely packed together (Figs. 23, 24) and seem to be oriented in the same direction. Most of these dark mass fragments are thin, with only a few exceeding 5 mm in the specimens. However, the largest fragment of the dark mass, at 20.3 mm x 20.2 mm x 12.3 mm, suggests that larger portions of the bone are also present.

In the synchrotron scans, multiple bone fragments are observed throughout the specimens. The fragments range in size from 0.7 mm to 30.22 mm, with the majority shorter than 5 mm. These fragments are closely associated with the dark mass, with only a few being more than 1 cm away from the presumed main body of the dark mass. Many of the flatter fragments also share an orientation with the dark mass, further supporting their association with each other. In addition to these fragments, the synchrotron scans also show invertebrate burrows and likely fecal pellets associated with the dark mass. Many of these burrows are concentrated on or near the dark mass.

The burrows and invertebrate fecal pellets in the specimens indicate a well-worked system with significant movement through the sediment (Freimuth et al., 2021). The producer is likely the same one that produced *Edaphichnium* isp., i.e., subsurface-feeding detritivores such as earthworms, millipedes, or beetles (Freimuth et al., 2021). These detritivores may also explain the flecks of phosphatic material visible throughout the surrounding sediment, which are either being dragged away or reprocessed by these detritivores. The activities observed in the specimens of these invertebrates would have likely only occurred in non-fluvial sediments (Freimuth et al., 2021). These occurrences suggest that, before and during burial, the specimens were likely in subaerial sediments before burial (Thulborn, 1991; Hollocher & Hollocher, 2012; Freimuth et al., 2021).

The preservation of the specimens is unusual, as the dark mass is intact, but the remaining fragments appear to have broken away from the main body of the bromalite. It is important to note that the top of the specimens, specifically the fragments of the dark mass, are more closely packed than the fragments found in the rest of the surrounding rock. The presence of invertebrate traces implies that they fed on the matter near the dark mass. This could explain why the fragments are so scattered in the matrix. The invertebrates would have broken down parts of the specimens, bioturbated the soil, and carried away fragments from the dark mass.

The dark mass itself may have been exposed to the air. Allowing it to harden through desiccation makes it more difficult to break down by either detritivores or fluvial activity. The phosphatic and calcitic signals (Fig. 13) within the surrounding matrix may have resulted from diagenesis or the breakdown of the specimens over time, which may also have helped small pieces detach from the dark mass. There are noted calcareous mudstone deposits at Egg Mountain that could be the source of the Ca (Panascí & Varricchio, 2020). However, the reduced P and Ca signals in the surrounding matrix (Figs. 13, 14) indicate that preservation of the specimens did not occur due to environment-induced phosphatization caused by excessive Ca or P.

The dark mass itself has a unique appearance and preservation. The luster of some specimens may be due to the application of a consolidant, but this does not explain the somewhat duller, natural luster on parts of the specimens that lack this coating. The roundedness of the top parts of the specimens may be due to abrasion, though it seems to be lacking on the underside of the dark mass fragments in CT and Synchrotron scans. Another reason for the smoothness may be due to etching from digestive enzymes and stomach acid, which have been noted to polish

bones that have been either regurgitated or passed through the digestive tract (Hockett, 1996; Sanz et al., 2001; Fernández-Jalvo et al, 2014; Fernández-Jalvo & Andrews, 2016; Klug & Vallon, 2019). If this is the case, it could also explain the darker color of the fragments' surfaces, as digestive enzymes have been observed to discolor the outer surfaces of bones (Hockett, 1996; Klug & Vallon, 2019). However, many bones within the Two Medicine Formation are darker in color, likely due to diagenetic processes in the sediment. Therefore, the change in color from the exterior may not conclusively indicate staining of the fossil; it may instead result from a diagenetic process within the sediment. Another interesting feature is the optically different portions of bone seen in thin sections of the dark mass or associated fragments. This alteration could be due to corrosion of the external surface, resulting from chemical changes induced by hydrologic factors or digestive enzymes (Fernández-Jalvo & Andrews, 2016). However, it is also possible that the dark brown coloring in the interior of the bone is what has been altered, as the ossified cartilage portion of bone fragments seems relatively intact, with lacunae of chondrocytes seemingly visible, while the osteocytes are more challenging to observe in the interior of the bone. It is not clear as to why this may be the case, though it may be due to some difference in the crystal structures of the interior calcium phosphate and that near the edge and in ossified cartilage.

The fragments in MOR 10878-4 and MOR 10878-9 represent different types of bone, with some being spongy trabecular bone (Fig. 10, 11) and others more dense cortical bone (Figure 9). Some of these fragments may be from the same bone, and they are likely all from the same individual, though it would be difficult to confirm. The observed features of the thin sections of MOR 10878-4B create some interesting possibilities about the nature of these

specimens. The strut-like structures seen in the thin sections (Figs. 10, 11) are the interior features of spongy cancellous or trabecular bone, as these structures share cross-sectional features of modern and even fossilized bone (Bailleul et al., 2014; Goret-Nicaise, 1984; Holliday et al, 2010; Lengelé et al., 1996).

What is interesting is how close these trabecular features are to the surface of the bone, as the cancellous material is directly under the cartilaginous areas (Figs. 10-12). There are sections of the cancellous bone that appear different under polarized light than the rest of the surrounding bone (Figs. 10,15). One possibility is that the fragments containing cartilage were near the epiphysis of a limb element. If the identification of the element is correct, the bone fragments could be on a growth plate from a juvenile individual, where the bone might intersect closely with the outer edge of the bone, and the cartilage is thicker. The softer articular cartilage that is seen on the end of a limb would likely have been destroyed, while the ossified epiphyseal cartilage remained. As it is difficult to determine how much of the epiphyseal cartilage thickness has been eroded, identifying the individual is challenging. Another interesting feature is the possible identification of secondary cartilage, often found on cranial elements that experience high stress (Bailleul et al., 2012). This would likely explain the ossified nature of the cartilage seen. Secondary cartilage has been found in most Dinosauria and has been described in ornithischian dinosaurs and modern birds (Bailleul et al., 2012). This suggests that the source of these fragments may be dinosaurian. This would also be likely if cartilage is part of a growth plate, as archosaurs are known to have thicker cartilage caps than those of other animals (Holliday et al., 2010). However, the interaction between the trabecular bone and the cartilage

seems more similar to secondary cartilage seen in cranial elements than growth plates (Bailleul et al., 2012).

The cortical bone features exhibit some secondary growth in their Haversian systems (Figs. 9, 19). This growth implies that the individual has had sufficient time to develop and is unlikely to be a hatchling (Adams & Organ, 2005). Secondary osteon growth does appear in some of the fragments (Fig. 9A), but other fragments show little overlap of osteon under λ-XPL (Figs. 9B, 19A, B), and the secondary osteons observed are few. It is also noted that the bubbly texture of the bone observed in Figure 9A may be due to the bone growing together from the remnants of fascicles from earlier stages of development, as seen in earlier examples of ossified tendons in ornithopods (Adams & Organ, 2005; Horner et al., 2016). Some of the fractures observed in the fragments may also be due to compression by sediment layers, but the bubbly texture is more reminiscent of metaplastic tissue (Horner et al., 2016). While a hatchling or early nestling with poorly formed Haversian systems with secondary growth is unlikely, juvenile is a possibility for the source. This would be further supported by the cavities near the edge of fragment 2 (Figs. 10, 11, A1; Table A1) if these represent developing osteons, which grow inward as animals age (Woodward Ballard et al., 2014; Mitchell et al., 2017).

Interpretation and Bromalite Evidence

Based on the initial observations, the original diagnosis was that the dark mass was a coprolite. While this could still be possible, other contenting possibilities must be considered as well. The simplest possibility is that the bone fragments of the specimens were transported by fluvial means during flooding, resulting in a microfossil assemblage. Small bone fragments, such as those seen in the specimens, can be easily transported in fluvial settings and could mask the

origin of a microfossil assemblage (Dodson, 1973; Korth, 1979). The surfaces of the dark mass appear rounded, possibly due to abrasion from flowing water. However, the differences in profile and the range of fragment size and shape complicate this explanation, as the sorting of elements does not necessarily align with what might be expected from fluvial transport (Kusmer, 1990). The thinner and longer fragments might not be expected to be associated with the more robust fragments. Simple fluvial transport would also not explain how the fragments that make up the dark mass are so tightly packed together, nor why they have stayed together.

A bromalite interpretation would be supported by most of the observations of the specimens. The polishing observed on the fragment on top of the specimens could be explained by gastric acid etching and enzymes on the surface of the bone as well as possibly explain the darkened color of the exterior of the fragments when compared to the interior of those fragments (Hockett, 1996; Sanz et al., 2001; Fernández-Jalvo et al, 2014; Fernández-Jalvo & Andrews, 2016; Klug & Vallon, 2019). This explanation also accounts for why most fragments are similarly oriented and closely associated with one another (Klug & Vallon, 2019). Phosphorus-rich minerals of the bones of the dark mass fragments may have leached into the sediment and phosphatized the bone fragments of the dark mass and the surrounding sediment, thus helping keep the dark mass intact (Northwood, 2005). This could be because the upper portion was exposed to air and sunlight for a more extended period, allowing it to desiccate, harden, and become more resistant to weathering and detritivores (Thulborn, 1991; Hollocher & Hollocher, 2012).

The extensive bone fragments found within the specimens indicate that the producer was a carnivore. The specimens are too large to have originated from one of the small mammals or

lizards previously described (DeMar et al., 2017; Weaver et al., 2021). The specimens also seem too small for what one might expect from anything but a very young tyrannosaurid in the region. While the deterioration of the bromalite is likely, as the bone fragments in the matrix are not as close to each other as the dark mass, more fragments or specimens might have been expected to be near the MOR specimens due to how well the dark mass fragments themselves stayed closely packed. Due to the size of the specimens, the likely producer of the bromalite was a small to medium-sized predator of the region. Understanding the potential type of bromalite may help narrow down the producer.

Coprolite or Regurgitalite

The initial interpretation of the specimens as coprolites is a possible explanation for the observed evidence. As seen in coprolites, these specimens lack articulated skeletal elements and are mainly composed of bone fragments with little identifying form (Hunt & Lucas, 2025). This interpretation would also explain why the fragments of the dark mass are rounded and closely packed (Hunt & Lucas, 2025). One possible point of contention is that although the fragments are not articulated, some are relatively large, with the longest reaching 32 mm, while others are bulky and blocky. This may have caused problems for a small predator to pass through their digestive system and could have risked compaction. This does not rule out the samples being a coprolite however, as bone fragments of this size can pass through the digestive systems of humans, who can pass objects through the stomach that are less than 5 cm long and 2 cm wide (Webb, 1988), and *Borophagus*, a wolf sized, bone eating canine, that does have coprolites that contain fragments of this size (Fig. 27 A, B) (Wang et al, 2018). It should be noted that these are two mammalian examples, one of which is named for its consumption of bone, and they may not

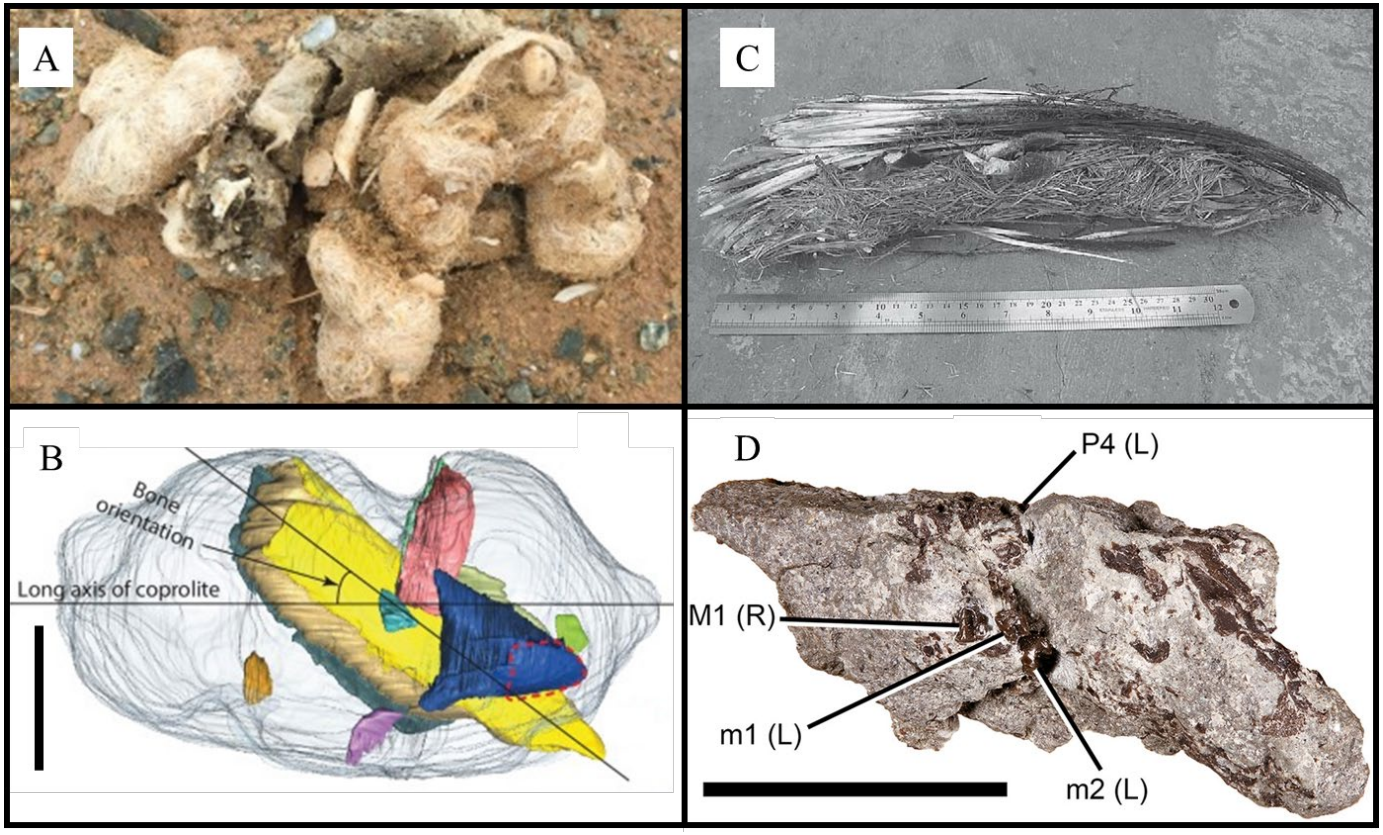

Figure 27: Trace examples from modern and fossil remains. Modified images: A-B from Wang et al. (2018); C from Plummer and McKenzie (2008); D from Freimuth et al. (2021). A) Figure 1C: Scats of extant grey wolf with bone fragments and hairs (photo by Xiaoming Wang) (Wang et al., 2018). B) MicroCT scan of *Borophagus* coprolite: LACM 158708, showing internal bone fragments. Scale: 10 mm (Wang et al., 2018). C) Figure 1: Gastric pellet believed to be that of a Komodo Dragon that contains the flight feathers from a sea bird (top of pellet) and the hoof of a juvenile Timor Deer (mid-center of pellet) surrounded by a matrix of grass. Scale: 30 cm (Plummer & McKenzie, 2008). D) Figure 3D: Representative elements of MOR 11750, potential *Troodon* regurgitilite. Associated cranial fragments and teeth of *Alphadon halleyi*. Scale: 10 mm. m/M, lower/upper molar; P, upper premolar (Freimuth et al., 2021).

be perfect analogues to predators of the Campanian. Still, they show that medium-sized animals can produce feces containing sizeable bone fragments. However, the lack of an observed distinct ground mass surrounding the other fragments in the thin sections and the surrounding sediment lacking a low Ca/P composition ratio, which would imply the presence of dissolved hydroxyapatite (Table 3) (Gordon et al., 2020; Allen et al., 2025), complicates a coprolite interpretation. It is possible that if there was a ground mass, it was degraded, either due to environmental factors or detritivores, while the part of the scat with the dark mass was either hardened due to desiccation or the bone fragments protected it so that it was preserved. The brighter sediment in the synchrotron data of the dark mass may have a higher P content and thus be the expected ground mass. The differences in the sediment inside the cavities of the dark mass compared to the surrounding matrix and the slightly higher P signals within those cavities could indicate that there is some ground mass stuck inside these cavities, though this still needs to be better explored (Fig. 21) However, it may be expected that the P content of the surrounding matrix would be higher than what we see, even if this were the case.

If the fragments were regurgitated, either as a mass of undigestible material or a gastric pellet, this would account for the lack of a ground mass surrounding the nearby fragments and a low P content in the sediment, as regurgitates are generally made up of undigestible material, like hair, bones, claws, or hooves (Fig. 27C). As stated before, there is no observed phosphatic ground mass around the associated bone fragments in the surrounding sediment in these specimens. Regurgitates have a lower phosphate-to-calcium ratio in the surrounding matrix than that observed in coprolites (Gordon et al., 2020; Allen et al., 2025). The presence of calcium levels in the surrounding sediments may indicate that bacteria broke down the material from the

digested tissue and other non-ossified parts after the regurgitated material was ejected, helping to preserve the fragments and the fragments of the dark mass. The problem with this interpretation is that none of the bone fragments found in the specimens are preserved like those observed in other regurgitalites (Zheng et al., 2018; Gordon et al., 2020; Freimuth et al., 2021). In contrast, other gastric pellets and ejecta usually have identifiable bones, as seen in the regurgitalite from Egg Mountain (Fig. 27C, D). This could be due to a change in the animal's diet, but it may not directly account for the smooth exterior of the bone fragments in the dark mass. It is also unusual that the dark mass is so tightly held together while other fragments are disarticulated. If these specimens were a gastric pellet or ejected material that had degraded and broken apart, the dark masses might be expected to be disarticulated as well. One possible explanation is that the dark mass fragments were close together and close to the surface, and thus dried and hardened together, while detritivores and moisture broke down the less-exposed portions of the specimens. Another possible complication is that the form of the specimens does not resemble other regurgitalites and is more similar to that seen in other coprolites (Fig. 27). Nevertheless, this is not strong enough evidence in of itself to discount a regurgitalite interpretation, as shape can be affected by many factors, including diagenetic or taphonomic processes which may degrade portions of the specimen to create features similar to those seen in coprolites. One last complication may be polishing from digestion. The degree observed in the samples appears higher than expected in regurgitalites (Gordon et al., 2020).

Trace Maker and implications

Depending on how these bromalites were formed, we can identify potential producers and gain greater insight into the possible preservation of the Willow Creek Anticline during the

Campanian. If the specimens are coprolites, one may be able to determine the size of the producer by the coprolite's possible size. Using a formula (animal length = 117.32 + 76.86(log (scat diameter) ± 32.93 standard error) from a study that used crocodile scat size to predict the animal's size (Platt et al., 2020), if the maximum diameter of the dark mass is the extent of the bromalite, then the producer is estimated to be around 2 m in length. It should be noted, however, that this is a rough estimate, as it is not clear if the dark mass is the furthest extent of the bromalite. If this size is correct, these specimens may be from a dromaeosaur, as some dromaeosaurs, such as *Microraptor zhaoianus*, have been known to have bones pass through their digestive systems (O'Connor et al., 2019). However, it is not currently known if this trait is one that dromaeosaurids as a whole exhibit, as closely related dinosaurs, such as members of the group Paraves (Zheng et al., 2018), have potentially produced gastric pellets (Myhrvold, 2011; Gordon et al., 2020). However, it may be that gastric pellets were a distinction between dromaeosaurs and Paraves as an adaptation for flight, thus excluding them from producing gastric pellets (Zheng et al., 2018). Another possible producer of the specimens, if they are coprolites, may be oviraptorosaurs, as *Continuoolithus* clutches (Hedge et al., 2025) have been found at Egg Mountain, and the mandibular ramus of an oviraptorosaur has been described from the Two Medicine formation (Varricchio, 2001). As stated before, the specimens are far from complete, and a predictable size may not be possible beyond the general size predicted by the existing specimens' dimensions. Excitingly, though, if these specimens are coprolites, they would be the first terrestrial vertebrate, carnivorous coprolites found in the Two Medicine Formation. This could indicate that more similar coprolites can be found here as they are preserved within the sediment.

If the specimens are regurgitalites, then candidates with a gizzard or a similar organ that allows them to separate nondigestible material from digestible material would likely be the producers. This could include *Troodon formosus*, which has been identified as a possible producer of a regurgitalite from Egg Mountain (Friemuth et al, 2021). Another possibility is the large-sized lizards such as *Palaeosaniwa* (Balsai, 2001). While the closest modern relative of *Palaeosaniwa*, the gila monster (*Heloderma suspectu*m), lacks a gizzard and does not produce gastric pellets (Christel, 2007; Wyneken, 2011), another closely related group, the varanids, does have a gizzard (AlMyhrvold, 2011), and some have been known to create gastric pellets (Auffenberg, 1982,1988; Plummer & McKenzie, 2008). The gastric pellets produced by modern varanids are looser than those observed in owls, but do have some cohesion in their gastric pellets (Kusmer, 1990; Plummer & McKenzie, 2008). However, it is also possible that both animals, such as *Troodon* and *Palaeosaniwa,* a large relative to gilo monsters (Heloderma suspectum) that grew up to 1 to 2 m (Balsai, 2021), could have produced bromalites containing these fragments. A regurgitalite interpretation would also be informative, as it would be one of two found at Egg Mountain. This could give us a better understanding of how the digestive systems of *Troodon* or other Campanian predators worked.

CONCLUSION

These specimens provide a clearer picture of the environment and ecology of Egg Mountain 75.6 million years ago. These specimens support the previous thoughts that these are biologically active sediments. This activity indicates that these specimens were likely buried during flooding after they had been dried out due to being subaerial (Thulborn, 1991; Hollocher & Hollocher, 2012). The taphonomy of the specimen suggests that it was exposed for some time and then buried, allowing detritivores to access the softer underside to feed from it, but not to consume or destroy those exposed areas.

The animal's predatory diet explains how and why the bromalite was preserved, providing insight into the region's ecology. The bone fragments may indicate that one of the individuals consumed was possibly an archosaur from the Campanian period, likely a small dinosaur native to the region. If the ingested bone fragments were from growing individuals, they may be from a juvenile. As stated, nests within the region, such as those of *Troodon*, *Maiasaura*, or other nesting dinosaurs, would be prime targets for poaching by passing predators. Due to the fragments indicating that the individual was probably older than a nestling, it is also possible that the individual is potentially a newly “fledged” individual.

It is difficult to determine which type of bromalite these samples are. The compaction of the fragments on the upper part of the specimens, along with the lack of complete skeletal elements, could indicate that the specimens are coprolites. On the other hand, the lack of an apparent ground mass around associated fragments could point towards a possible regurgitalite interpretation. As with most bromalites, determining the producer is challenging. Further analysis of the bone fragments within the specimens may provide insight into what prey the predator was

and offer some clues about the predator. However, the producer's identity may be complicated without further specimens of similar composition from the area. The size of the bromalites and the fragments found within indicates that the producer was larger than most of the smaller-sized lizards and mammals found at Egg Mountain. While a larger individual, such as an adult tyrannosaurid, may be possible, more specimens are likely to have been preserved. A small to moderately sized predator of the region, such as *Palaeosaniwa* (Balsai, 2001), a dromaeosaurid (Sues, 1978; Jasinski et al., 2020), an oviraptorosaur (Varricchio, 2001; Hedge et al., 2025), or possibly *Troodon*, is more likely a possible producer. Regardless of their origin, these specimens help understand the region's paleoecology and put other specimens found at the site into context. If found, further specimens of similar origin within the Willow Creek Anticline may help test these hypotheses.

REFERENCES CITED

Adams, J. & Organ, C. (2005). Histologic determination of ontogenetic patterns and processes in Hadrosaurian ossified tendons. Journal of Vertebrate Paleontology, 25, p. 614–622.

Allen, R. C., Chin, K., Zawaski, M., Bevitt, J. J., & Smiglewski, W. (2025). Determining whether a phosphatic concretion containing a Cretaceous juvenile crocodylian is a coprolite or a non-fecal concretion. Scientific Reports, 15, p. 6436.

Auffenberg, W. (1981). The Behavioral Ecology of the Komodo Monitor.

Auffenberg, W. (1988). Gray's monitor lizard.

Bailleul, A. M., Nyssen-Behets, C., Lengelé, B., Hall, B. K., & Horner, J. R. (2016). Chondroid bone in dinosaur embryos and nestlings (Ornithischia: *Hadrosauridae*): Insights into the growth of the skull and the evolution of skeletal tissues. Comptes Rendus Palévol, 15(1-2), p. 49–64.

Bailleul, A. M., Hall, B. K., & Horner, J. R. (2012). First Evidence of Dinosaurian Secondary Cartilage in the Post-Hatching Skull of *Hypacrosaurus stebingeri* (Dinosauria, Ornithischia). PLOS ONE, *7*(4), e36112.

Balgooyen, T. G. (1971). Pellet Regurgitation by Captive Sparrow Hawks (Falco sparverius). The Condor, 73(3), p. 382–385.

Balsai, M.J. (2001). The Phylogenetic Position of *Palaeosaniwa* and the Early Evolution of the Platynotan (Varanoid) Anguimorphs. Ph.D. Thesis, University of Pennsylvania, Philadelphia, PA, USA; p. 1–359.

Barsbold R. (1974). Saurornithoididae, a new family of small theropod dinosaurs from central Asia and North America. Palaeontologia Polonica, 30, p.5–22.

Barrett, P.M. (2005). The diet of ostrich dinosaurs (Theropoda: Ornithomimosauria). Palaeontology, 48, p. 347–358.

Beauchamp, J.S., K.M. Hart, M.S. Cherkiss, & F.J. Mazzotti. (2018). Variation in home range size and patterns in adult female American Crocodiles *Crocodylus acutus*. Endangered Species Research, 36, p. 161–171.

Brachaniec, T., Niedźwiedzki, R., Surmik, D., Krzykawski, T., Szopa, K., Gorzelak, P., & Salamon, M. A. (2015). Coprolites of marine vertebrate predators from the Lower Triassic of southern Poland. Palaeogeography, Palaeoclimatology, Palaeoecology, *435*, p. 118-126.

Carpenter, K. (1987). Paleoecological significance of droughts during the Late Cretaceous of the Western Interior. Fourth Symposium on Mesozoic Terrestrial Ecosystems, 3, p. 42–47.

Chin, K. (1996). The Paleobiological Implications of Herbivorous Dinosaur Coprolites: Ichnologic, Petrographic, and Organic Geochemical Investigations (Order No. 9724575). Available from ProQuest One Academic. (304287757).

Chin, K., Tokaryk, T. T., Erickson, G. M., & Calk, L. C. (1998). A king-sized theropod coprolite. Nature, 393(6686), p. 680–682.

Chin, K. (2002). Analyses of Coprolites Produced by Carnivorous Vertebrates. The Paleontological Society Papers, 8, p. 43–50.

Chin, K., Eberth, D. A., Schweitzer, M. H., Rando, T. A., Sloboda, W. J., & Horner, J. R. (2003). Remarkable Preservation of Undigested Muscle Tissue within a Late Cretaceous Tyrannosaurid Coprolite from Alberta, Canada. PALAIOS, 18(3), p. 286–294.

Christel, C. M., DeNardo, D. F., & Secor, S. M. (2007). Metabolic and digestive response to food ingestion in a binge-feeding lizard, the Gila monster (*Heloderma suspectum*). The Journal of Experimental Biology, 210(Pt 19), p. 3430–3439.

Comet Technologies Canada Inc. (2025). Dragonfly 3D World (Version 2025.1) [Computer software]. https://dragonfly.comet.tech/

Cooper, S. L., Marson, K. J., Smith, R. E., & Martill, D. (2022). Contrasting preservation in pycnodont fishes reveals first record of regurgitalites from the Upper Cretaceous (Maastrichtian) Moroccan phosphate deposits. Cretaceous Research, 131, p. 105111.

DeMar, J.R., D.G., Conrad, J.L., Head, J.J., Varricchio, D.J., & Wilson, G.P. (2017). New Late Cretaceous iguanomorph from North America and the origin of New World Pleurodonta (Squamata, Iguania): Proceedings of the Royal Society B: Biological Sciences, 284, p. 20161902.

Divers, S., & Stahl, S. (2015). Reptile Radiology. InBuilding Exotics Excellence: One City, One Conference, p 167

Dodson, P. (1973). The significance of small bones in paleoecological interpretation. University of Wyoming Contributions in Geology, 12, p. 15–19.

Duke, G. E. (1997). Gastrointestinal physiology and nutrition in wild birds. Proceedings of the Nutrition Society, 56(3), p. 1049–1056.

Durham, F. E. (1951). Observations on a Captive Gila Monster. The American Midland Naturalist, *45*(2), p. 460–470.

Fernández-Jalvo, Y., Andrews, P., Sevilla, P., & Requejo, V. (2014). Digestion versus abrasion features in rodent bones. Lethaia, 47(3), p. 323–336.

Fernández-Jalvo, Y., & Andrews, P. (2016). Atlas of Taphonomic Identifications: 1001+ Images of Fossil and Recent Mammal Bone Modification.

Flessa, K., Struthers, A., Fall, L.M., & Dexter, T.A. (2012). Really crappy talk: fecal volume and body size in birds, mammals, and dinosaurs. GSA Annual Meeting & Exposition, p. 4–7.

Fowler, D.W. (2017). Revised Geochronology, Correlation, and Dinosaur Stratigraphic Ranges of the Santonian–Maastrichtian (Late Cretaceous) Formations of the Western Interior of North America: PloS one, 12.

Freimuth, W. J., & Varricchio, D. J. (2019). Insect trace fossils elucidate depositional environments and sedimentation at a dinosaur nesting site from the Cretaceous (Campanian) Two Medicine Formation of Montana. Palaeogeography, Palaeoclimatology, Palaeoecology, 534, 109262.

Freimuth, W. J., Varricchio, D. J., & Chin, K. (2021). Paleoenvironmental Implications of Invertebrate Fecal Pellets (*EDAPHICHNIUM* ISP.) at an Ichnofossil-Rich Dinosaur Nesting Locality, Upper Cretaceous Two Medicine Formation, Montana, USA. PALAIOS, 36 (9), p. 283–300.

Freimuth, W. J., Varricchio, D. J., Brannick, A. L., Weaver, L. N., & Wilson Mantilla, G. P. (2021). Mammal-bearing gastric pellets potentially attributable to *Troodon formosus* at the Cretaceous Egg Mountain locality, Two Medicine Formation, Montana, USA. Palaeontology, 64(5), p. 699–725.

Gatta, M. & Rolfo, M. (2017). Cava Muracci: a new middle-upper Palaeolithic site in west-central Italy. Mediterranean Archaeology and Archaeometry, 17, p. 105–116.

Genise, J. F. (2000). The ichnofamily *Celliformidae* for *Celliforma* and allied ichnogenera: Ichnos, v. 7, p. 267–282.

Genise, J.F. (2016). Ichnoentomology: Insect Traces in Soils and Paleosols: Springer, Switzerland, p. 565.

Gordon, C., Roach, B., Parker, W., & Briggs, D. (2020). Distinguishing regurgitalites and coprolites: A case study using a Triassic bromalite with soft tissue of the pseudosuchian archosaur Revueltosaurus. Palaios. 35. p. 111–121.

Goret-Nicaise, M. (1984). Identification of collagen type I and type II in chondroid tissue. Calcif Tissue Int, **36**, p. 682–689.

Hamilton, S., Paparella, I., Bell, P., Campione, N., Fanti, F., Larson, D., Sissons, R., Vavrek, M., Balsai, M., & Sullivan, C. (2023). New Lizard Specimens from the Campanian Wapiti Formation of Alberta, Canada. Geosciences. 13. 337. 10.3390/geosciences13110337.

Hedge, J., Tucker, R. T., Makovicky, P. J., & Zanno, L. E. (2025). Fossil eggshell diversity of the Mussentuchit Member, Cedar Mountain Formation, Utah. PLOS ONE, *20*(2), e0314689.

Hirsch, K.F., & Quinn, B. (1990). Eggs and eggshell fragments from the Upper Cretaceous Two Medicine Formation of Montana: Journal of Vertebrate Paleontology, 10, p. 491–511.

Hockett, B. S. (1996). Corroded, thinned and polished bones created by golden eagles (*Aquila chrysaetos*): Taphonomic implications for archaeological interpretations. Journal of Archaeological. Science, 23, p. 587–591.

Holgado, B., Dalla Vecchia, F. M., Fortuny, J., Bernardini, F., & Tuniz, C. (2015). A Reappraisal of the Purported Gastric Pellet with Pterosaurian Bones from the Upper Triassic of Italy. PLOS ONE, 10(11), e0141275.

Holliday, C. M., Ridgely, R. C., Sedlmayr, J. C., & Witmer, L. M. (2010). Cartilaginous Epiphyses in Extant Archosaurs and Their Implications for Reconstructing Limb Function in Dinosaurs. PLOS ONE, 5(9), e13120.

Hollocher, K., & Hollocher, T.C. (2012). Early process in the fossilization of terrestrial feces to coprolites, and microstructure preservation: New Mexico Museum of Natural History and Science. 57.

Hone, D., Henderson, D.M., Therrien, F., & Habib, M.B. (2015). A specimen of *Rhamphorhynchus* with soft tissue preservation, stomach contents and a putative coprolite. PeerJ 3:e119179–92.

Horner, J. R., & Makela, R. (1979). Nest of juveniles provides evidence of family structure among dinosaurs. Nature, 282(5736), p. 296–298.

Horner, J.R. (1984). The nesting behavior of dinosaurs: Scientific American, 250, p.130–137.

Horner, J.R. (1987). Ecologic and Behavioral Implications Derived from a Dinosaur Nesting Site: Dinosaurs Past and Present, 2, p. 50–63

Horner, J.R., & Weishampel, D. (1988). A comparative embryological study of two ornithischian dinosaurs. Nature 332, p. 256–257.

Horner, J. R., De Ricqlès, A., & Padian, K. (2000). Long bone histology of the hadrosaurid dinosaur *Maiasaura peeblesorum*: growth dynamics and physiology based on an ontogenetic series of skeletal elements. Journal of Vertebrate Paleontology, 20(1), p. 115–129.

Horner, J. R., Woodward, H. N., & Bailleul, A. M. (2016). Mineralized tissues in dinosaurs interpreted as having formed through metaplasia: A preliminary evaluation. Comptes Rendus Palévol, *15*(1-2), p. 176–196.

Huerta, J. O., Henke, S. E., Wester, D. B., Eversole, C. B., Webb, S. L., & Hernandez, F. (2023). Feasibility and application of using Texas horned lizard scat to predict lizard size and age class. Wildlife Society Bulletin, 47(3), e1446.

Hunt, A. P. (1992). Late Pennsylvanian coprolites from the Kinney Brick Quarry, central New Mexico, with notes on the. *New Mexico Bureau of Mines & Mineral Resources Bulletin*, *138*, p. 221.

Hunt, A. & Lucas, S. (2012). Classification of vertebrate coprolites and related trace fossils. New Mexico Museum of Natural History and Science. Bulletin 57, p. 137–146.

Hunt, A., Lucas, S., Milàn, J., & Spielmann, J. (2012). Vertebrate coprolite studies: status and prospectus. New Mexico Museum of Natural History and Science. 57, p. 5–24.

Hunt, A. P., & Lucas, S. G. (2025). Regurgitalites. Vertebrate Ichnology, p. 381–404.

Jackson, F. D., Schaff, R. J., Varricchio, D. J., & Scmitt, J. G. (2015). A theropod nesting trace with eggs from the upper Cretaceous (Campanian) Two Medicine Formation of Montana. Palaios 38(5), p. 362–372.

Jasinski, S. E., Sullivan, R. M., & Dodson, P. (2020). New Dromaeosaurid Dinosaur (Theropoda, *Dromaeosauridae*) from New Mexico and Biodiversity of Dromaeosaurids at the end of the Cretaceous. Scientific Reports, 10(1), p. 1–10.

Korth, W. (1979). Taphonomy of microvertebrate fossil assemblages. Annals of the Carnegie Museum, 48, p. 235–285.

Klug, C., & Vallon, L. H. (2019). Regurgitated ammonoid remains from the latest Devonian of Morocco. Swiss Journal of Palaeontology, *138*(1), p. 87–97.

Kusmer, K. D. (1990). Taphonomy of owl pellet deposition. Journal of Paleontology, *64*(4), p. 629–637.

Longrich, N. R., Horner, J. R., Erickson, G. M., & Currie, P. J. (2010). Cannibalism in *Tyrannosaurus rex*. PLoS ONE, 5(10), e13419.

Lengelé, B., Schowing, J., & Dhem, A. (1996). Embryonic origin and fate of chondroid tissue and secondary cartilages in the avian skull. The Anatomical Record, 246(3), p. 377–393.

Lorenz, J.C., Gavin, W. (1984). Geology of the Two Medicine Formation and the sedimentology of a dinosaur nesting ground, in J.D. McBane and P.B. Garrison (eds.), Montana Geological Society 1984 Field Conference Guidebook: Montana Geological Society, Helena, p. 175–186.

Martin, A.J., Varricchio, D.J. (2011). Paleoecological utility of insect trace fossils in dinosaur nesting sites of the Two Medicine Formation (Campanian), Choteau, Montana: Historical Biology, v. 23, p. 15–25.

Mancuso, A. C., Benavente, C. A., Previtera, E., Arcucci, A. B., & Irmis, R. B. (2018). Carnivore coprolites from the lower Carnian (Upper Triassic) Chañares Formation, northwestern Argentina. Palaeogeography, Palaeoclimatology, Palaeoecology, *489*, 15–28.

Mitchell, J., Sander, P. M., & Stein, K. (2017). Can secondary osteons be used as ontogenetic indicators in sauropods? Extending the histological ontogenetic stages into senescence. *Paleobiology*, *43*(2), p. 321–342.

Milàn, J. (2012). Crocodylian scatology–a look into morphology, internal architecture, inter-and intraspecific variation and prey remains in extant crocodylian feces. New Mexico Museum of Natural History and Science Bulletin, 57, pp.65–71

Montes, L., de Margerie, E., Castanet, J., de Ricqlès, A., & Cubo, J. (2005). Relationship between bone growth rate and the thickness of calcified cartilage in the long bones of the *Galloanserae* (Aves). Journal of Anatomy, 206(5), 445–452.

Mayr, G., & Schaal, S.F.K.(2016). Gastric pellets with bird remains from the early Eocene of Messel. Palaios, 31, 447–451.

Myhrvold, N. (2011). A call to search for fossilised gastric pellets. Historical Biology. 24. 505–517.

Nadon, G. C. (1993). The Association of Anastomosed Fluvial Deposits and Dinosaur Tracks, Eggs, and Nests: Implications for the Interpretation of Floodplain Environments and a Possible Survival Strategy for Ornithopods. Palaios, *8*(1), p. 31-44.

Northwood, C. (2005). Early Triassic Coprolites from Australia and their Palaeobiological Significance. Palaeontology, 48, 49–68.

O'Connor, J., Zheng, X., Dong, L., Wang, X., Wang, Y., Zhang, X., & Zhou, Z. (2019). Microraptor with Ingested Lizard Suggests Non-Specialized Digestive Function. Current Biology, 29(14), p. 2423-2429.e2.

Organ, C. L., & Adams, J. (2005). The Histology of Ossified Tendon in Dinosaurs. Journal of Vertebrate Paleontology, 25(3), p. 602–613.

Padian, K., Werning, S., & Horner, J. R. (2016). A hypothesis of differential secondary bone formation in dinosaurs. Comptes Rendus Palévol, 15(1-2), p. 40–48.

Panasci, G., & Varricchio, D.J. (2020). A new terrestrial trace *Feoichnus martini*, ichnosp. Nov., from the Upper Cretaceous Two Medicine Formation (USA). Journal of Paleontology, 95, p. 922–930.

Platt, S.G., Elsey, R.M., Bishop, N.D., Rainwater, T.R., Thongsavath, O., Labarre, D., & McWilliam, A.G. (2020). Using scat to estimate body size in crocodilians: Case studies of the Siamese crocodile and American alligator with practical applications. Conserv. Biol, 15(2), p. 325–334.

Plummer, M. & McKenzie, D. (2008). Geographic distribution: Notopthalmus viridescens. Herpetological Review. 39. 104.

Qvarnström, M., Niedźwiedzki, G., Tafforeau, P., Žigaitė, Ž., & Ahlberg, P. E. (2017). Synchrotron phase-contrast microtomography of coprolites generates novel palaeobiological data. Scientific Reports, 7(1), 1-6.

Qvarnström, M., Elgh, E., Owocki, K., Ahlberg, P.E., & Niedźwiedzki, G. (2019). Filter feeding in Late Jurassic pterosaurs supported by coprolite contents. PeerJ 7:e7375

Qvarnström, M., Ahlberg, P. E., & Niedźwiedzki, G. (2019). Tyrannosaurid-like osteophagy by a Triassic archosaur. *Scientific Reports*, *9*(1), 1-9. https://doi.org/10.1038/s41598-018-37540-4

Qvarnström, M., Vikberg Wernström, J., Wawrzyniak, Z., Barbacka, M., Pacyna, G., Górecki, A., Ziaja, J., Jarzynka, A., Owocki, K., Sulej, T., Marynowski, L., Pieńkowski, G., Ahlberg, P. E., & Niedźwiedzki, G. (2024). Digestive contents and food webs record the advent of dinosaur supremacy. Nature, *636*(8042), 397–403.

Ramezani, J., Beveridge, T. L., Rogers, R. R., Eberth, D. A., & Roberts, E. M. (2022). Calibrating the zenith of dinosaur diversity in the Campanian of the Western Interior Basin by CA-ID-TIMS U–Pb geochronology. Scientific Reports, 12(1), 1–20.

Reilly, J. (2002). Growth in the Sumatran elephant (*Elephas maximus sumatranus*) and age estimation based on dung diameter. Journal of Zoology. 258. 205–213.

Roberts, E.M., & Hendrix, M.S. (2000). Taphonomy of a petrified forest in the Two Medicine Formation (Campanian), northwest Montana: implications for palinspastic restoration of the Boulder Batholith and Elkhorn Mountains volcanics. PALAIOS, v. 15, p. 476–482.

Rogers, R.R., Swisher, C.C., & Horner, J.R. (1993). Ar40/Ar39 age and correlation of the nonmarine Two Medicine Formation (Upper Cretaceous), northwestern Montana, USA: Canadian Journal of Earth Science, v. 30, p. 1066–1075.

Rogers, R. R., Currie, P. J., & Padian, K. (1997). Two Medicine formation. Encyclopedia of dinosaurs, 760–765.

Rogers, R.R., Eberth, D.A., & Ramezani, J. (2023). The “Judith River–Belly River problem” revisited (Montana-Alberta-Saskatchewan): New perspectives on the correlation of Campanian dinosaur bearing strata based on a revised stratigraphic model updated with CA-ID-TIMS U-Pb geochronology: Geological Society of America Bulletin, v. 136, p. 1221–1237

Rogers, R.R., Horner, J.R., Ramezani, J., Roberts, E.M., & Varricchio, D.J. (2025). Updating the Upper Cretaceous (Campanian) Two Medicine Formation of Montana: Lithostratigraphic revisions, new CA-ID-TIMS U-Pb ages, and a calibrated framework for dinosaur occurrences. Geological Society of America Bulletin.

Romer, A. S., & Parsons, T. S. (1970). The vertebrate body.

Sanz, J., Chiappe, L., Fernández Jalvo, Y., Ortega, F., Sánchez, B., Poyato-Ariza, F. J., Pérez-Moreno, B. (2001). An Early Cretaceous pellet. Nature. 409, p. 998–1000.

Sanz, M., Daura, J., Égüez, N., & Brugal, J. (2016). Not only hyenids: A multi-scale analysis of Upper Pleistocene carnivore coprolites in Cova del Coll Verdaguer (NE Iberian Peninsula). Palaeogeography, Palaeoclimatology, Palaeoecology, 443, p. 249–262.

Scofield, G. (2018). Analysis of hadrosaur teeth from Egg Mountain Quarry, a diffuse microsite locality, upper Cretaceous, Two Medicine Formation, northwest Montana. Montana State University - Bozeman, College of Letters & Science.

Shelton, J. A. (2007). Application of sequence stratigraphy to the nonmarine Upper Cretaceous Two Medicine Formation, Willow Creek anticline, northwestern, Montana. Montana State University - Bozeman, College of Letters & Science.

Shillito, L. M., Blong, J., Green, E., & van Asperen, E. (2020). The what, how and why of human coprolite analysis in archaeology. 10.31223/osf.io/uf3qe.

Sues, H.D. (1978). A new small theropod dinosaur from the Judith River Formation (Campanian) of Alberta Canada. Zoological Journal of the Linnean Society, *62*(4), p. 381–400.

Vanden Berge, J. C., & Storer, R. W. (1995). Intratendinous ossification in birds: A review. Journal of morphology, 226(1), p. 47–77.

Varricchio, D., Jackson, F., Borkowski, J., & Horner, J. (1997). Nest and egg clutches of the dinosaur *Troodon formosus* and the evolution of avian reproductive traits. Nature 385, p. 247–250.

Varricchio, D. J., Jackson, F., & Trueman, C. N. (1998). A Nesting Trace with Eggs for the Cretaceous Theropod Dinosaur Troodon formosus, Journal of Vertebrate Paleontology, 19:1, p. 91-100

Varricchio, D. J. (2001). Late Cretaceous Oviraptorosaur (Theropoda) Dinosaurs of Montana, Mesozoic Vertebrate Life. Indiana University Press. p. 42–57. In D. Tanke and K. Carpenter (eds).

Wang, S., Ding, N., Ma, W., Yu, W., Zheng, T., Choiniere, J., & Xu, X. (2025). Direct evidence of carnivory in the early-diverging *Alvarezsaurian Bannykus*. The Innovation Geoscience **3**:100143.

Wang, X., White, S. C., Balisi, M., Biewer, J., Sankey, J., Garber, D., & Tseng, Z. J. (2018). First bone-cracking dog coprolites provide new insight into bone consumption in *Borophagus* and their unique ecological niche. ELife, *7*, e34773.

Weaver, J. L., & Fritts, S. H. (1979). Comparison of Coyote and Wolf Scat Diameters. The Journal of Wildlife Management, *43*(3), 786–788.

Weaver, L. N., Varricchio, D. J., Sargis, E. J., Chen, M., Freimuth, W. J., & Wilson Mantilla, G. P. (2021). Early mammalian social behaviour revealed by multituberculates from a dinosaur nesting site. Nature Ecology & Evolution, *5*(1), p. 32–37.

Webb W. A. (1988). Management of foreign bodies of the upper gastrointestinal tract. Gastroenterology, 94(1), p. 204–216

Wehrle, B. A., & German, D. P. (2023). Reptilian digestive efficiency: Past, present, and future. Comparative Biochemistry and Physiology Part A: Molecular & Integrative Physiology, 277, 111369.

Wood, J. R., & Wilmshurst, J. M. (2014). Late Quaternary terrestrial vertebrate coprolites from New Zealand. Quaternary Science Reviews, 98, p. 33-44.

Woodward Ballard, H. (2012). Comparative population histovariability within the archosauria. (Order No. 3516469, Montana State University). ProQuest Dissertations and Theses, 273.

Woodward Ballard, H., Horner, J., & Farlow, J. (2014). Quantification of intraskeletal histovariability in Alligator mississippiensis and implications for vertebrate osteohistology. PeerJ. 2. e422. 10.7717/peerj. 422.

Wyneken, J. (2011). Anatomy and physiology of the reptilian gastrointestinal tract. Eighteenth Annual Conference Proceedings Association of Reptilian and Amphibian Veterinarians, p. 50

Zheng, X., Wang, X., Sullivan, C., Zhang, X., Zhang, F., Wang, Y., Li, F., & Xu, X. (2018). Exceptional dinosaur fossils reveal early origin of avian-style digestion. Scientific Reports, 8, 14217.

APPENDICES

APPENDIX A

BONE FRAGMENTS

Table A1. Table of Fragments found within specimens. All fragments except # 16 are primarily internal to the specimen, with # 16 being seen on the bottom face of the specimen. Fragments that are close to the dark mass are either closely associated with or touching the fragments of the dark mass. # 22 is a fecal pellet used as a reference for other pellets found inside the specimens.

ID	Size(mm)	Potential Type	Close to Dark Mass	Specimen ID	Relative Shape	Notes
1	9.8 x 6.0 x 3.4	Cortical	No	MOR 10878-4B	Semi-Rectangular	Long bone? Ossified tendon? Associated Figs: 8,21
2	13.4 x 7.2 x 2.9	Trabecular	No	MOR 10878-4B	Concave, Rounded	Long bone epiphysis, cartilage, Associated Figs: 9,10
3	2.3 x 1.9 x 1.3	Cortical	No	MOR 10878-4B	Semi-Rounded	
4	2.7 x 1.6 x 1.7	Trabecular	Yes	MOR 10878-4B	Cylindrical	Cartilage, Associated Fig: 11,12
5	6.4 x 4.5 x 3.0	Unknown	Yes	MOR 10878-4B	Semi-Rectangular, Wavy surface	edge of dark mass?
6	6.5 x 5.3 x 2.1	Trabecular?	Yes	MOR 10878-4B	Semi-rectangular	
7	1.3 x 1.0 x 1	Cortical	No	MOR 10878-4A	Cylindrical	Vertebra?, Shaft Fragment?
8	4.6 x 3.6 x 1.5	Trabecular	Yes	MOR 10878-4A	Flat/Semi-Triangular	Near side of dark mass between glued segments
9	3.4 x 2.0 x 1.0	Trabecular	No	MOR 10878-4A	Rectangular	Very faint (Same density as Matrix), Asso. 9,10,11

10	0.8 x 0.7 x 0.6	Cortical	No	MOR 10878-4A	Semi-cylindrical	Similar density to 6, associated with 8,10,11
11	1.2 x 0.6 x 0.9	Cortical	No	MOR 10878-4A	Amorphous	Similar density to 8, associated with 8,9,11
12	0.8 x 0.6 x 0.4	Cortical	No	MOR 10878-4A	Amorphous	Similar density to 8, associated with 8,9,10
13	1.4 x 1.0 x 0.6	Cortical	No	MOR 10878-4A	Amorphous	
14	2.3 x 1.0 x 0.5	Trabecular	No	MOR 10878-4A	Flat/Semi-Rect.	Edge of bone? Associated with 14 and 15
15	0.8 x 0.6 x 0.4	Unknown	No	MOR 10878-4A	Rounded	Associated with 13 and 15
16	2.4 x 2.0 x 1.1	Trabecular	Yes	MOR 10878-4A	Flattened/ Rounded sides	Associated with 13 and 14
17	30.2 x 12.0 x 1.4	Trabecular	No	MOR 10878-9	Flat/Rectangular	Bottom of Specimen, 1.10 gap between pieces
18	8.5 x 7.9 x 5.6	Trabecular	No	MOR 10878-9	Semi-ovoid	
19	4.8 x 3.2 x 2.7	Trabecular	Yes	MOR 10878-9	Ovoid	
20	16.7 x 9.9 x 1.5	Trabecular	Yes	MOR 10878-9	Flat/Rectangular	Multiple associated fragments, Seen on the surface of the specimen

21	3.6 x 2.5 x 2.3	Trabecular	Yes	MOR 10878-9	Rounded	
22	1.6 x 1.3	Fecal pellet	No	MOR 10878-9	Ovoid	Invertebrate fecal pellet. Close to dark mass.
23	2.6 x 1.6 x 1.2	Unknown	Yes	MOR 10878-9	Semi-cylindrical	Semi-cylindrical
24	4.5 x 1.7 x 2.2	Trabecular	Yes	MOR 10878-9	Semi-cylindrical,	Associated with 20 and 21
25	3.8 x 2.5 x 3.79	Trabecular?	No	MOR 10878-9	Flat/Jagged	
26	7.9 x 3.3 x 2.3	Trabecular	No	MOR 10878-9	Jagged	

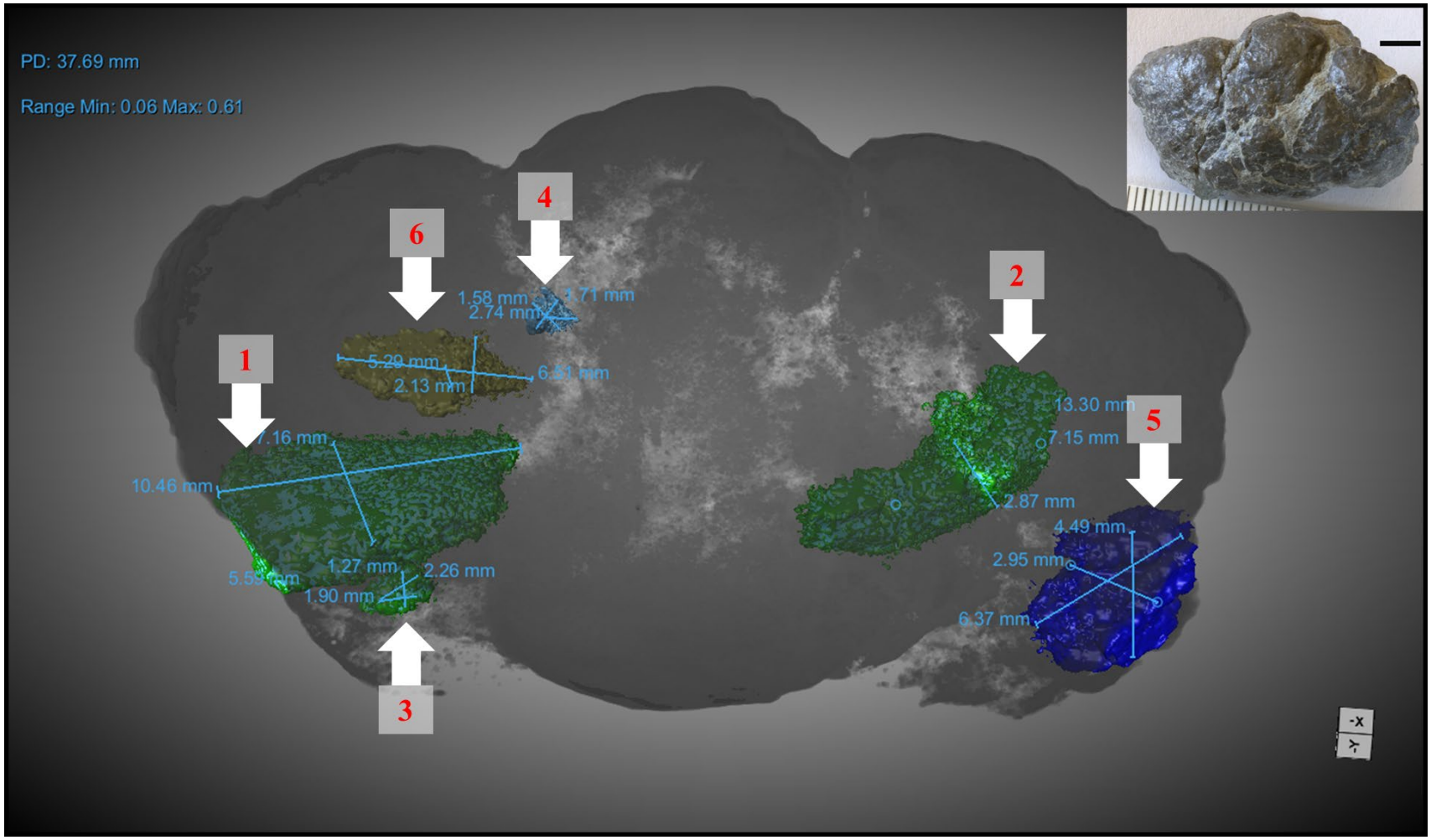

Figure A1: Image of bone fragments within MOR 10878-4B using CT scan data. Numbers are associated with the fragments in Table A1.

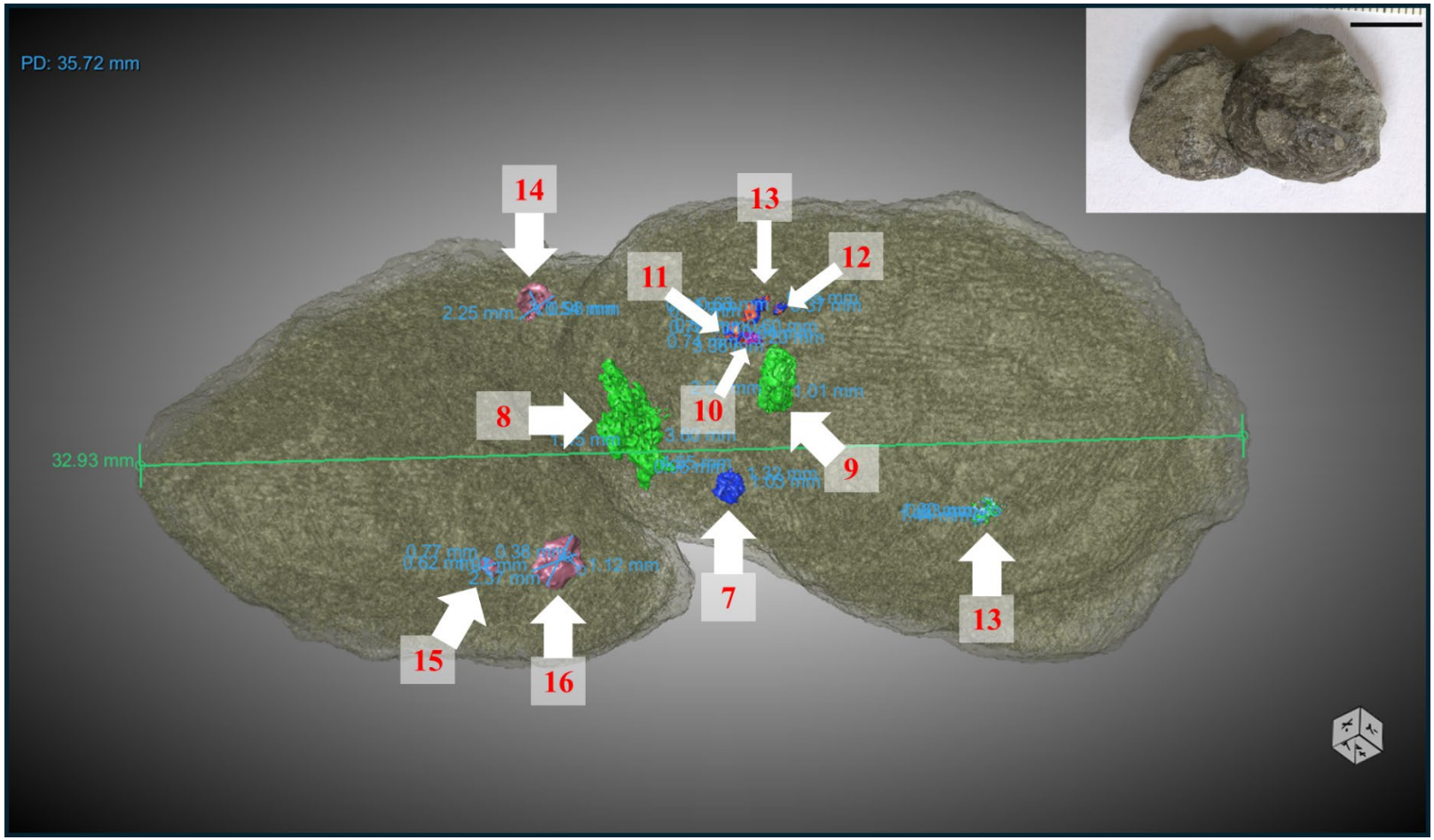

Figure A2: Image of bone fragments found within MOR-10878-4A using synchrotron data. Numbers are associated with the fragments in Table A1.

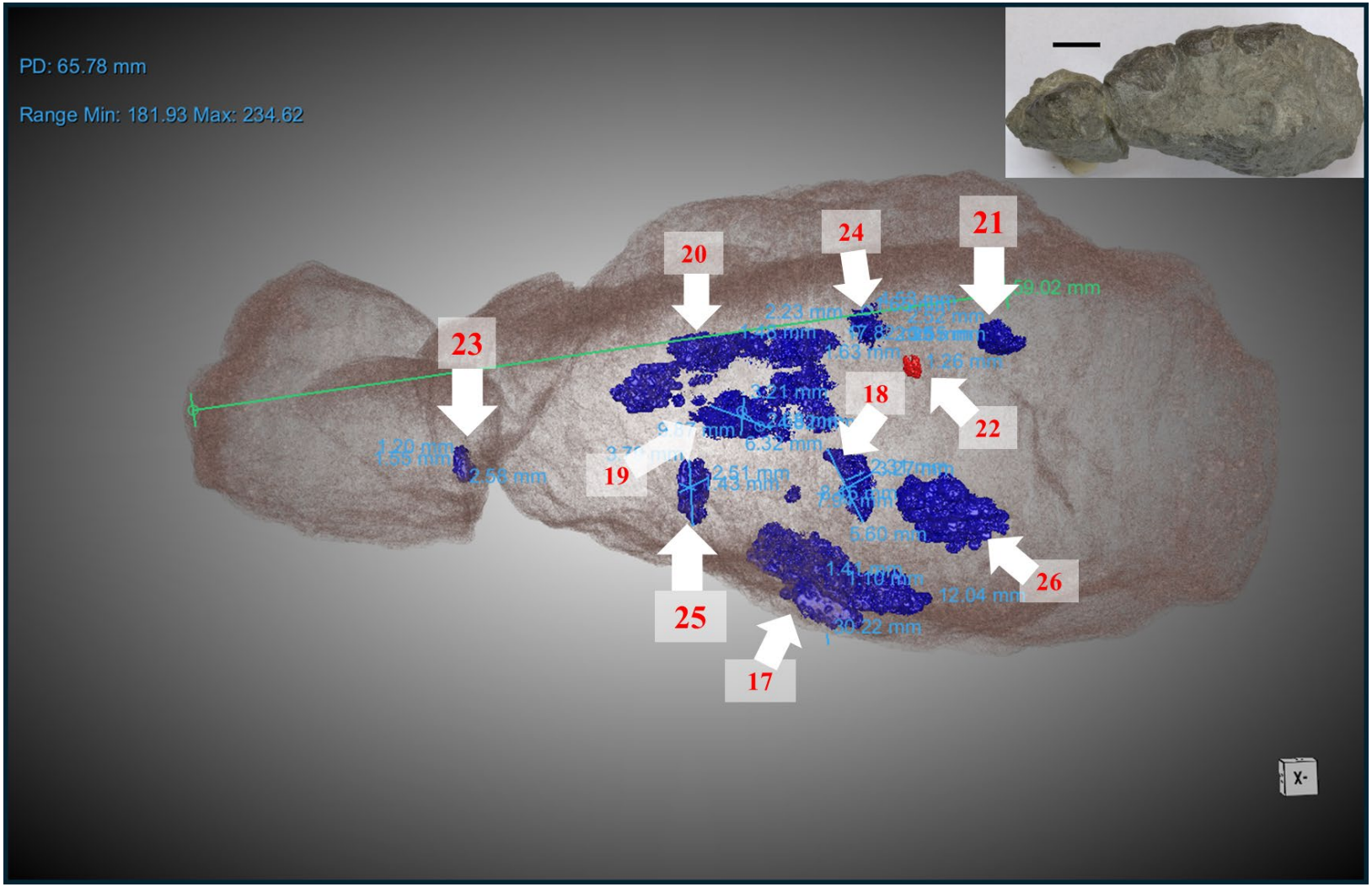

Figure A3: Image of bone fragments found within MOR-10878-4A using synchrotron data. Numbers are associated with the fragments in Table A1.